

HYDROGEN EMBRITTLEMENT SUSCEPTIBILITY
OF LINEPIPE STEEL

HYDROGEN EMBRITTLEMENT SUSCEPTIBILITY OF CA-
TREATED LINEPIPE STEEL SKELP

BY: SARA FILICE, B.ENG

A Thesis

Submitted to the Department of Materials Science & Engineering
and the School of Graduate Studies
in Partial Fulfilment of the Requirements
for the Degree
Master of Applied Science

McMaster University

© Copyright by Sara Filice, December 2017

McMaster University
Hamilton, Ontario

MASTER OF APPLIED SCIENCE (2017)
(Materials Science & Engineering)

TITLE: Hydrogen Embrittlement Susceptibility of
Ca-Treated Linepipe Steel Skelp

AUTHOR: Sara Filice, B. Eng (McMaster University)

SUPERVISOR: Dr. J.R. Kish

NUMBER OF PAGES: 110

Abstract

The aim of this research was to identify problematic microstructural features as hydrogen traps in linepipe steel that serve to increase the hydrogen embrittlement susceptibility. A comparison was made between the hydrogen trapping capacity and associated hydrogen embrittlement susceptibility of Ca-treated X60 grade steel skelp and X70 grade steel skelp: the latter typically being more susceptible to hydrogen-induced cracking in sour environments.

Through-thickness variations in the steel skelp microstructure were characterized across multi-length scales using light optical microscopy (LOM) and scanning electron microscopy (SEM) equipped with X-ray energy dispersive spectroscopy (EDS). Key features under study include the composition, shape, and distribution of non-metallic inclusions, as well as differences in features present between the quarterline ($\frac{1}{4}$ and $\frac{3}{4}$ depths) and centerline ($\frac{1}{2}$ depth) microstructures. The type, count, and average size of inclusions present in both steel skelp grades were analyzed using an automated SEM-EDS technique called ASPEX[®]. Major types of inclusions detected in both grades of steel skelp include those containing Ca, Al, Mn, Mg and Ti as major elements. Overall, the area fraction of inclusions detected in the X70 steel was larger than those detected in the X60 with the exception of Ti-containing inclusions, which had a larger area fraction within the X60 steel. Comparing the number of detected inclusions shows that there were overall slightly less Ca-containing inclusions and significantly less Ti-containing inclusions

detected in the X70 steel but there were generally more Al-containing, Mg-containing, and Mn-containing inclusions than those detected in the X60 steel.

Thermal desorption spectroscopy (TDS) measurements were made on samples prepared from the $\frac{1}{4}$, $\frac{1}{2}$, and $\frac{3}{4}$ depths of X60 and X70 steel skelps after galvanostatic cathodic charging in an As_2O_3 -containing solution using an applied current density of -10 mA/cm^2 . Hydrogen release was measured using a HYDROSTEEL[®] probe while the sample was heated from 20°C to 650°C to detect temperature values at which hydrogen gas release peaks occurred, and thus provide information on types of reversible and/or irreversible traps present. The TDS results suggests that non-metallic inclusions indeed serve as irreversible traps along with grain boundaries and dislocations, which serve as reversible traps. Hydrogen permeation measurements were also made on samples prepared from the $\frac{1}{4}$, $\frac{1}{2}$, and $\frac{3}{4}$ depths after galvanostatic cathodic charging in an As_2O_3 -containing solution using an applied current density of -10 mA/cm^2 . Hydrogen gas release was measured using a HYDROSTEEL[®] probe while the sample remained at room temperature ($\sim 20^\circ\text{C}$), providing information regarding the potency of reversible hydrogen traps when subjected to a flux of hydrogen. Only reversible traps can be detected at room temperatures due to their low binding energies. Higher temperatures are required to overcome the larger binding energies associated with irreversible traps. The hydrogen permeation results indicated no significant effect of through-thickness variations in the X60 steel, but the centreline depth of the X70 steel skelp trapped a larger quantity of hydrogen than either of the two quarterline depths, indicating the presence of a distinct problematic trap. The X70 steel skelp was also observed to trap more hydrogen than the X60 steel skelp.

The observed hydrogen trapping capacity was linked to the hydrogen embrittlement susceptibility by comparing the uniaxial tensile behaviour of centreline samples with and without hydrogen charging applied as a pre-treatment step. Hydrogen charging was achieved by galvanostatic cathodic polarization at an applied current density of -10 mA/cm^2 for 24 h in an NH_4SCN -containing solution while simultaneously loading the samples to 85% of the yield strength using a proof ring tensile test cell. An increase in hydrogen embrittlement as a result of pre-charging was confirmed through tensile plots by comparing the area of reduction and failure strain of charged samples to uncharged samples. A decrease in both values was observed in the charged samples indicating a loss in ductility as a result of hydrogen charging. Fracture surfaces were imaged using SEM and inclusions of interest were analyzed for elemental composition using EDS. Inclusions observed along the fracture surfaces include oxysulfides of Ca and Al, oxides of Mg, Al-Ca-Si oxides, and Al_2O_3 -containing inclusions which are likely to be heterogeneous Al-Ca-O inclusions.

Acknowledgements

I would like to begin by thanking my supervisor, Dr. Joey Kish, for providing me not only with an interesting project, but also for his unconditional support, guidance, and patience with me throughout the duration of my master's degree. I am appreciative that he allowed me to attend numerous conferences over the years which gave me the opportunity to present my research and connect with other corrosion researchers. His constant encouragement over these years helped me grow not only as a researcher, but also as an individual, and has helped me gain confidence in myself. This project would not have been possible without him and I am incredibly grateful for all of his efforts over the years.

Thank you to Dr. Fateh Fazeli and the scientists and technicians at CanmetMATERIALS who allowed me to use their facility for the completion of my TDS and hydrogen permeation experiments required in my master's project. I also owe plenty of thanks to Dr. Joe McDermid, who also provided unlimited amounts of guidance and support for me through the course of my master's degree. I am grateful for his willingness to share his input and ideas throughout the completion of my project. Thank you to Dr. Mike Bruhis and Dr. Beth McNally for their in-lab support and for taking the time to teach me how to use the instruments required for the completion of my project. I would also like to thank Chris Butcher for electron microscopy training, as well as Shooka Mahboubi, Caitlin Dever, and Daniella Pallisco for microscopy support and assistance.

Profuse thanks is extended to NSERC, Evraz, and Nucor for providing financial support for my project, Evraz for providing me with Ca-treated steel skelp, and to ArcelorMittal Dofasco for conducting ASPEX[®] analysis on my steel samples.

I would also like to thank my colleagues and friends in the Department of Materials Science and Engineering for providing both academic and personal support, as well as filling my days in the office and lab with happiness and endless laughter.

And finally, I would like to thank my family, who continuously expressed their belief in me, stood by me in my times of stress, and always encouraged me to do my best. I would not be the person I am today without their constant love and support.

Abbreviations and Symbols

List of Abbreviations

API	American Petroleum Institute
BOF	Basic Oxygen Furnace
CLR	Crack Length Ratio
CSR	Crack Sensitivity Ratio
CTR	Crack Thickness Ratio
EAF	Electric Arc Furnace
EBSD	Electron Backscatter Diffraction
EDSS	X-ray Energy Dispersive Spectroscopy
EIC	Environmentally Induced Cracking
HE	Hydrogen Embrittlement
HIC	Hydrogen Induced Cracking
ICP-OES	Inductively Coupled Plasma – Optical Emission Spectroscopy
LOM	Light Optical Microscope/Microscopy
ND	Normal Direction
RD	Rolling Direction
SCC	Stress Corrosion Cracking
SEM	Scanning Electron Microscope/Microscopy
SSC	Sulfide Stress Cracking
TD	Transverse Direction
TDS	Thermal Desorption Spectroscopy

List of Symbols

%RA	Percent reduction in area
°C	Degrees Celsius
A	Cross-sectional area
A	Trapping site
A _o	Initial cross-sectional area of tensile gauge
B	Normal lattice site
cm	Centimetre
e	Engineering strain
E _a	Trap activation energy
E _b	Trap binding energy
E _n	Diffusion activation energy
E _s	Sadle point energy
F	Tensile force
h	Hour
kJ	Kilojoule
kN	Kilonewton
L _o	Initial tensile gauge length
m	Metre
mA	Milliampere
min	Minute
mm	Millimetre
mol	Mole
MPa	MegaPascal
N	Newton
pL	Picolitre
s	Engineering stress

s	second
YS	Yield stress
YS _{0.2%}	0.2% offset tensile yield stress
ΔL	Change in tensile gauge length
ϵ_f	True strain at failure
μm	Micrometre

Table of Contents

Abstract	iii
Acknowledgements	vi
Abbreviations and Symbols	viii
List of Abbreviations	viii
List of Symbols	ix
Table of Contents	xi
List of Tables	xii
List of Figures	xiii
Chapter 1: Introduction	1
Chapter 2: Literature Review	5
2.1. Hydrogen-Induced Cracking.....	5
2.2. Comparison of X60 and X70 Linepipe Steel	13
2.3. Role of Ca Treatment.....	16
2.4. Fracture Mechanics	20
2.5. Opportunities for Research	24
Chapter 3: Experimental Methods	26
3.1. Materials	26
3.2. Microstructure Characterization	27
3.3. Diffusible Hydrogen Characterization.....	30
3.4. Hydrogen Embrittlement Susceptibility	36
Chapter 4: Results and Discussion.....	43
4.1. Starting Material Characterization	43
4.2. Characterization of Diffusible Hydrogen.....	69
4.3. Hydrogen Embrittlement Susceptibility	80
4.4. Outlook	97
Chapter 5: Conclusions	98
Appendix I: Calibration of CorTest [®] Proof Ring	101
Appendix II: Inclusions Detected in X60 and X70 Steel.....	103
References	106

List of Tables

Table 2.1: Published data for activation energy of hydrogen escape for various traps in steel.	8
Table 2.2: Problematic inclusions reported in literature, (a) elongated Si-enriched inclusion, (b) Al oxide inclusion with small amounts of Mg and Ca, (c) inclusion containing globular Al ₂ O ₃ with elongated MnS, (d) inclusion containing Ti oxide and Al oxide, (e) inclusion containing iron carbide and Al oxide [25], [35], [34]. ...	12
Table 2.3: Chemical requirements for API 5L linepipe steel [36].	13
Table 2.4: Tensile requirements for API 5L linepipe steel [36].	14
Table 2.5: Macroscopic and microscopic fractographic features [28].	21
Table 3.1: Chemical composition of linepipe steel skelp material.	27
Table 4.1: Count, average diameter and area fraction of inclusions as determined through ASPEX [®] analysis for the RD-ND plane and TD-ND planes of the X60 steel.	55
Table 4.2: Count, average diameter and area fraction of inclusions as determined through ASPEX [®] analysis for the RD-ND plane and TD-ND planes of the X70 steel.	56
Table 4.3: Hydrogen flux values from low temperature TDS analysis as determined by peak temperature values for the detected hydrogen trapping peak.	74
Table 4.4: Summary of mechanical properties for uncharged and charged tensile samples.	83
Table I.1: Deflection values corresponding to applied compressive axial load.	101
Table I.2: Deflection values corresponding to released compressive axial load.	102
Table II.1: SEM-EDS images of inclusions detected in the X60 grade steel skelp.	104
Table II.2: SEM-EDS images of inclusions detected in the X70 grade steel skelp.	105

List of Figures

Figure 2.1: Schematic diagram illustrating common mechanisms of hydrogen introduction into steel [16].	6
Figure 2.2: Energy levels associated with a hydrogen trap [11].	7
Figure 2.3: Schematic of HIC initiation sites based on inclusion geometry [12].	17
Figure 2.4: HIC susceptibility of steel containing various Ca/S ratios [12].	18
Figure 2.5: Relationship between Ca/S ratio and formation of inclusions [15].	20
Figure 2.6: SEM imaged comparing the basic types of overload fracture: (a) intergranular fracture, (b) transgranular fracture by cleavage, (c) ductile fracture with equiaxed dimples [28].	22
Figure 2.7: Schematic image of (a) brittle fracture with slip path at 45° to tensile axis, and (b) ductile material undergoing necking during plastic deformation [42].	23
Figure 2.8: Images of (a) ductile and (b) brittle tensile fractures [43].	23
Figure 3.1: Schematic showing orientation and labeling of planes of the steel skelp material.	28
Figure 3.2: Flat disk samples used for thermal desorption spectroscopy measurements.	31
Figure 3.3: Experimental apparatus used to charge samples with hydrogen via galvanostatic cathodic polarization for subsequent TDS measurements.	33
Figure 3.4: Experimental apparatus used for thermal desorption spectroscopy measurements (courtesy CanmetMATERIALS).	34
Figure 3.5: Rectangular plate samples used for hydrogen permeation experiments.	35
Figure 3.6: Experimental apparatus used for hydrogen permeation measurements (courtesy of CanmetMATERIALS).	36
Figure 3.7: Sub-size cylindrical tensile samples used for tensile testing of X60 and X70 steel skelp material with and without hydrogen charging.	38
Figure 3.8: Engineering stress-strain plots for as-received X60 and X70 ½ depth (centreline) samples to determine 0.2% offset yield stress ($YS_{0.2\%}$).	39

Figure 3.9: Experimental apparatus used to charge the tensile samples with hydrogen under a constant applied cathodic current density and a constant elastic loading (85% of $YS_{0.2\%}$).	40
Figure 3.10: Proof ring calibration curve.....	41
Figure 4.1: LOM images of the as-received centreline microstructures of the X60 steel (a) RD-TD, (b) TD-ND, and (c) RD-ND planes and the X70 steel (d) RD-TD, (e) TD-ND, and (f) RD-ND planes.	44
Figure 4.2: LOM images of the RD-ND plane of the X60 steel at the (a) $\frac{1}{4}$ depth, (b) $\frac{1}{2}$ depth, and (c) $\frac{3}{4}$ depth locations and of the X70 steel at the (d) $\frac{1}{4}$ depth, (e) $\frac{1}{2}$ depth, and (f) $\frac{3}{4}$ depth locations.	46
Figure 4.3: SEM images of the RD-ND plane of the X60 steel at the (a) $\frac{1}{4}$ depth, (b) $\frac{1}{2}$ depth, and (c) $\frac{3}{4}$ depths and of the X70 steel (d) $\frac{1}{4}$ depth, (e) $\frac{1}{2}$ depth, and (f) $\frac{3}{4}$ depth locations.	48
Figure 4.4: SEM images of $\frac{1}{2}$ depth from X60 steel skelp from the RD-ND plane, (a) and (b), and the TD-ND plane, (c) and (d). Polygonal ferrite (PF) and pearlite (P) phases are indicated.	50
Figure 4.5: SEM images of $\frac{1}{2}$ depth from X70 steel skelp from the RD-ND plane, (a) and (b), and the TD-ND plane, (c) and (d). Polygonal ferrite (PF) and bainite (B) phases are indicated.	51
Figure 4.6: Effect of Ca/S ratio on the HIC susceptibility of steel [12].	53
Figure 4.7: Area fraction plots of inclusions as determined through ASPEX [®] analysis for the X60 steel: (a) RD-ND plane and (b) TD-ND plane.	58
Figure 4.8: Area fraction plots of inclusions as determined through ASPEX [®] analysis for the X70 steel: (a) RD-ND plane and (b) TD-ND plane.	59
Figure 4.9: SEM image (a) and associated EDS maps (b) of a randomly selected inclusion in the $\frac{1}{2}$ depth of the X60 steel.	62
Figure 4.10: SEM image (a) and associated EDS maps (b) of a second randomly selected inclusion in the $\frac{1}{2}$ depth of the X60 steel.....	63

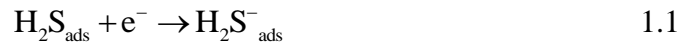
Figure 4.11: SEM image (a) and associated EDS maps (b) of a randomly selected inclusion in the $\frac{1}{4}$ depth of the X70 steel.....	63
Figure 4.12: SEM image (a) and associated EDS (b) maps of a second randomly selected inclusion in the $\frac{1}{2}$ depth of the X70 steel.....	64
Figure 4.13: SEM image (a) and associated EDS maps (b) of a third randomly selected inclusion in the $\frac{1}{2}$ depth of the X70 steel.....	64
Figure 4.14: Comparison of inclusion group area fraction in the X60 and X70 steel for the (a) RD-ND plane and (b) TD-ND plane at the $\frac{1}{4}$ depth, (c) the RD-ND plane and (d) TD-ND plane for the $\frac{1}{2}$ depth, and (e) the RD-ND plane and (f) TD-ND plane for the $\frac{3}{4}$ depth.....	67
Figure 4.15: Comparison of inclusion group total count in the X60 and X70 steel for the (a) RD-ND plane and (b) TD-ND plane at the $\frac{1}{4}$ depth, (c) the RD-ND plane and (d) TD-ND plane for the $\frac{1}{2}$ depth, and (e) the RD-ND plane and (f) TD-ND plane for the $\frac{3}{4}$ depth.....	68
Figure 4.16: Comparison of inclusion group average diameter in the X60 and X70 steel for the (a) RD-ND plane and (b) TD-ND plane at the $\frac{1}{4}$ depth, (c) the RD-ND plane and (d) TD-ND plane for the $\frac{1}{2}$ depth, and (e) the RD-ND plane and (f) TD-ND plane for the $\frac{3}{4}$ depth.	69
Figure 4.17: TDS data for (a) $\frac{1}{4}$ depth, (b) $\frac{1}{2}$ depth, and (c) $\frac{3}{4}$ depth of the X60 steel sample after prior galvanostatic cathodic charging.....	71
Figure 4.18: Plot of total diffusible hydrogen versus cathodic charging current density to determine hydrogen saturation.....	71
Figure 4.19: Low temperature TDS data for (a) X60 steel samples and (b) X70 steel samples after prior galvanostatic cathodic charging.	73
Figure 4.20: High temperature TDS data for (a) X60 steel samples and (b) X70 steel samples after galvanostatic cathodic charging, and 1st derivative plots for (c) X60 steel samples and (d) X70 steel samples.....	75

Figure 4.21: TDS data for the X60 steel and X70 steel samples from the ½ depth for (a) low temperature analysis and (b) derivative plot of high temperature analysis after galvanostatic cathodic charging.	77
Figure 4.22: Hydrogen permeation data acquired for the (a) X60 steel samples and (b) X70 steel samples after prior galvanostatic cathodic charging.	78
Figure 4.23: Engineering stress-strain plots of repeated sets for (a) X60 uncharged, (b) X70 uncharged, (c) X60 after charge, and (d) X70 after charge.	82
Figure 4.24: Low magnification SEM images of ½ depth X60 steel sample fracture surfaces: (a) non-charged (starting) sample, (b) Test 1 charged sample, and (c) Test 2 charged sample. Higher magnification SEM images of outer region of (d) non-charged (starting) sample, (e) Test 1 charged sample, and (f) Test 2 charged sample and of inner region of (g) non-charged (starting) sample, (h) Test 1 charged sample, and (i) Test 2 charged sample.	84
Figure 4.25: SEM images (a-c) of fisheye feature found on the ½ depth X60 Test 1 steel sample fracture surface at various magnifications. (d) EDS analysis of inclusion found within fisheye feature shown in (c).	85
Figure 4.26: SEM images (a-b) of inclusion of interest found on the ½ depth X60 Test 2 steel sample fracture surface at various magnifications. (c) EDS analysis of inclusion shown in (b).	86
Figure 4.27: Low magnification SEM images of ½ depth X70 steel sample fracture surfaces: (a) non-charged (starting) sample, (b) Test 1 charged sample, and (c) Test 2 charged sample. Higher magnification SEM images of outer region of (d) non-charged (starting) sample, (e) Test 1 charged sample, and (f) Test 2 charged sample and of inner region of (g) non-charged (starting) sample, (h) Test 1 charged sample, and (i) Test 2 charged sample.	88
Figure 4.28: SEM images (a) of inclusion of interest found on the ½ depth X70 Test 1 steel sample fracture surface and (b) EDS analysis of inclusion.	89

Figure 4.29: SEM images (a-b) of inclusion of interest found on the ½ depth X70 Test 2 steel sample fracture surface at various magnifications. (c) EDS analysis of inclusion shown in (b).	91
Figure 4.30: SEM image of ½ depth X70 steel sample fracture surface in cross-section: a) Test 1, and b) Test 2.....	92
Figure 4.31: (a) SEM image and (b) associated EDS maps of inclusion found on ½ depth X70 Test 1 steel sample cross-section close to fracture surface.	92
Figure 4.32: (a) SEM image (b) and associated EDS maps of inclusion found on ½ depth X70 Test 2 steel sample cross-section close to fracture surface.	93
Figure 4.33: Area fraction versus count for each inclusion type detected through ASPEX® at the ½ depth for X60 and X70 steel skelps.	95
Figure 4.34: Comparison of the centreline behaviour between X60 and X70 steel skelps during (a) TDS, and (b) hydrogen permeation.....	95

Chapter 1: Introduction

Pipelines are extensively used in the transportation of oil and gas. In order to improve the reliability and safety of this transportation method, ongoing efforts have been made to identify the cause of stress corrosion cracking (SCC) and hydrogen induced cracking (HIC) susceptibility of the steel grades typically used to fabricate the pipelines. Natural gas can be classified as sweet gas or sour gas. Sweet gas has low sulfur content whereas sour gas contains high amounts of sulfur, namely hydrogen sulfide (H₂S), which causes the absorption of atomic hydrogen into the steel as a result of hydrogen dissociation by the H₂S corrosion reaction [1], [2]. Kawashima et al. have proposed the following mechanism for hydrogen adsorption and introduction to the linepipe steel [3]:



The absorption of hydrogen into the steel accelerates embrittlement and results in SCC and HIC [3]. For the transportation of sour gas, it is necessary to develop linepipe steels that are classified as sour service grades, which have improved resistance to HIC. To be qualified a sour service grade steel, NACE International has developed standard tests, NACE TM0177 and TM0284, which evaluate the SCC and HIC susceptibility respectively in H₂S environments [4]–[6].

Microstructural features of the steel can affect the mobility of absorbed hydrogen by acting as traps [7]. Hydrogen that is weakly trapped is considered to be reversible and hydrogen that is strongly trapped is considered to be irreversible. Whether a trap is considered to be reversible or irreversible is highly dependent on the binding energy of the trap. A trap is considered irreversible at ambient temperature if the absolute binding energy of the trap is higher than 35 kJ/mol [8]. Irreversible traps may become reversible at higher temperatures and can be detected through thermal desorption spectroscopy (TDS) measurements. TDS peaks detected at low temperatures correspond with reversible traps and TDS peaks detected at high temperatures correspond to irreversible traps [9]. Features within the microstructure that can act as hydrogen traps include grain boundaries, microvoids, dislocations, non-metallic inclusions, and precipitate particles [10]. The presence of these traps in the steel microstructure has been reported as a main contributing factor to HIC [11]. More specifically, it has been reported that inclusion types harmful to HIC include aluminum oxides, aluminum-calcium-silicon oxides, and manganese sulfides, whereas a fine dispersion of titanium-based inclusions result in high HIC resistance [10], [12].

In this study, the hydrogen trapping capacity and associated hydrogen embrittlement susceptibility of two grades of linepipe steel skelps were compared: sour service X60 grade and standard service X70 grade, which were both provided by Evraz North America. The X60 grade steel (Fe-Nb-V) typically passes the NACE TM0284 HIC susceptibility testing, thereby qualifying it for sour service applications. However, the X70 grade steel (Fe-Nb-Ti) typically fails the HIC susceptibility testing, thereby disqualifying

it for sour service applications. Over the last several years there has been a depletion in sweet gas and an increase in consumption of sour gas, therefore increasing the demand for linepipe steels classified as sour service grade (highly HIC-resistant) steel [12]. Qualification of X70 steel as a sour service grade steel would help meet this demand, however, the current inability of the X70 grade steel to pass the NACE HIC susceptibility test prevents this. Both grades of steel provided by Evraz North America have been Ca treated, which has been reported to improve HIC resistance [12]. Ca addition prohibits the formation of MnS inclusions, which has proved to be a detrimental HIC susceptibility by serving as potent trapping sites for HIC initiation, by promoting the formation of fine spherical CaS inclusions. Additionally, Ca additions help to control the shape, quantity, and distribution of inclusions within the steel [13].

The goal of this comparative study is to first identify differences in the microstructure between the two grades of steel and then to relate differences in the hydrogen embrittlement susceptibility between the two grades of steel to the differences in microstructure features based on their capacity to trap hydrogen. ASPEX[®] analysis was conducted to characterize the type, quantify and distribution of the micrometer-sized inclusions present. TDS and hydrogen permeation testing was conducted after galvanostatic cathodic polarization to charge the steel with hydrogen to identify the various hydrogen traps present. Uniaxial tensile testing of samples with and without being subjected to hydrogen charging (galvanostatic cathodic polarization) pre-treatment was conducted to evaluate the hydrogen embrittlement (HE) susceptibility. Fractography using scanning electron microscopy (SEM) equipped with X-ray energy dispersive spectroscopy

(EDS) was conducted to identify the fracture modes and characterize inclusions of interest found on the fracture surfaces. Successful identification of the problematic microstructure features of the X70 grade steel will provide the platform on which to explore possible changes in the steelmaking practice that can be implemented to help reduce HIC susceptibility.

Chapter 2: Literature Review

2.1. Hydrogen-Induced Cracking

Hydrogen-induced cracking (HIC) is a type of environmentally induced cracking (EIC) caused by the entry of atomic hydrogen into the steel resulting in brittle mechanical fracture [14], [15]. Metallurgical heterogeneities act as traps in the steel matrix where atomic hydrogen accumulation occurs as atomic hydrogen diffuses through the steel [14]. HIC of pipeline steels in H₂S-containing environments can be explained by the theory of hydrogen embrittlement (HE) in the following steps [16]:

1. Evolution of hydrogen gas as a cathodic reaction during corrosion.
2. Atomic hydrogen absorption on the steel surface as part of the cathodic half-cell reaction sequence.
3. Diffusion of atomic hydrogen into the steel (instead of molecular gas formation).
4. Accumulation of atomic hydrogen at potential trapping sites.
5. Formation of molecular hydrogen gas by combination of atomic hydrogen.
6. Initiation of cracking by internal pressure of hydrogen gas and propagation of the crack.

A schematic provided by Shi et al. depicting hydrogen behaviour leading to HIC in steel is shown in Figure 2.1, and is based on the internal pressure theory proposed by Zapffe

et al. [16], [17]. A corrosion reaction between the steel surface and the sour environment causes atomic hydrogen to form, as part of the cathodic half-cell reaction. This atomic hydrogen diffuses into the steel where it can then be trapped by microstructural features acting as hydrogen trapping sites. Accumulation of the hydrogen atoms at hydrogen traps and subsequent combination to form hydrogen gas lead to increasing internal pressure and result in crack initiation and propagation and/or blister formation [10], [15], [16]. Grain boundaries, phase boundaries, micro-voids, dislocations, non-metallic inclusions, and precipitate particles are all heterogeneities within the steel microstructure that can act as hydrogen traps [10].

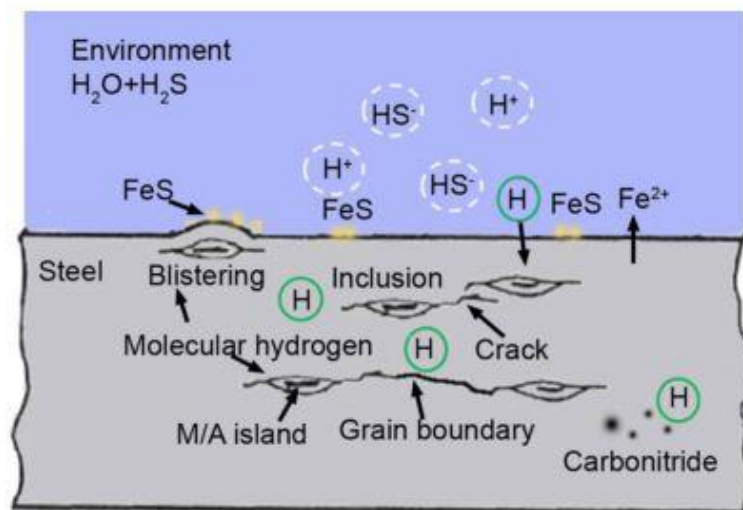


Figure 2.1: Schematic diagram illustrating common mechanisms of hydrogen introduction into steel [16].

Hydrogen traps can be reversible or irreversible, depending on whether the trapped hydrogen atoms are easily released or tightly bound. This can be measured as an activation or binding energy as listed in Table 2.1 [14], [18]–[21]. Activation and binding energies of

specific hydrogen traps can be measured through TDS analysis using a method based on the work of Lee et al. involving a simplification of the original formula by Kissinger [19], [20], [22]–[24]. Hydrogen traps with low energies are said to be reversible, whereas hydrogen traps with high energies are said to be irreversible at ambient temperatures, but become reversible at higher temperatures [8], [9]. Figure 2.2 shows a schematic of the energy levels of hydrogen atoms around trapping sites where E_n is the diffusion activation energy (kJ/mol) of hydrogen atoms in a normal lattice, E_s is the saddle point energy (kJ/mol), E_b is the trap binding energy (kJ/mol), E_a is the trap activation energy (kJ/mol), A is the trapping site, and B is the normal lattice site [18]. The activation energy, E_a , is that which is needed to escape from a trapping site. As Table 2.1 shows, grain boundaries, dislocations and microvoids have low binding energies and activation energies, therefore, classifying them as reversible traps. Non-metallic inclusions have high binding energies and activation energies, classifying them as irreversible traps.

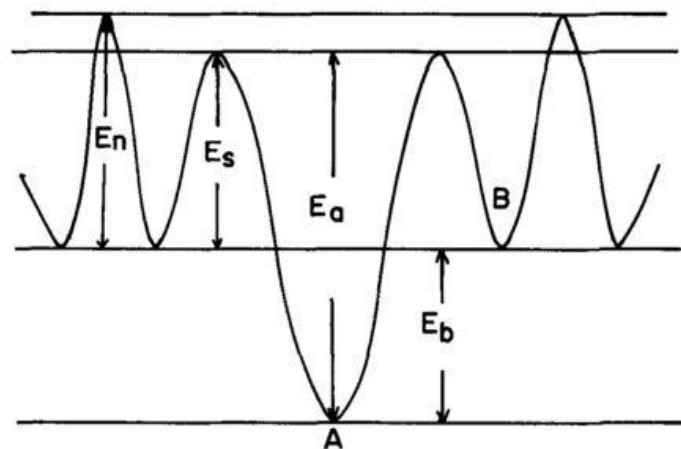


Figure 2.2: Energy levels associated with a hydrogen trap [11].

Table 2.1: Published data for activation energy of hydrogen escape for various traps in steel.

Trap Site	Activation Energy, E_a (kJ/mol)	Reference
Grain Boundary	17.2, 9.6*	[18]
Dislocation	26.8, 19.2*	[18]
Micro-void	35.15, 48.3, 27.6*	[18], [20]
Cementite Interface	18.35	[19]
Fe Oxide Interfaces	47.2	[19]
MnS Interfaces	72.3	[19], [20]
Al ₂ O ₃ Interfaces	78.96	[19]
TiC Interfaces	86.98, 95, 61*	[19], [21]
VC Precipitates	34	[21]
Precipitates Interfaces	23 to 48	[21]

*trap binding energies, E_b (kJ/mol)

Grain size (ferrite matrix) and different phases (pearlite, bainite, martensite) present in the microstructure has been reported to have an effect on the HIC susceptibility in steel [10], [11], [25]–[27]. Grain refinement of the ferrite matrix in steels is said to improve the resistance of steel to HIC due to an increased grain boundary area as a result of fine grains, increasing a short-circuited diffusion path for hydrogen atoms [8]. Hejazi et al. reports that the mobility of hydrogen atoms increases as grain size decreases due to a larger grain boundary per unit area, however a resulting increased density of nodes or junction points can reduce the overall mobility of hydrogen atoms by acting as potential hydrogen traps [10]. Therefore, due to these two opposing effects, an optimum grain size is required to result in a maximum hydrogen atom short-circuited diffusion coefficient [8], [10].

Linepipe steel microstructures can contain multi-phases including polygonal ferrite, acicular ferrite, pearlite, bainite and martensite, depending on the alloy composition and

the thermo-mechanical processing route [8], [26], [27]. Hard phases such as cementite, martensite and dislocation-rich acicular ferrite increase stress zones present in the microstructure, causing absorbed hydrogen atoms to become trapped, in which HIC can take place if the trapped hydrogen reaches the critical concentration necessary for crack initiation [10]. Phase hardness increases in the following order: ferrite < pearlite < bainite < martensite. The associated hydrogen trapping efficiency also increases in that same order [10], [12], [28]. Park et al. investigated the susceptibility of HIC and sulfide stress cracking (SSC) in steels containing various fractions of bainite. It was reported that the steel containing the highest fraction of bainite had a significant increase in HIC susceptibility compared to those steels with lower fractions of bainite or no bainite present in the microstructure [27]. It has been reported by multiple authors that acicular ferrite shows lower HIC susceptibility due to its excellent crack propagation inhibition as a result of fine dispersed carbonitrides and high-density tangled dislocations serving as hydrogen traps [9], [16], [29], [30]. The high-density tangled dislocations act as beneficial hydrogen traps by distributing the trapped hydrogen evenly and thereby preventing the hydrogen accumulation from reaching the critical value that causes HIC occurrence [16], [31]. Dong et al. also states the benefits of acicular ferrite in lowering HIC susceptibility in steel, but mentions the detrimental effects of acicular ferrite when mixed in a microstructure containing polygonal ferrite. It is noted that when the microstructure is polygonal ferrite mixed with acicular ferrite, hydrogen accumulates at the grain boundaries of the polygonal ferrite, which increase the susceptibility of HIC [30]. Shi et al. also comments on the effects of acicular ferrite, in which bainitic ferrite within the acicular ferrite exhibits straight lath

boundaries acting as a hydrogen trap. Once the hydrogen content within the trap accumulates to a critical/threshold concentration, HIC will occur [16]. Therefore, while acicular ferrite has been reported to be a beneficial microstructural feature from a HIC perspective, there is some contradiction in the literature about the exact role acicular ferrite plays.

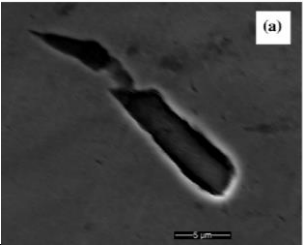
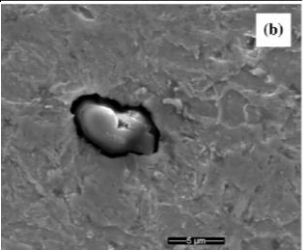
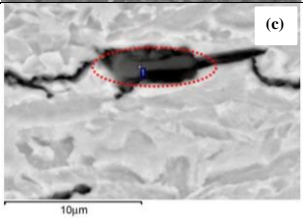
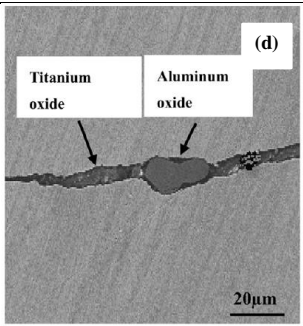
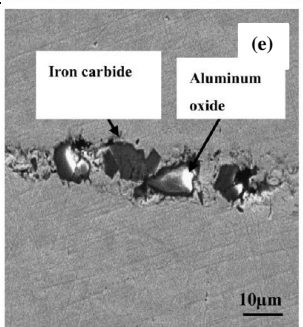
Centreline segregation of phases has also been discussed in the context of HIC susceptibility by Moon et al., in which it was mentioned that phases of a higher hardness are typically segregated to the centreline of the steel plate during the hot rolling process [12]. Similarly, the centreline of the steel plates contain a different grain size than the quarterlines. The grain size in the centreline is larger than that contained at the quarterlines due to the cooling stage after rolling, where the centre of the plate remains at higher temperatures for a longer time due to uneven heat extraction between the surface and centre of the steel plate [32]. Due to segregation of harder phases to the centreline of the steel plate, as well as the resultant coarser grains, it is not that surprising that that the centreline of steel plates has increased susceptibility to HIC relative to the quarterline depths [12], [33].

It has been reported that linepipe steels contain Al_2O_3 , complex Al-Ca-Si oxides, oxides and oxysulfides of Ca and Al, oxides of Mg and Mn, spinel-type double oxide $\text{FeO}\cdot\text{Al}_2\text{O}_3$, titanium oxide, ferric carbide, MnS, complex (Fe, Mn)S, and nitrides and carbonitrides of Ti and Nb [10]. HIC susceptibility in steels is increased with the presence of larger inclusions, clusters or stringers of oxides, and larger amounts of inclusions [10], [25]. It has also been reported that HIC is associated with inclusions enriched in Al or Si in

linepipe steel, and that inclusions enriched in Al were the most harmful due to being more brittle and incoherent with the metal matrix [8], [12]. Ti-based inclusions are observed to be smaller and therefore less problematic than oxides and other inclusions in the steel matrix [30]. Beidokhti et al. have reported that having a dispersion of fine Ti-based inclusions, particularly Ti-carbonitrides, are beneficial traps in the steel matrix due to their ability to provide dispersion strengthening and behave as innocuous hydrogen traps, which can provide numerous sites for redistribution of hydrogen therefore precluding the accumulation of critical hydrogen concentrations at detrimental trapping sites [11]. The same author also reported that TiC particles maintain a distributed hydrogen profile thereby delaying the occurrence of cracking, or can delay the onset of HE to higher bulk concentrations at longer times [11].

Some problematic inclusions reported in literature are shown in Table 2.2 [25], [34], [35]. HIC susceptibility in steels is increased with an increase in the amount, area and volume fraction of inclusions [25]. Cracks as a result of hydrogen charging were reported to initiate in the absence of external stress primarily at inclusions, such as Al oxides, Ti oxides, and ferric carbides [34], [35].

Table 2.2: Problematic inclusions reported in literature, (a) elongated Si-enriched inclusion, (b) Al oxide inclusion with small amounts of Mg and Ca, (c) inclusion containing globular Al_2O_3 with elongated MnS, (d) inclusion containing Ti oxide and Al oxide, (e) inclusion containing iron carbide and Al oxide [25], [34], [35].

Image of Inclusion	Significance
 <p>(a)</p>	<ul style="list-style-type: none"> - Inclusion not well coherent to steel matrix. - Strong hydrogen trap between inclusion and base metal followed by crack initiation.
 <p>(b)</p>	<ul style="list-style-type: none"> - Inclusion not well coherent to steel matrix. - Strong hydrogen trap between inclusion and base metal followed by crack initiation.
 <p>(c)</p> <p>10µm</p>	<ul style="list-style-type: none"> - Inclusion not well coherent to steel matrix - Hydrogen trapping reported to increase with amount, area and volume fractions of inclusions.
 <p>(d)</p> <p>Titanium oxide</p> <p>Aluminum oxide</p> <p>20µm</p>	<ul style="list-style-type: none"> - Elongated inclusion containing Al oxide and Ti oxide. - Crack initiation was found to be associated with this type of inclusion due to hydrogen-enhanced stress concentration.
 <p>(e)</p> <p>Iron carbide</p> <p>Aluminum oxide</p> <p>10µm</p>	<ul style="list-style-type: none"> - Inclusion containing ferric carbide. - Crack initiation was found to be associated with this type of inclusion.

2.2. Comparison of X60 and X70 Linepipe Steel

Chemical requirements and tensile requirements as stated in the API specification are shown in Table 2.3 and Table 2.4 [36]. Typically, X60 grade steel contains higher amounts of V and lower amounts of Nb and Ti than X70 grade steel [26]. The increase in Nb and Ti in X70 grade steel aids in grain refinement within the microstructure, resulting in the X70 steel having an overall smaller grain size than the X60 steel [26], [37]. The API specification did not indicate requirements for Ca and Al contents for linepipe steel grades. The X70 steel is also a higher-strength steel compared to the X60, which increases its appeal in the oil and gas industry due to improved mechanical resistance, however, it is more susceptible to environmental cracking than lower-strength alloys [5], [26], [33]. Higher-strength steels aid in the pipe making process due to their ability to be produced at smaller wall thicknesses, and therefore the development of high-strength pipeline steels with low HIC susceptibility is essential [16]. The increase in hydrogen embrittlement (degraded mechanical properties) susceptibility in high-strength steels is attributed to the larger number of potential crack initiation sites, and the increased stress level acting at these sites [22].

Table 2.3: Chemical requirements for API 5L linepipe steel [36].

Grade	C_{max}	Mn_{max}	P_{max}	S_{max}	Ti_{max}
X60	0.26	1.40	0.030	0.030	0.04
X70	0.26	1.65	0.030	0.030	0.06

Table 2.4: Tensile requirements for API 5L linepipe steel [36].

Grade	Minimum Yield Strength (MPa)	Minimum Ultimate Tensile Strength (MPa)
X60	414	517
X70	483	565

X60 steel tends to be manufactured via traditional hot-rolling, while the X70 steel typically undergoes thermo-mechanical processing and suitable rolling. The thermo-mechanical processing in the X70 steel also contributes to the grain refinement, and improved strength and toughness [26]. The X60 steel has been reported to typically contain a ferrite-pearlite microstructure while the X70 steel typically contains a ferrite-bainite microstructure, where the presence of acicular ferrite, or bainite, or both has been observed in the X70 steel microstructure [7], [26], [38].

Mohtadi-Bonab et al. investigated HIC behaviour of X60 steel compared to X70 steel. It was determined that the X60 microstructure contained polygonal ferrite, the X70 microstructure contained acicular ferrite, and bainite and small particles of martensite were observed in both steels. To examine the HIC susceptibility in both grades, three HIC parameters were considered, where a is the crack length (m), b is the crack thickness (m), W is the section width (m), and T is the test specimen thickness (m) [33]:

$$\text{Crack Length Ratio, CLR} = \frac{\sum a}{W} \quad 2.1$$

$$\text{Crack Thickness Ratio, CTR} = \frac{\sum b}{T} \quad 2.2$$

$$\text{Crack Sensitivity Ratio, CSR} = \frac{\sum(a \times b)}{(W \times T)} \quad 2.3$$

It was reported that all observed HIC parameters had higher values in the X70 steel than those determined in the X60, indicating that the X70 samples were more susceptible to HIC than the X60. Acceptable limit values of CLR, CTR and CSR should be less than 15%, 5%, and 2%, respectively, but the average values determined from the HIC test in the X70 steel was 42%, 8%, and 3%, respectively, indicating that the X70 steel was highly susceptible to HIC. Average HIC parameter values for CLR, CTR and CSR determined from the HIC test in the X60 were 8%, 2%, and 1%, respectively, showing a much lower HIC susceptibility in the X60 steel [33]. Micro-hardness measurements were also done on the X60 and X70 steel samples to compare hardness variations across the cross sections of the plates. Insignificant variations of hardness were detected in the X60 steel, but very different hardness values were observed through the X70 cross section.

Mohtadi-Bonab et al. also reported inclusions observed in the X60 and X70 grades, where no MnS inclusions were detected in the X60 steel and <4% of MnS inclusions were detected in the X70 among all inclusions. Mixed oxide inclusions were found in both grades which include: Si-Ca-Al-Mg-O, Al-Ca-Ti-O, Mg-Al-Ca-O, Al-Mg-O, Mg-Ti-O [33]. It was also reported by Mohtadi-Bonab et al. that X70 pipeline steel was observed to contain inclusions enriched with either Al or Si [8]. As previously mentioned, inclusions containing Al are known to be detrimental heterogeneities within the steel matrix, where these inclusion types as well as other inclusions are irreversible trapping sites and serve to initiate cracks. As hydrogen atoms diffuse into the steel, they become trapped at irreversible

trapping sites and combine together to make hydrogen molecules, which accumulate inside the void between the inclusion and metal matrix resulting in an increased pressure in the area thus initiating cracks [33]. Reversible traps, such as grain boundaries, contain a high content of mobile hydrogen which have the ability to accumulate around the crack tip thus propagating cracks once initiated [33]. Due to this phenomenon, Mohtadi-Bonab et al. concludes that the role of reversible trapping sites outweighs the role of irreversible trapping sites on HIC susceptibility [33].

2.3. Role of Ca Treatment

Ca treatment is beneficial in steel production not only by preventing nozzle blockage in continuous casting but also by modifying inclusion formation within steel [39]. HIC is greatly affected by the cleanliness of the steel. It is widely known that MnS inclusions are detrimental features that act as crack initiation sites when the steel is exposed to a hydrogen-containing environment. Additionally, inclusion size can greatly affect the susceptibility of HIC, where it has been shown that larger areas and volume fractions of inclusions increase the steel's susceptibility to HIC [12]. To improve steel cleanliness, alternative methods, including Ca treatment and/or producing steels with low S content (<0.002%), have been suggested in order to reduce the harmful effects of sulfide inclusions [2]. Calcium treatment results in better control over the shape, size, and distribution of non-metallic inclusions, and prohibits the formation of long stringer types of MnS inclusions by

facilitating the formation of spherical CaS inclusions [13]. Yin et al. reported on two main inclusion types, type A and type B, which increase HIC susceptibility in steel: type A are MnS inclusions, and type B are mainly CaO-Al₂O₃, CaO-CaS-Al₂O₃, CaS-CaO type inclusions [15]. The occurrence of type B inclusions are further described within this section.

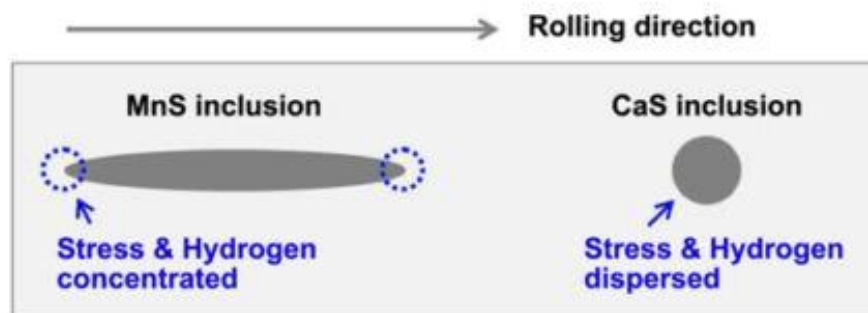


Figure 2.3: Schematic of HIC initiation sites based on inclusion geometry [12].

Moon et al. illustrated the mechanism of HIC occurrence, Figure 2.3, showing that elongated MnS inclusions have sharp edges where hydrogen atoms and stress can accumulate causing crack initiation, whereas spherical CaS inclusions result in a dispersion of hydrogen atoms and stress resulting in reduced [12]. Furthermore, it was also reported by Moon et al. that MnS inclusions are larger and contain a higher volume fraction than the fine CaS inclusions that are formed as a result of Ca treatment [12]. The type, shape, size, and distribution of inclusions all seem to matter. A systematic study in which these parameters are independently varies needs to be done to best differentiate potency.

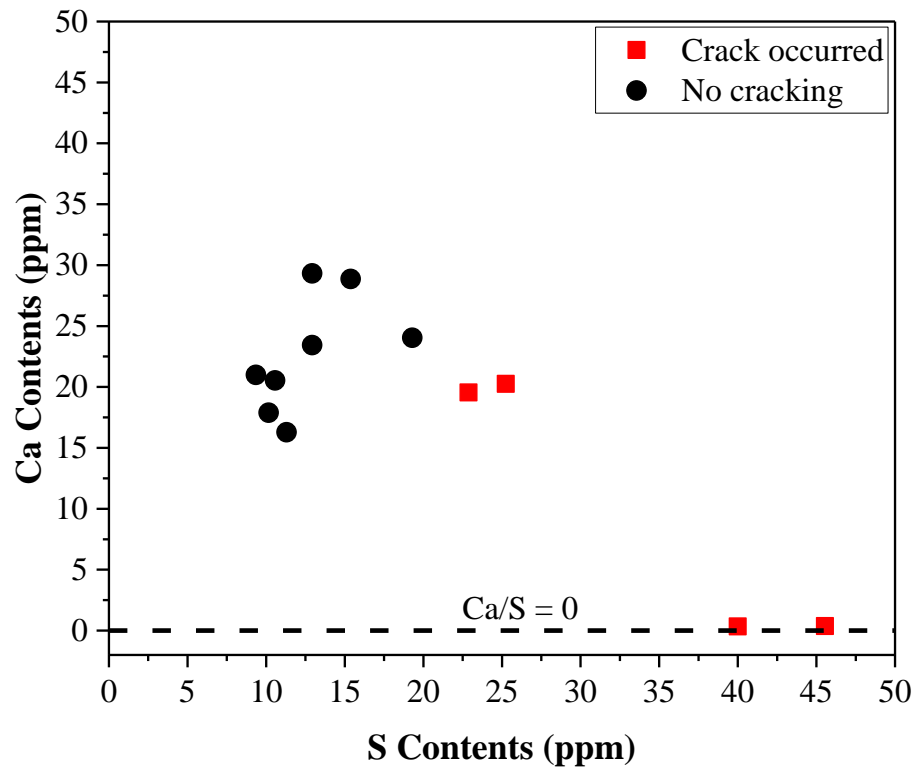


Figure 2.4: HIC susceptibility of steel containing various Ca/S ratios [12].

HIC resistance is sensitive to the resulting Ca/S ratio in the steel after Ca treatment, as shown in Figure 2.4, with cracking susceptibility observed based on steels containing various Ca/S ratios [12]. From these experiments performed by Moon et al. it was concluded that HIC susceptibility decreased when the stoichiometric Ca/S ratio was higher than 1.25, above which all the elemental S is not formed into MnS, but rather is formed into CaS [12].

Type B inclusions are the result of Ca treatment. The effects of Ca treatment are reduced by re-oxidation of liquid steel after Ca treatment resulting in a significant amount of inclusions being generated, as well as inclusions changing from low melting Ca

aluminates to Al_2O_3 -rich Ca aluminates [15], [39]. Ca treatment modifies solid Al_2O_3 inclusions to liquid CaO- Al_2O_3 complex inclusions, which prevents nozzle clogging in continuous casting, however, excessive addition of Ca during treatment can lead to the clogging of the nozzle and tundish gate plates due to an increase in the number of Ca-modified inclusions [15], [39], [40]. This further emphasizes the importance of a suitable Ca/S ratio associated with Ca treatment. It has also been reported that when the Ca/S ratio is too low in Ca treated steel, the production of elongated MnS inclusions occur, but when the Ca/S ratio is too high, a cluster of Ca-O-S inclusions are formed [15]. The relationship between Ca/S ratio and the formation of MnS and Ca-O-S inclusion clusters is shown in Figure 2.5, where it was shown that the Ca/S ratio should be controlled between 2~5 in order to prevent the formation of these inclusions [15]. Type A inclusions are reported to be controlled after reducing the sulfur content in steels and Ca treating, however, type B inclusions still pose a threat to HIC resistance in pipelines which require further investigations to focus on the control of these inclusion types [15].

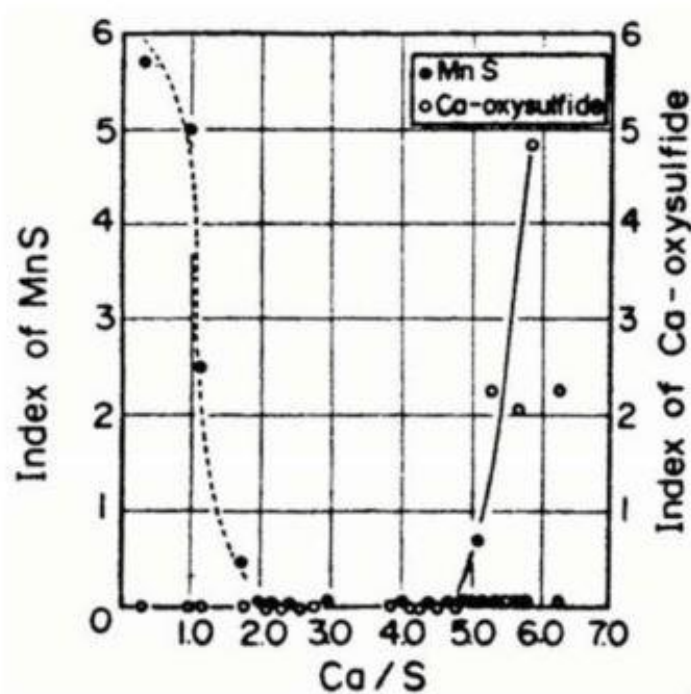


Figure 2.5: Relationship between Ca/S ratio and formation of inclusions [15].

2.4. Fracture Mechanics

There are distinctive fractographic features, both macroscopic and microscopic, that can be used to distinguish the difference between various fracture mechanisms, and can sometimes indicate how a fracture occurred [28], [41]. Table 2.5 summarizes macroscopic and microscopic features that can be observed on a fracture surface and what it may indicate in regards to the fracture mechanisms [28].

Table 2.5: Macroscopic and microscopic fractographic features [28].

Mark/Indication	Implication
Visible distortion.	Plastic deformation exceeded yield strength and may indicate instability or post-failure damage.
Visible nicks and gouges.	Possible crack initiation site.
Both flat fracture and shear lips present on fracture surface.	Crack propagation direction is parallel to shear lips. This also indicates mixed-mode fracture.
Radial marks and chevrons (V-shape).	Points toward crack initiation site and shows crack propagation direction.
Ratchet marks.	More likely in cyclic loading. Indicates fracture initiation site.
Dimpled fracture surface.	Ductile overload fracture at this location.
Faceted fracture surface.	Brittle cleavage fracture or possible SCC fracture.

Microscopic examination of fracture surfaces can be achieved through the use of an SEM. Figure 2.6 consists of SEM images showing three basic types of overload fractures and the distinctive microscopic features associated with each fracture type. The three modes of overload fracture shown are: brittle fracture by intergranular separation, transgranular brittle fracture (cleavage), and transgranular ductile fracture (microvoid coalescence) [28]. These differences in the topological features of a fracture surface can be easily imaged in the SEM.

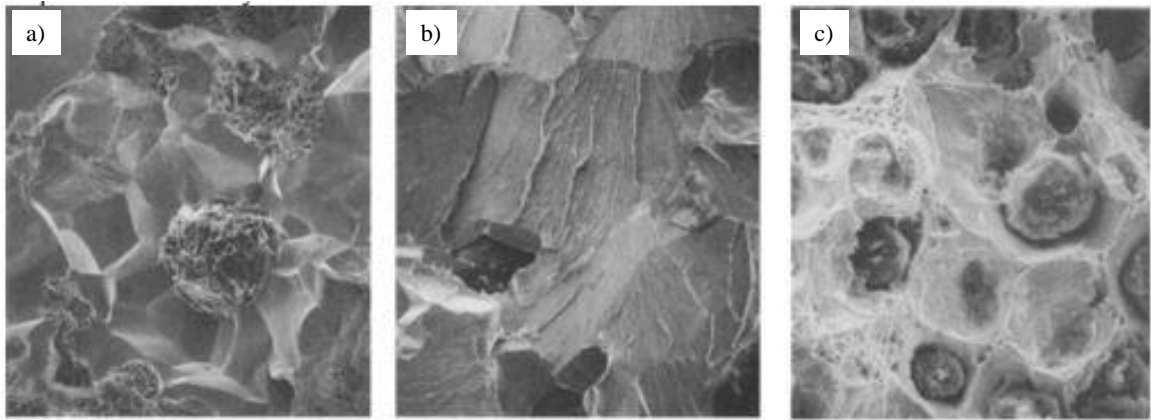


Figure 2.6: SEM imaged comparing the basic types of overload fracture: (a) intergranular fracture, (b) transgranular fracture by cleavage, (c) ductile fracture with equiaxed dimples [28].

In addition to the fracture surface topography, the tensile cross-sectional fracture geometry is also very indicative of whether or not the fracture is brittle or ductile. Figure 2.7 shows the difference in the cross-section of a fractured tensile when the fracture mode is brittle or ductile. Brittle fractures experience very little necking and result in a fracture with a slip path at 45° to the tensile axis, however, ductile fractures undergo necking and result in shear lips which are at a 45° slant to the maximum tensile stress [42], [43]. The occurrence of shear lips in a ductile fracture is observed in Figure 2.8(a), while shear lips are not observed in the brittle fracture imaged in Figure 2.8(b).

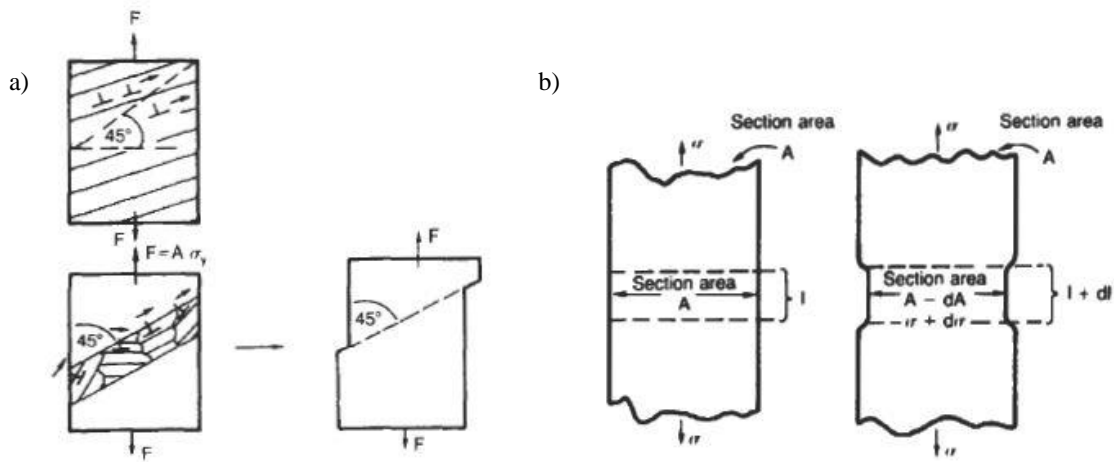


Figure 2.7: Schematic image of (a) brittle fracture with slip path at 45° to tensile axis, and (b) ductile material undergoing necking during plastic deformation [42].

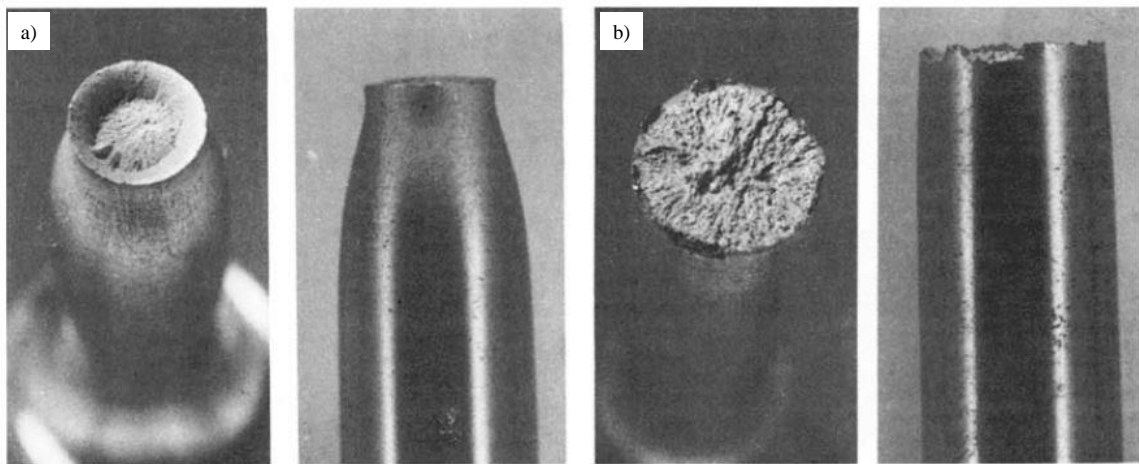


Figure 2.8: Images of (a) ductile and (b) brittle tensile fractures [43].

Ductile fracture typically results in a cup-and-cone fracture as shown in Figure 2.8(a) [43]. As stress is being applied to the tensile specimen, voids are developed in the necked region, and the coalescence of these voids produce an internal crack by normal

rupture. Final separation of the tensile occurs by shear rupture, which produces the shear lips along the edge of the fracture surface [43].

Brittle fractures are characterized by rapid crack propagation, and exhibit little or no necking as shown in Figure 2.8(b) [43]. The mechanisms associated with brittle fracture may exhibit chevron or herringbone patterns that indicate the fracture origin and direction of rapid fracture [28].

2.5. Opportunities for Research

Controlling the Ca/S ratio and alloy chemistry of pipeline steels is an excellent engineering approach to control HIC susceptibility, however it does not explain the mechanism nor does it provide mechanistic insight into what microstructural features are controlling HE susceptibility. X60 grade steel has been compared to X70 grade steel on the basis of linking hydrogen permeation to HIC susceptibility using NACE standard TM0284 testing and analyzing with SEM-EBSD and SEM-EDS methods [6], [33]. Excellent information has been reported on hydrogen traps that control HIC propagation by linking electron backscatter diffraction (EBSD) to HIC susceptibility, but there is limited insight into traps that control the initiation of HIC. There was a missed opportunity by Mohtadi-Bonab et al. to combine TDS experimentation along with ASPEX[®] inclusion analysis with their hydrogen permeation analysis to better investigate and understand the role of hydrogen traps [33]. TDS gives information regarding reversible and irreversible traps present in the

steel matrix, and ASPEX[®] gives information regarding the quantity, size, and area fraction of inclusions which gives better statistics to better understand contributions of the microstructure to HIC susceptibility.

This research aims to identify problematic microstructural features acting as hydrogen traps that serve to increase the HE susceptibility, and to compare the behaviour of HE susceptibility between two kinds of Ca treated pipeline steel: X60 grade steel skelp and X70 grade steel skelp. This involved the microstructural characterization of the as-received steel skelp using LOM, SEM, and ASPEX[®] analysis which gave information regarding grain size, phases in microstructure, and composition, shape and distribution of inclusions within the steel skelp. TDS and hydrogen permeation measurements were done to determine the types of hydrogen traps present as well as the potency of these traps in the steel skelp. The hydrogen trapping capacity was then linked to the HE susceptibility by comparing the uniaxial tensile behaviour of samples with and without hydrogen charging applied as a pre-treatment step where SEM-EDS techniques were then used to identify fracture modes and characterize inclusions of interest found on the fracture surfaces.

Chapter 3: Experimental Methods

3.1. Materials

In this work, the hydrogen embrittlement susceptibility of linepipe steel skelp was compared. Sour service X60 grade and standard service X70 grade linepipe steel skelp material were provided by Evraz North America; where the X60 grade steel typically passes hydrogen-induced cracking (HIC) susceptibility testing (NACE TM0284 [6]), and the X70 grade steel has problems passing HIC susceptibility testing. The X60 skelp was manufactured using the EAF process, under thick slab conditions using a curved mold continuous caster, and the X70 skelp was manufactured using the BOF process, under thick slab conditions using a continuous caster [44]. The skelp material was provided in the as-rolled condition, wherein the X60 skelp material was rolled down to 9.0 mm and 12.0 mm thicknesses, and the X70 skelp sample was rolled down to 15.9 mm thickness.

Table 3.1 provides the chemical composition of X60 and X70 skelp material. The composition of the X60 skelp was provided by Evraz North America, whereas the composition of X70 skelp was determined by inductively coupled plasma - optical emission spectroscopy (ICP-OES) using a VISTA-PRO CC Simultaneous ICP-OES instrument here at McMaster University. The C and S concentrations in the X70 skelp were determined using a LECO CS-444 instrument coupled with a LECO HF-400 instrument. It was determined that the Ca/S ratio in the X60 skelp was ~4.3 and in the X70 skelp was ~0.3.

Both grades of linepipe steel were Ca treated, although the apparent Ca content in the X70 skelp is relatively low. The X60 skelp contained lower amounts of C, Mn, and Nb, but a higher amount of V, as alloying elements relative to the X70 grade. The composition of both grades are within the ranges specified by the American Petroleum Institute (API) [36].

Table 3.1: Chemical composition of linepipe steel skelp material.

Grade	Composition (wt.%)									
	C	Si	Mn	V	Nb	Ti	Ca	S	P	Ca/S
X60	0.027	0.17	1.32	0.066	0.044	0.01	0.0034	0.0008	0.007	4.3
X70	0.033	0.13	1.57	0.004	0.067	0.016	0.001	0.0039	0.008	0.3

3.2. Microstructure Characterization

Small rectangular samples extracted from X60 and X70 skelp materials were both hot-mounted in phenolic resin and cold-mounted in epoxy resin to isolate the orthogonal planes for a subsequent metallographic examination. Hot-mounted samples included orthogonal planes normal to the rolling direction (RD), transverse direction (TD), and normal direction (ND), whereas cold-mounted samples included just the plane (TD-ND) normal to the RD. Figure 3.1 illustrates a schematic showing the orientation of these planes in the steel skelp material. The working surface planes exposed in the mounted samples were ground to 1200-grit finish using SiC paper, polished up to 0.25 μm finish using water-free lubricants and diamond slurry, etched using 2.5% nital solution for about 5 s, rinsed with deionized water and ethanol, and then dried in a warm air stream. The hot-mounted samples were

imaged using a Keyence VH-ZST dual objective zoom lens light optical microscope (LOM) to document the typical appearance of the microstructure in each case. Grain size measurements were made on the RD-ND plane at the $\frac{1}{4}$, $\frac{1}{2}$, and $\frac{3}{4}$ through-thickness depth locations. The average grain size was determined using the Heyn lineal intercept procedure as described in ASTM E112-13 [45]. The cold-mounted samples (RD-ND and TD-ND planes) were imaged using a JEOL JSM-7000F scanning electron microscope (SEM) operated at an accelerating voltage of 10 kV and a working distance of 10 mm to help confirm the major phases present in material: ferrite and pearlite in the X60 grade and ferrite and bainite in the X70 grade.

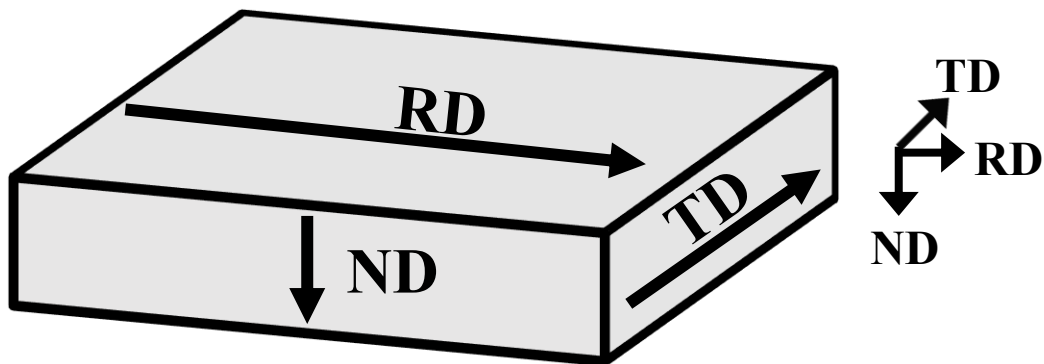


Figure 3.1: Schematic showing orientation and labeling of planes of the steel skelp material.

The type, count, and average size of inclusions present in both steel skelp materials were analyzed using the ASPEX[®] technique, which was made available for use by ArcelorMittal Dofasco (Hamilton, ON). The technique is an automated feature analysis (algorithm) for particle characterization using conventional X-ray energy dispersive

spectroscopy (EDS) coupled with scanning electron microscopy (SEM). Rectangular (11 mm × 30 mm × 25 mm) samples exposing the RD-ND plane and the TD-ND plane were prepared from the X60 and X70 steel skelp for this purpose. The working plane surfaces were ground to 220-grit finish using MD-Piano diamond disc, polished up to 1 μm finish using water-free lubricants and diamond slurry, rinsed with deionized water and ethanol, and then dried in a warm air stream. The analysis was conducted along the ¼, ½, and ¾ depths on both the RD-ND and ND-TD planes of both steel skelps. Images were acquired using an accelerating voltage of 20 kV and a working distance of 16.5 mm. Data received from this analysis included the total count, average diameter, and area of each type of inclusion detected, with limitations that inclusions containing a maximum diameter of less than 2 μm were not detected. No standard deviation data were provided with the results.

A complementary ‘spot check’ analysis of the inclusions present in both steel skeps was also conducted using SEM-EDS here at McMaster University. A set of cold-mounted samples exposing the RD-TD plane extracted from the ¼, ½, and ¾ depth were prepared from the X60 and X70 steel skeps for the SEM-EDS examination. Samples were cold-mounted, polished and etched in the manner described above. Prior to SEM-EDS analysis, the working surfaces were coated with a carbon film in order to prevent major charging once irradiated with the electron beam. The working surfaces were imaged using a JEOL JSM-7000F SEM operating at an accelerating voltage of 10 kV and a working distance of 10 mm. EDS was used to obtain elemental maps and point analysis of inclusions imaged from each working surface using AZtec Version 3.3 Oxford Instruments software.

3.3. Diffusible Hydrogen Characterization

The diffusible hydrogen characterization in both the X60 and X70 steel skelp material was evaluated using both thermal desorption spectroscopy and hydrogen permeation measurements. Both sets of measurements were conducted in collaboration with Dr. Fateh Fazeli at CanmetMATERIALS (Hamilton, ON).

For the thermal desorption spectroscopy measurements, disk-shaped (10 mm in diameter and 1 mm in thickness) samples were prepared from the $\frac{1}{4}$, $\frac{1}{2}$, and $\frac{3}{4}$ depths of X60 and X70 steel skelps, Figure 3.2. Prior to testing, both working surfaces of the disk sample (front and back faces) were ground to 600-grit using SiC paper and water as a lubricant to remove contaminants and to yield a reproducible surface finish for replicate testing. A steel wire was then spot-welded to the curved edge of the sample to apply the charge during the galvanostatic cathodic polarization hydrogen charging pre-treatment step.

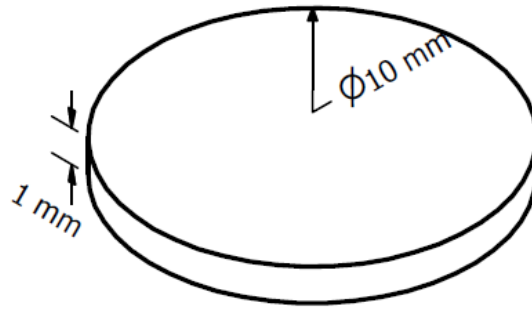


Figure 3.2: Flat disk samples used for thermal desorption spectroscopy measurements.

Samples were charged with hydrogen via galvanostatic cathodic polarization using a Gamry Reference 600 potentiostat, where the sample served as the working electrode and a graphite rod served as the counter electrode, Figure 3.3. Hydrogen charging of the samples was conducted in a solution comprising 0.1 N NaOH + 0.15 g/L As_2O_3 at a pH \sim 12.6 and was prepared from As_2O_3 powder, NaOH pellets, and deionized water. The As_2O_3 addition served as the hydrogen recombination poison for this set of measurements, and has been used by CanmetMATERIALS in the past as an effective hydrogen poison [34], [46]. X60 steel samples were galvanostatically polarized in the test solution for 2 h (as suggested by Dr. Fateh Fazeli) using an applied cathodic current densities of -2 mA/cm^2 , -5 mA/cm^2 , and -10 mA/cm^2 , whereas the X70 steel samples were galvanostatically polarized in the test solution for 2 h using an applied cathodic current density of -10 mA/cm^2 .

After the hydrogen charging pre-treatment step, samples were briefly stored in acetone solution while being transferred to a Carbolite MTF Tube Furnace equipped with

an E1151 Type 301 Controller with a quartz tube of 1 cm diameter. The transfer time of the sample from charging to heating in the furnace was less than 3 minutes. The sample (one per test) was heated from room temperature to 400°C using a heating rate of 10°C/min. while simultaneously measuring the hydrogen gas released during heating using a HYDROSTEEL[®] 6000 probe. Nitrogen gas was purged through the tube furnace at a flow rate of 27 cm³/min. for the duration of testing. A photographic image of the thermal desorption spectroscopy apparatus is provided in Figure 3.4. This process was performed twice on samples prepared from the three through-thickness depths of both steels, using freshly prepared test solutions for galvanostatic cathodic charging (pre-treatment) and samples. The HYDROSTEEL[®] probe is a non-destructive instrument used to measure the hydrogen gas flux from the steel sample in a stream of air, and the data obtained includes a measurement of hydrogen gas flux within a tolerance of ± 2 pL/cm²/s, and the time that each measurement was recorded [47], [48]. This recorded time was then converted to a temperature value by the corresponding heating rate used with the furnace. No post-exposure examination of the TDS samples was conducted.

The results obtained from thermal desorption spectroscopy measurements of X60 samples gave an indication the galvanostatic hydrogen charging pre-treatment testing conditions necessary to saturate the steel skelp material with hydrogen, and thus provided the pre-treatment parameters used for the hydrogen permeation measurements. This was done using the Ideal Gas Law to calculate the total diffusible hydrogen from TDS using various charging conditions in order to detect when hydrogen saturation occurred in the steel matrix (Equations 3.1 to 3.4). J is the hydrogen flux (pL/cm²/s), n_H is the number of

moles of hydrogen (mol), P is the pressure (atm), R is the gas constant (L·atm/K·mol), T is the temperature (K), m_H is the mass of hydrogen (g), M_H is the molar mass of hydrogen (g/mol), m_{sample} is the mass of the sample (g), and $PPM_{mass,H}$ is the total diffusible hydrogen (ppm).

$$\text{Total H Released} = \int J \, dt \quad 3.1$$

$$n_H = \frac{(\text{Total H Released})(10^{-12})P}{RT} \quad 3.2$$

$$m_H = n_H M_H \quad 3.3$$

$$PPM_{mass,H} = \frac{m_H}{m_{sample}} \times 10^6 \quad 3.4$$

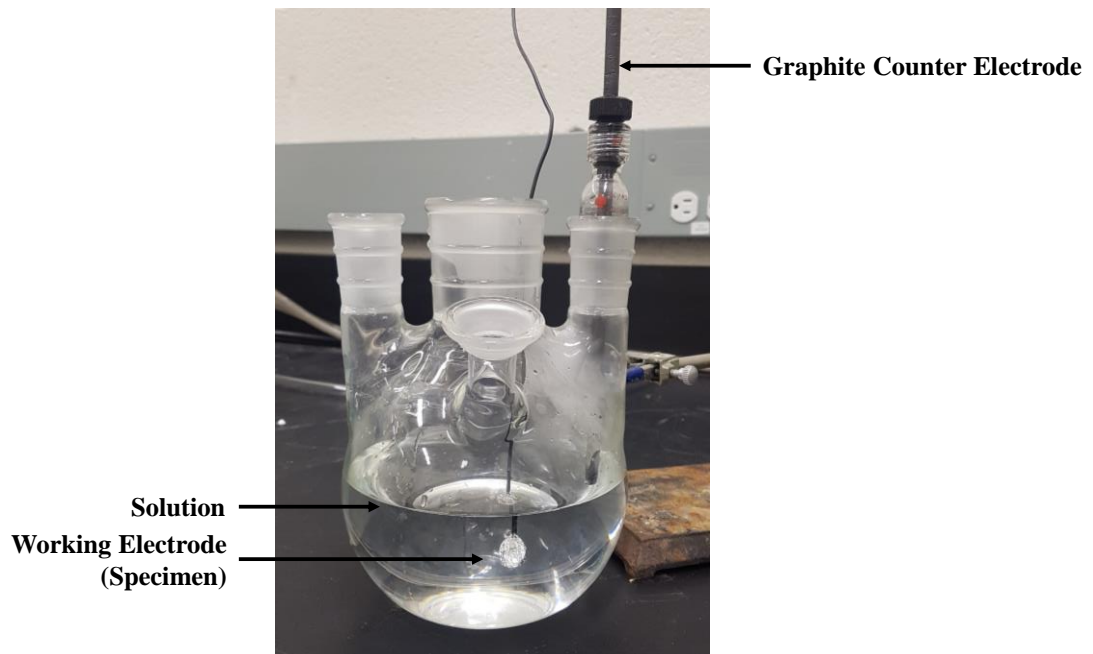


Figure 3.3: Experimental apparatus used to charge samples with hydrogen via galvanostatic cathodic polarization for subsequent TDS measurements.

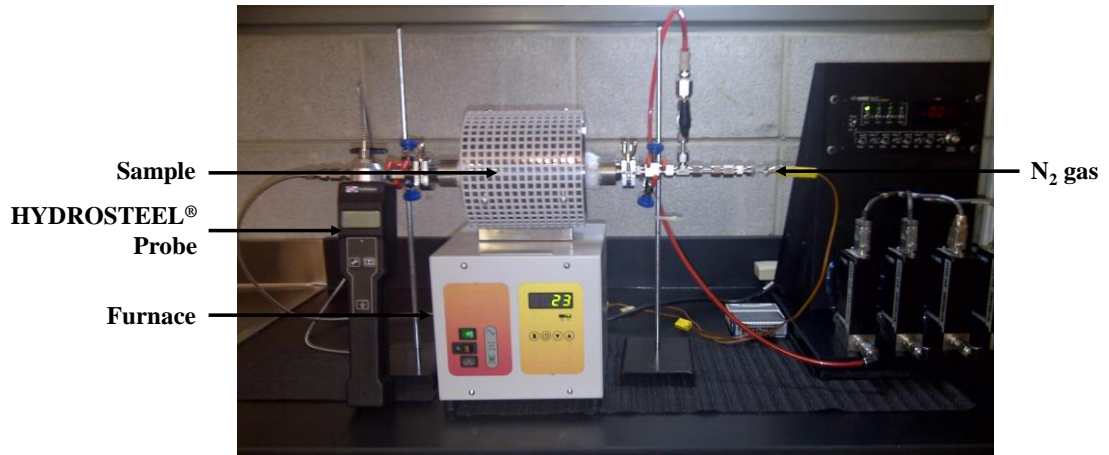


Figure 3.4: Experimental apparatus used for thermal desorption spectroscopy measurements (courtesy CanmetMATERIALS).

For the hydrogen permeation measurements, rectangular samples (80 mm × 95 mm × 2 mm) were prepared from the $\frac{1}{4}$, $\frac{1}{2}$, and $\frac{3}{4}$ depths of X60 and X70 steels, Figure 3.5. Prior to testing, the working surfaces (front and back faces) were ground to 600-grit using SiC paper and water as a lubricant to remove contaminants and to yield a reproducible surface finish for replicate testing.

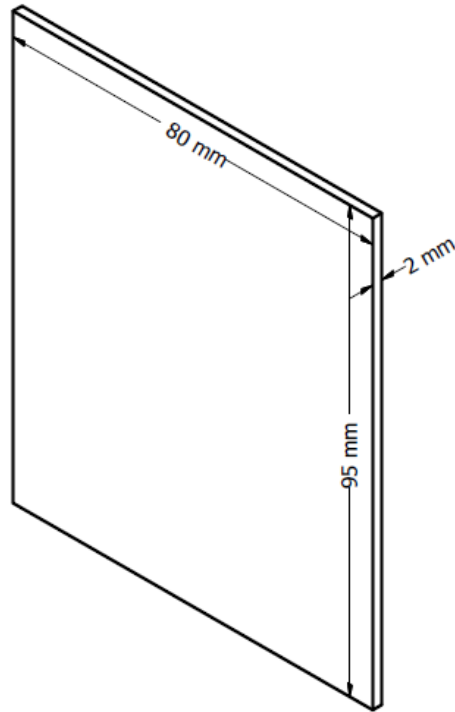


Figure 3.5: Rectangular plate samples used for hydrogen permeation experiments.

A one-sided corrosion cell was used for hydrogen charging (by galvanostatic cathodic polarization) of the samples, where the sample served as the working electrode, a saturated calomel electrode (SCE) served as the reference electrode, and platinum wire served as the counter electrode. The utilized cell design allowed for the simultaneous measure of hydrogen flux during galvanostatic polarization by exposing one side of the rectangular sample to the same hydrogen poison solution utilized in for the thermal desorption spectroscopy measurements and connecting the HYDROSTEEL[®] probe with a circular collector plate to the other side of the sample. A photographic image of the experimental apparatus is provided in Figure 3.6. Hydrogen permeation experimentation was conducted using a charging current density of -10 mA/cm^2 , as that was determined to

be when hydrogen saturation occurred from thermal desorption results. No post-exposure examination of the samples was conducted.

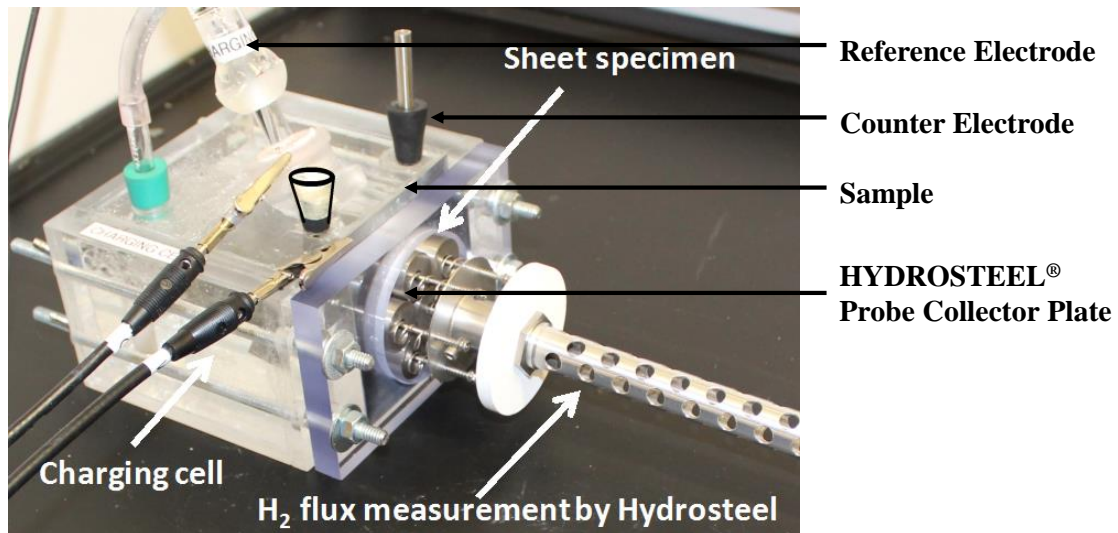


Figure 3.6: Experimental apparatus used for hydrogen permeation measurements (courtesy of CanmetMATERIALS).

3.4. Hydrogen Embrittlement Susceptibility

The hydrogen embrittlement susceptibility of the X60 and X70 steel skelp materials was evaluated using uniaxial tensile testing of sub-sized cylindrical tensile samples with and without being subjected to a cathodic hydrogen charging pre-treatment step. Sub-size cylindrical tensile samples, as shown in Figure 3.7, were prepared from the ½ depth (centreline) location of the X60 and X70 steel skelps with the long axis parallel to the RD for this purpose. Tensile testing was conducted using a 10 kN tensile test frame using a strain rate of 1 mm/min. and a 12.5 mm extensometer under ambient laboratory conditions.

The data obtained from this procedure contains the elongation of the sample gauge section caused by the applied force (applied along the RD), which can then be used to plot a tensile curve of engineering stress versus engineering strain. This process was repeated in triplicate for each tensile sample of each steel grade. The equations for calculating engineering stress (Equation 3.5) and engineering strain (Equation 3.6) are as follows, where s is the engineering stress (MPa), F is the tensile force (N), A_o is the initial cross-sectional area of the tensile gauge (mm^2), e is the engineering strain, ΔL is the change in gauge length (mm), and L_o is the initial gauge length (mm) [43]:

$$s = \frac{F}{A_o} \quad 3.5$$

$$e = \frac{\Delta L}{L_o} = \frac{L - L_o}{L_o} \quad 3.6$$

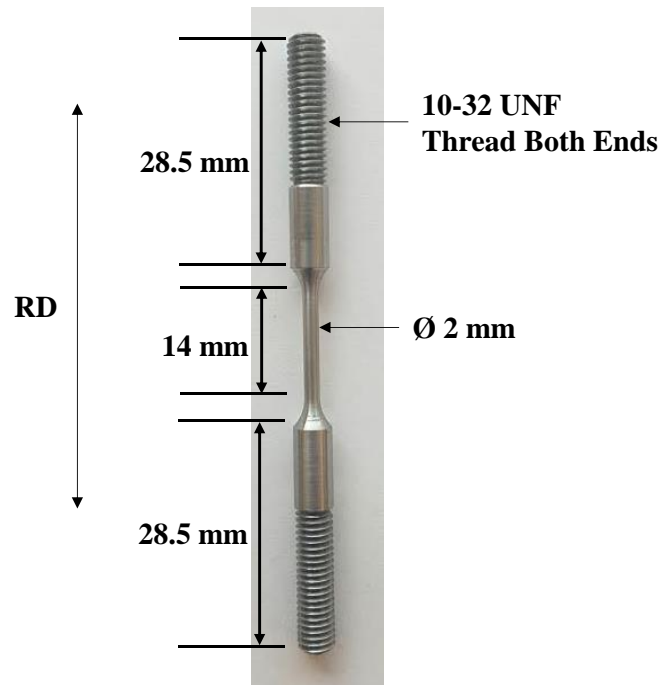


Figure 3.7: Sub-size cylindrical tensile samples used for tensile testing of X60 and X70 steel skelp material with and without hydrogen charging.

Hydrogen pre-charging was conducted by galvanostatically polarizing the cylindrical tensile samples at an applied cathodic current density of -10 mA/cm^2 for 24 h in a solution comprised of 30 g/L NaCl + 5 g/L NH_4SCN + 7.07 g/L H_3BO_3 + 8.27 g/L $\text{Na}_2\text{B}_4\text{O}_7 \cdot 10\text{H}_2\text{O}$ (pH ~ 8.1). This test solution is known to hydrogen embrittle X70 steel [49]. Hydrogen charging was done in a CorTest Proof Ring using an Agilent E3612A DC Power Supply to apply the galvanostatic cathodic polarization. A graphite rod was used as the counter electrode, and the solution was deaerated using nitrogen gas throughout the duration of the experiment. The tensile samples were charged while elastically stressed to 85% of the 0.2% offset tensile yield strength. The 0.2% offset tensile yield stress ($\text{YS}_{0.2\%}$) was determined from a triplicate set of uniaxial tensile testing of the X60 and X70 $\frac{1}{2}$ depth

(centreline) samples with the starting (as-rolled and un-charged) microstructure, Figure 3.8.

The $YS_{0.2\%}$ for the starting X60 and X70 $\frac{1}{2}$ depth (centreline) samples were determined to be 420 ± 6 MPa and 562 ± 10 MPa respectively. A photographic image of this set-up is shown in Figure 3.9.

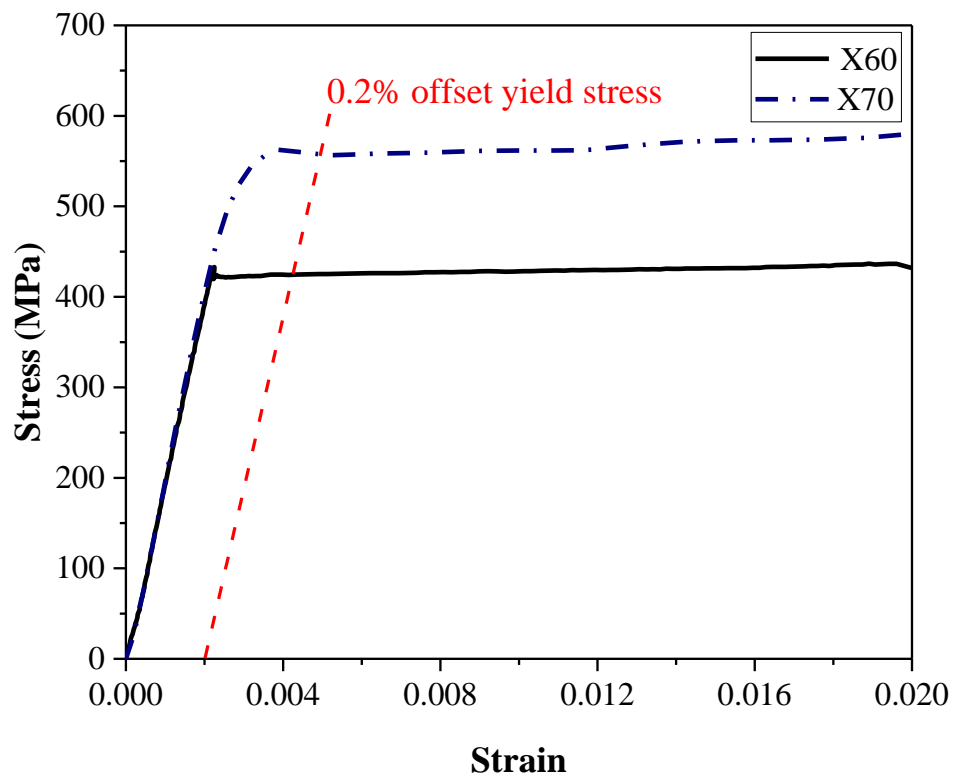


Figure 3.8: Engineering stress-strain plots for as-received X60 and X70 $\frac{1}{2}$ depth (centreline) samples to determine 0.2% offset yield stress ($YS_{0.2\%}$).

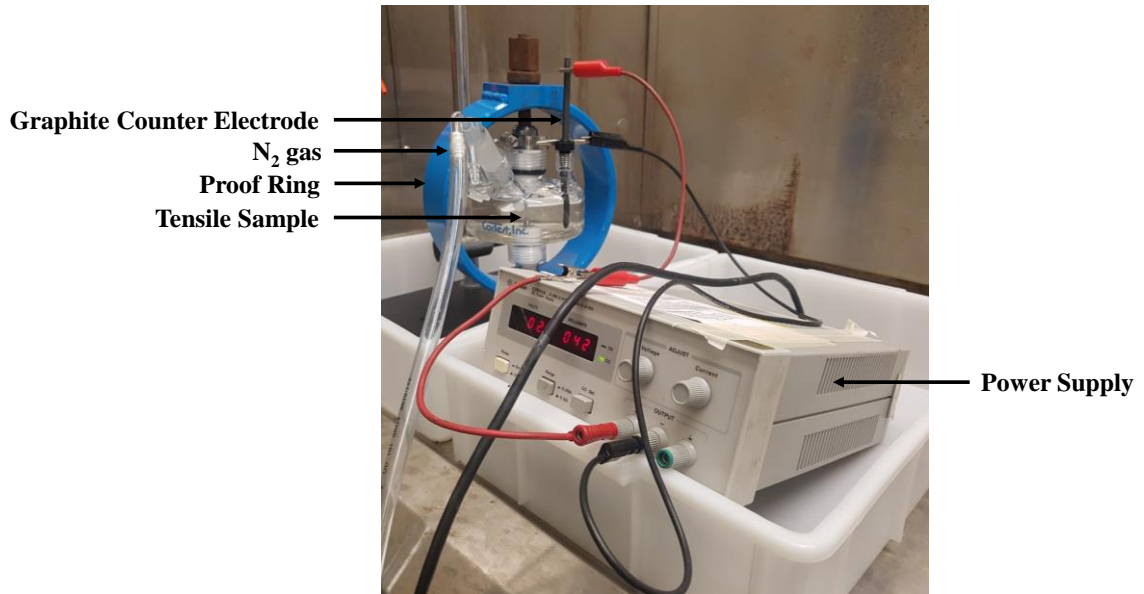


Figure 3.9: Experimental apparatus used to charge the tensile samples with hydrogen under a constant applied cathodic current density and a constant elastic loading (85% of $YS_{0.2\%}$).

To apply the static load elastic tensile load (85% of $YS_{0.2\%}$) to the tensile samples, it was necessary to apply a compressive load to the proof ring, which in turn provided a tensile load to the samples. To determine the ring deflection parameters it was necessary to first calculate the ring load (N), P , by multiplying the desired stress level (MPa), S , by the cross-sectional area (mm), A , of the tensile sample gauge section, Equations 3.7 and 3.8 [50]:

$$P = SA \quad 3.7$$

$$S = 0.85 \times YS_{0.2\%} \quad 3.8$$

Using the proof ring calibration curve, Figure 3.10, it was possible to determine the ring deflection (mm), d , required to obtain the desired load, P .

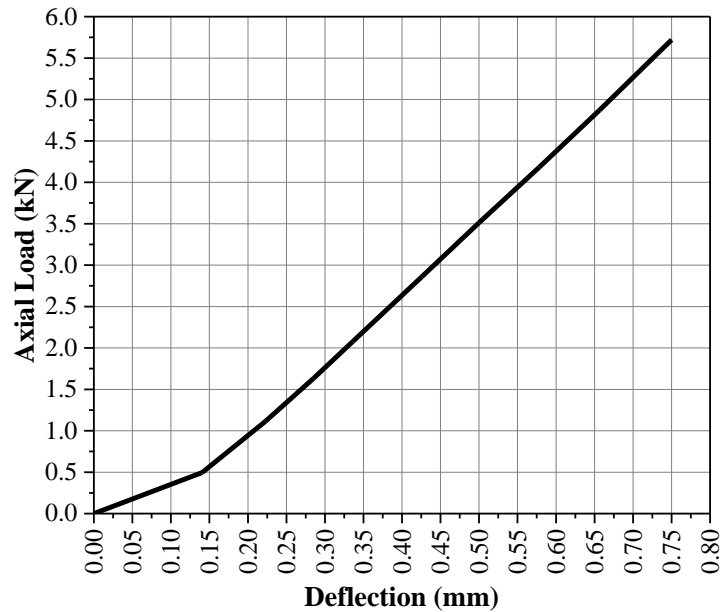


Figure 3.10: Proof ring calibration curve.

For sample loading in the CorTest[®] Proof Ring, the dial indicator was adjusted to read 0.000", and the adjusting nut tightened while the load adjusting screw was held stationary. The proof ring was then deflected the necessary amount, d , to obtain the desired load (P) using the dial indicator to monitor approximate deflection.

The hydrogen embrittlement susceptibility of the X60 and X70 steels was assessed by comparing the tensile properties before and after galvanostatic cathodic hydrogen charging. This was done using tensile properties of true stress and true strain to calculate the percent reduction in area ($\%RA$), Equation 3.9, and to compare the true strain at failure (ϵ_f) of the charged samples to the uncharged samples, where A_o is the original cross-sectional area of the sample (mm^2), and A_f is the cross-sectional area of the sample at the point of fracture (mm^2) [43].

$$\%RA = \frac{A_o - A_f}{A_o} \times 100 \quad 3.9$$

The fracture surfaces were imaged using a JEOL JSM-6610LV SEM. Images were acquired using an accelerating voltage of 10 kV and a working distance of 10 mm. The objective of the imaging was to compare differences in fracture mode between pre-charged and uncharged samples, as well as to look for physical evidence of inclusions serving as brittle crack initiation sites. The examination also made use of EDS to obtain elemental maps and point analysis of inclusions of interest found on the fracture surfaces using AZtec Version 3.3 Oxford Instruments software.

For the X70 steel samples, cross-sections of the fracture surfaces were also prepared and examined using SEM-EDS (JEOL JSM-6610LV SEM) to help determine the key microstructural features present that may have contributed to the rather significant hydrogen embrittlement observed during tensile testing. Cross-sections of the fracture surfaces were hot-mounted in phenolic polyfast resin, ground to 1200-grit finish using SiC paper and then polished up to 0.25 μm using water-free lubricants and diamond slurry. Prior to SEM-EDS analysis, samples were coated in a carbon film to prevent charging of the samples under the electron beam. Images were acquired using an accelerating voltage of 10 kV and a working distance of 10 mm.

Chapter 4: Results and Discussion

4.1. Starting Material Characterization

Light optical microscopy images of the starting (as-received) X60 and X70 steel skelp microstructures are shown in Figure 4.1(a-c) and Figure 4.1(d-f) for three orthogonal planes of the X60 and X70 steel respectively. The cross-section planes images (TD-ND and RD-ND planes) were taken at the centreline ($\frac{1}{2}$ depth) location. The X60 microstructure is consistent with a polygonal ferrite matrix, whereas the X70 microstructure is consistent with acicular ferrite matrix. There was no evidence of banded structures in either steel.

Chapter 4: Results and Discussion

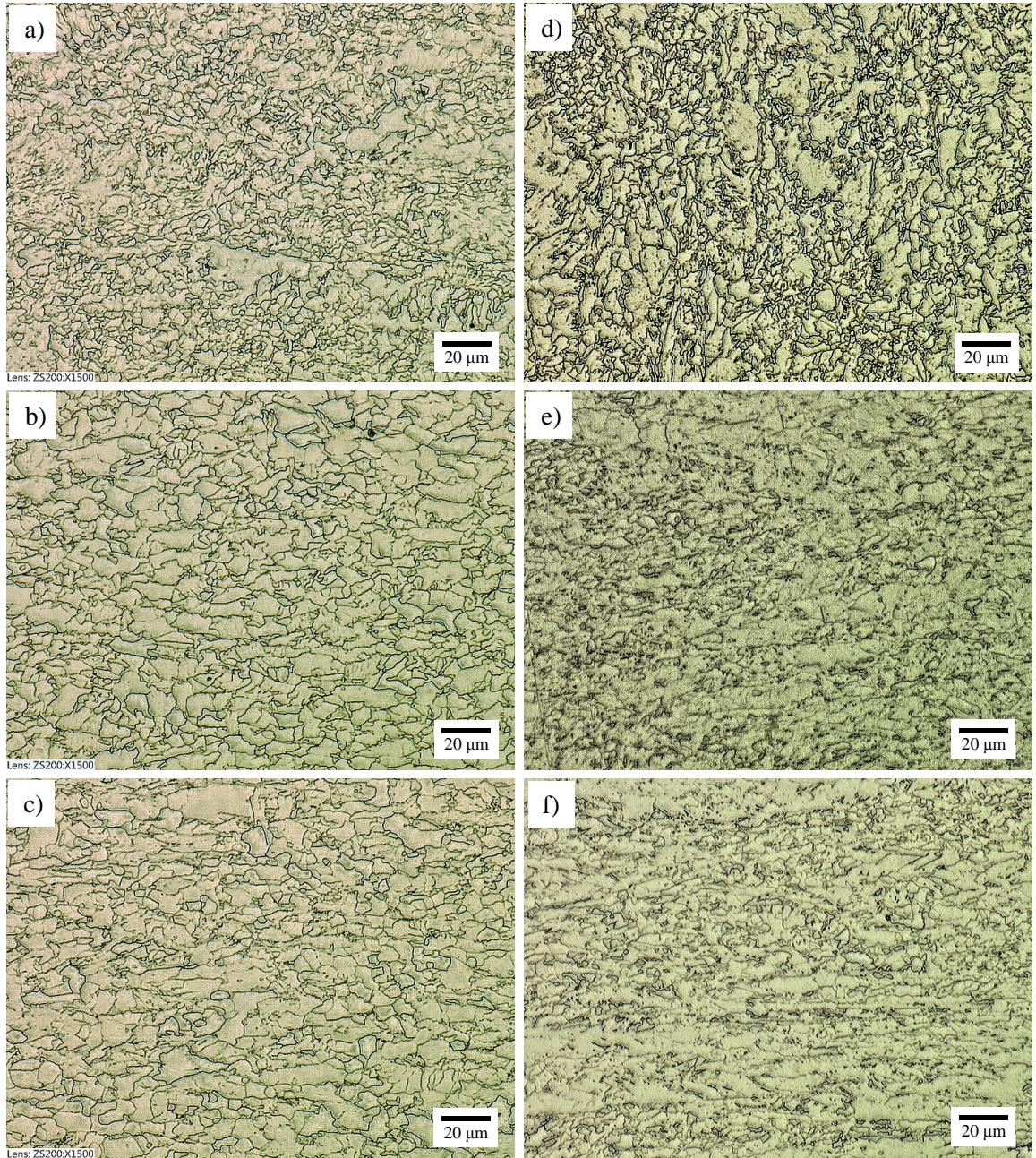


Figure 4.1: LOM images of the as-received centreline microstructures of the X60 steel (a) RD-TD, (b) TD-ND, and (c) RD-ND planes and the X70 steel (d) RD-TD, (e) TD-ND, and (f) RD-ND planes.

Figure 4.2(a-c) and Figure 4.2(d-e) compare the microstructure through the thickness of the RD-ND plane at the $\frac{1}{4}$, $\frac{1}{2}$, and $\frac{3}{4}$ depths of the X60 and X70 steel respectively. No significant variations in the appearance of the microstructure was observed for either steel upon comparing the three through-thickness images. Qualitatively speaking, the grain size of X60 steel is larger than that of X70 steel, and that the grain size in the centreline ($\frac{1}{2}$ depth) for both steels is larger than that at either of the two quarterline ($\frac{1}{4}$ and $\frac{3}{4}$) depths.

Chapter 4: Results and Discussion

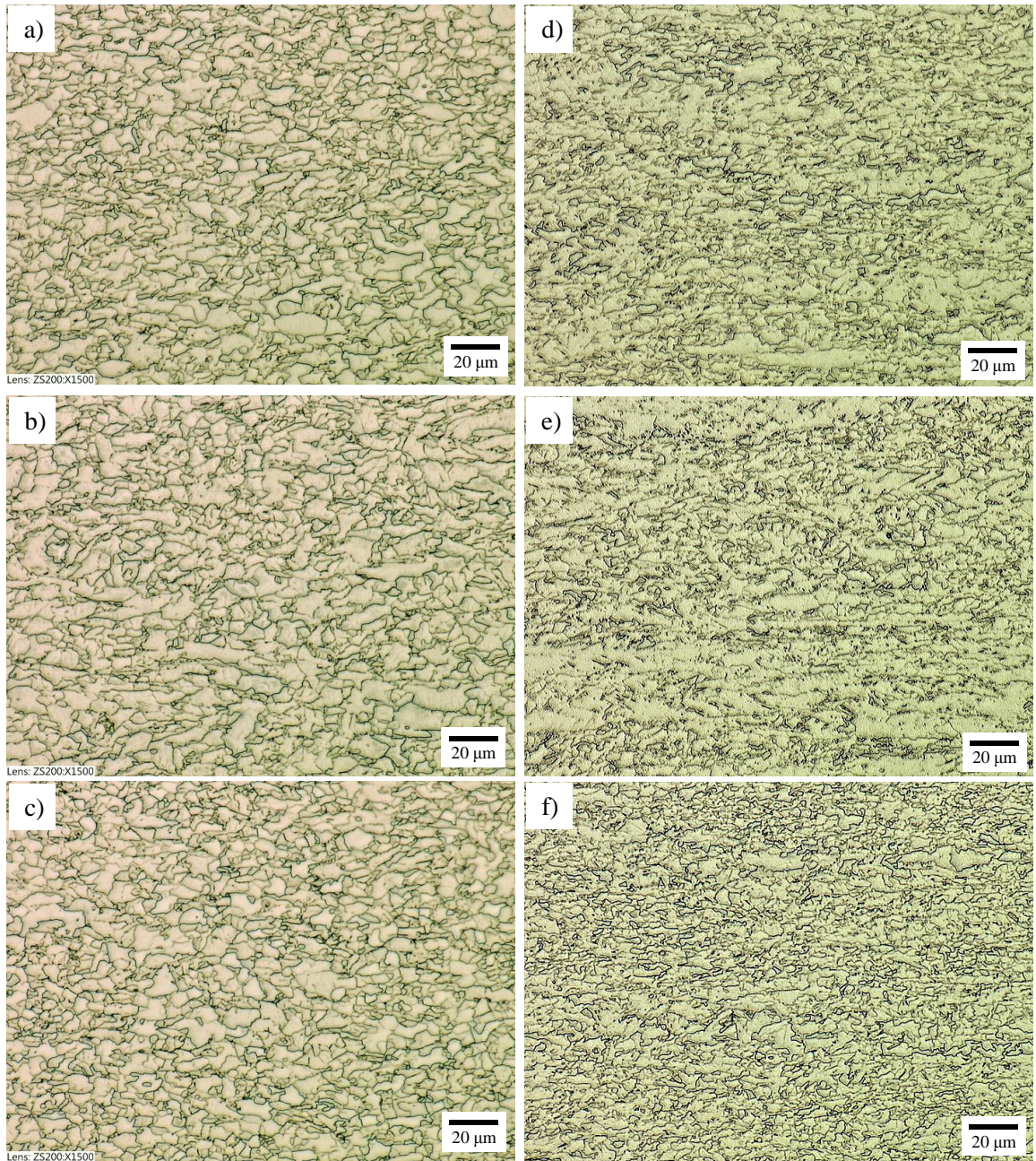


Figure 4.2: LOM images of the RD-ND plane of the X60 steel at the (a) $\frac{1}{4}$ depth, (b) $\frac{1}{2}$ depth, and (c) $\frac{3}{4}$ depth locations and of the X70 steel at the (d) $\frac{1}{4}$ depth, (e) $\frac{1}{2}$ depth, and (f) $\frac{3}{4}$ depth locations.

The average grain sizes for the X60 and X70 steel were calculated for the $\frac{1}{4}$, $\frac{1}{2}$, and $\frac{3}{4}$ depths of the RD-ND plane. This was done using the Heyn lineal intercept procedure, where five test lines were used to obtain an average grain size within 95% confidence for each depth [45]. Figure 4.3 shows SEM images obtained from the $\frac{1}{4}$, $\frac{1}{2}$, and $\frac{3}{4}$ depths of the RD-ND plane from X60 and X70 grades of steel respectively that were used for grain size measurements. The mean grain diameters of the $\frac{1}{4}$ depth, $\frac{1}{2}$ depth, and $\frac{3}{4}$ depth of the X60 steel were determined to be $6.5 \pm 0.4 \mu\text{m}$, $9.0 \pm 0.5 \mu\text{m}$, and $7.5 \pm 0.2 \mu\text{m}$ respectively. The mean grain diameters of the $\frac{1}{4}$ depth, $\frac{1}{2}$ depth, and $\frac{3}{4}$ depth of the X70 steel were determined to be $5.5 \pm 0.3 \mu\text{m}$, $6.8 \pm 0.6 \mu\text{m}$, and $6.0 \pm 0.3 \mu\text{m}$ respectively.

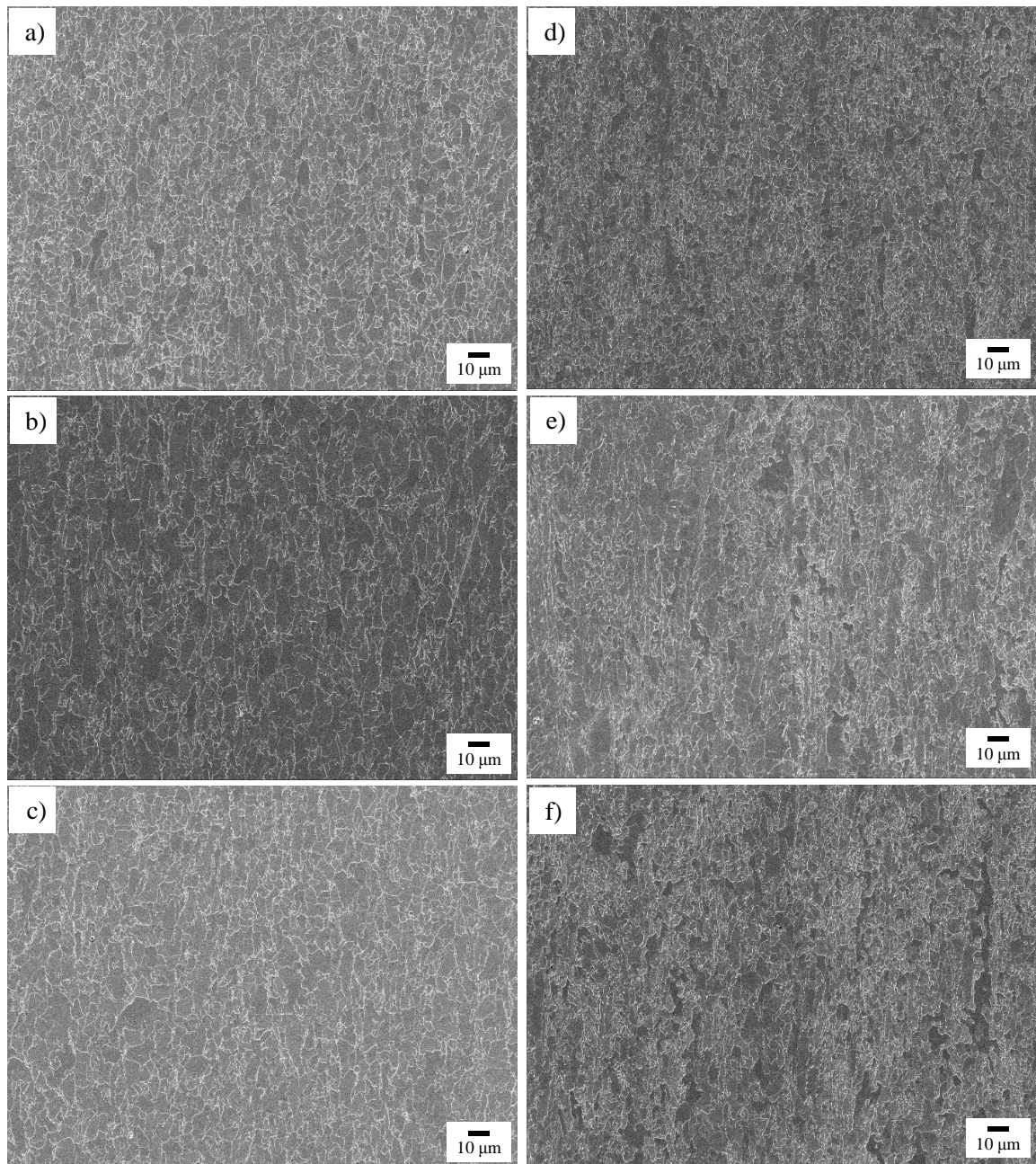


Figure 4.3: SEM images of the RD-ND plane of the X60 steel at the (a) $\frac{1}{4}$ depth, (b) $\frac{1}{2}$ depth, and (c) $\frac{3}{4}$ depths and of the X70 steel (d) $\frac{1}{4}$ depth, (e) $\frac{1}{2}$ depth, and (f) $\frac{3}{4}$ depth locations.

It has been reported in the literature that variations in the grain size and the type of matrix phases present in the microstructure have an effect on the HIC susceptibility of the steel [10], [11], [25]–[27]. It was determined that the centreline ($\frac{1}{2}$ depth) location of both steels contained a larger grain size than the quarterline ($\frac{1}{4}$ and $\frac{3}{4}$ depth) locations. The cause of this grain size difference between the centrelines and quarterlines is due to the cooling stage after hot rolling. It is difficult to achieve uniform grain size through the plate thickness as the surfaces of the plate has a faster heat extraction than the centre of the plate, resulting in the centre remaining at higher temperatures for longer times ultimately causing grain coarsening [32]. The grain size in the X60 steel is larger than that in the X70 steel. This difference is typical between the two steels, and is likely due to the increase in the Nb and Ti micro-alloying content in the X70 steel [26], [37]. It has been reported that grain refinement decreases HIC susceptibility, which offers an explanation as to why the centreline of the steels are typically more susceptible to HIC. However this does not explain why X70 is more susceptible to HIC than X60 steel skelp as X70 typically has a smaller grain size [10], [29].

Chapter 4: Results and Discussion

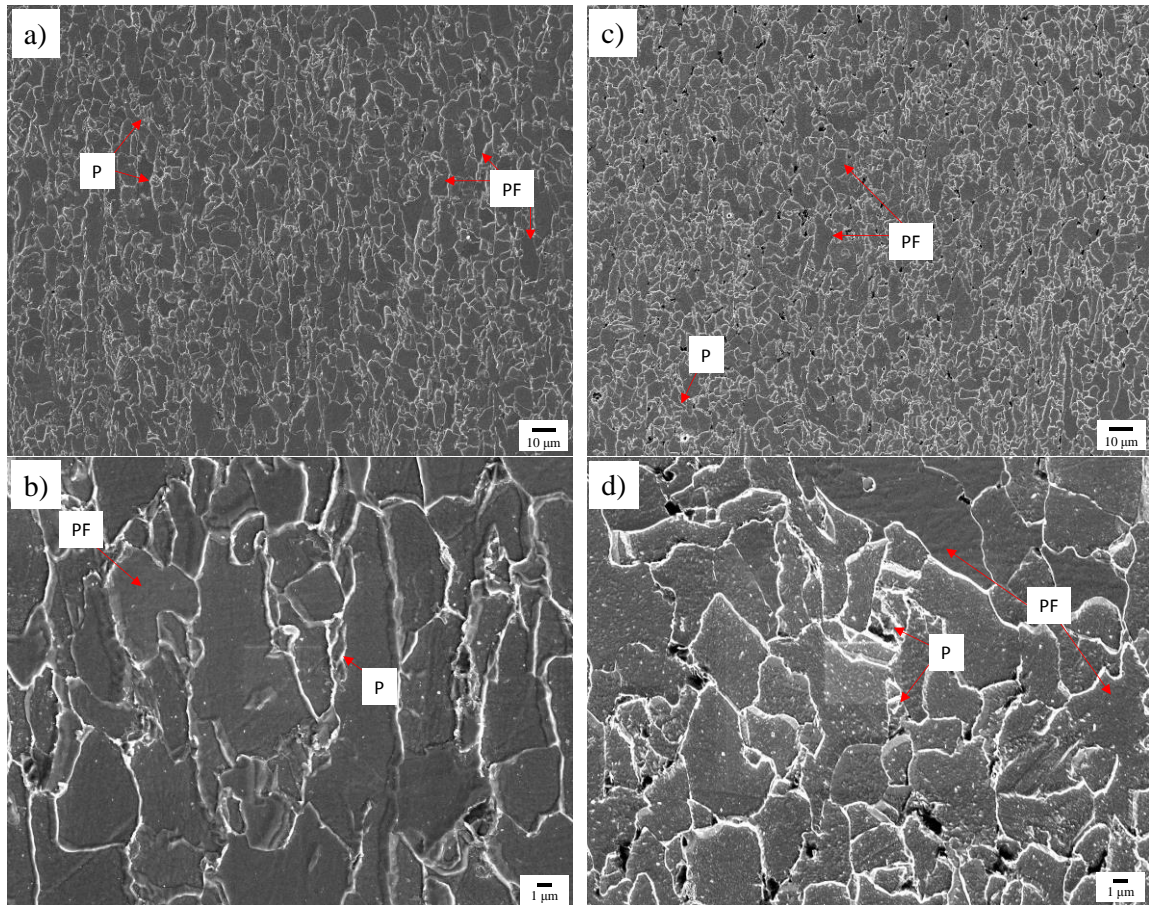


Figure 4.4: SEM images of $\frac{1}{2}$ depth from X60 steel skelp from the RD-ND plane, (a) and (b), and the TD-ND plane, (c) and (d). Polygonal ferrite (PF) and pearlite (P) phases are indicated.

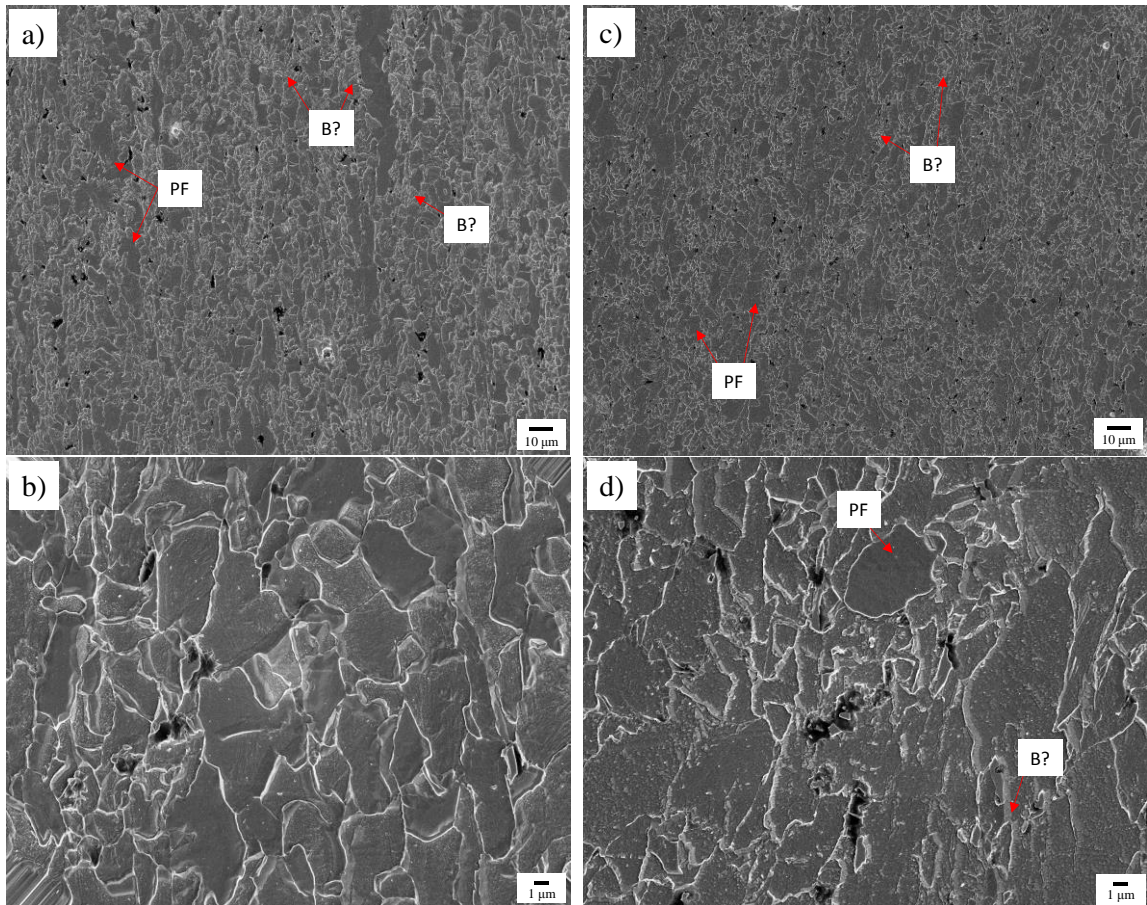


Figure 4.5: SEM images of $\frac{1}{2}$ depth from X70 steel skelp from the RD-ND plane, (a) and (b), and the TD-ND plane, (c) and (d). Polygonal ferrite (PF) and bainite (B) phases are indicated.

The difference in HIC susceptibility between X60 and X70 steel could be caused by the different phases present in the microstructures, where it has been reported that X60 can contain acicular ferrite, polygonal ferrite and pearlite, whereas X70 can contain acicular ferrite, polygonal ferrite, pearlite, bainite and small particles of martensite within its microstructure [10], [11], [26], [29], [33], [51], as revealed by SEM imaging and associated analysis techniques. From SEM analysis in Figure 4.4 and Figure 4.5 respectively, there

appears to be ferrite and pearlite present in the X60 steel skelp microstructure, and ferrite, pearlite and potential bainite present in the X70 steel skelp microstructure. Xiao et al. reported that acicular ferrite is beneficial due to its increasing tensile strength, resulting in good toughness, and increasing corrosion resistance [33], [51]. It is known that hard matrix phases have relatively high HIC susceptibility. Ferrite phases are relatively soft and bainite is harder than pearlite, therefore the efficiency of hydrogen trapping tends to increase in the following order: ferrite < pearlite < bainite [10], [12], [28]. Moon et al. has also reported that phases having increased hardness tend to segregate to the centreline of the steel plate during the hot rolling process [12]. From the SEM methods used in this study it was not possible to qualify centreline segregation of hard phases in the steel grades being investigated, therefore a detailed EBSD study would be necessary to confirm hard phase segregation in either the X60 or X70 grade steel, or both.

Work done by Moon et al., focused on the role of Ca addition in affecting HIC susceptibility in API pipeline steel [12]. Figure 4.6 reproduces their findings on the HIC susceptibility as it relates to an increasing Ca/S ratio in the steel through Ca additions. From the chemical compositions of the X60 and X70 steel, Table 3.1, it was determined that the Ca/S ratio in the X60 steel is 4.3 and in the X70 steel is 0.3. Superimposing the Ca/S ratios of the X60 and X70 steel on Figure 4.6 reveals that the Ca/S ratio in the X60 steel falls within the range of low HIC susceptibility (where no cracking was observed), whereas the Ca/S ratio in the X70 steel is within the range of high HIC susceptibility (where cracking was observed). The study done by Moon et al. reveals that cracking did not occur in pipeline steels with a Ca/S ratio higher than 1.28 [12]. Ca treatment is used to prohibit the formation

of problematic MnS inclusions by promoting the formation of CaS inclusions instead, as well as for its control of oxide inclusion shape, quantity, and distribution [13]. However, treating the steel with Ca does not guarantee that the formation of problematic MnS inclusions does not occur. Moon et al. state that when the Ca/S ratio was higher than 1.25 MnS inclusions were not formed and rather CaS inclusions formed instead. This agrees with work done by Yin et al. which suggests a Ca/S ratio between 2~5 prevents the formation of problematic MnS inclusions [12], [15].

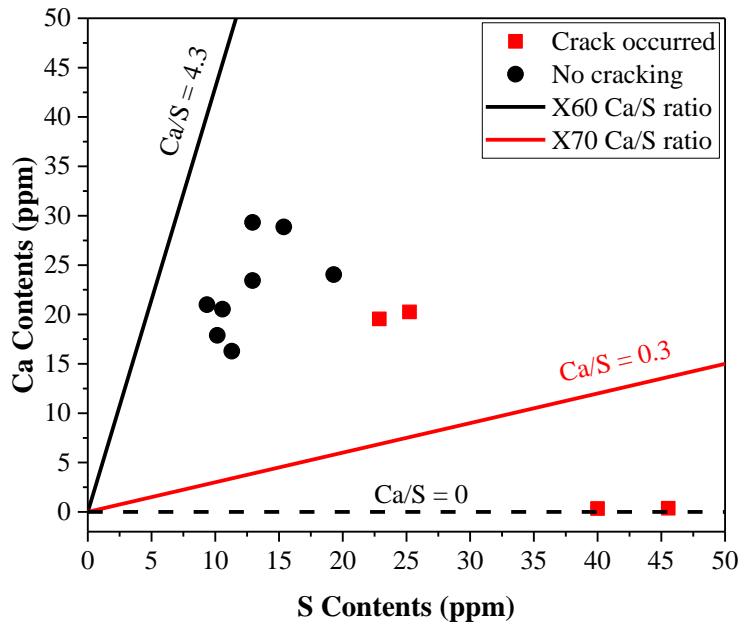


Figure 4.6: Effect of Ca/S ratio on the HIC susceptibility of steel [12].

Table 4.1 and Table 4.2 summarize the results of the ASPEX[®] inclusion analyses listing the count, average diameter and area fraction of the major inclusion types detected in the RD-ND and TD-ND planes of the X60 and X70 steel. One significant observation

extracted from the two tables is that the average diameter of the major inclusions types shows little variation in average size ranging from 1.7 μm to 7.7 μm regardless of cross-sectional plane or the steel. Another significant observation is that there is also little variation in the type, count, average diameter and area fraction of the major inclusions through-thickness of either steel.

Table 4.1: Count, average diameter and area fraction of inclusions as determined through ASPEX[®] analysis for the RD-ND plane and TD-ND planes of the X60 steel.

Inclusion Type	¼ Depth						½ Depth						¾ Depth						
	Count		Average Diameter (µm)		Area Fraction (× 10 ⁶)		Count		Average Diameter (µm)		Area Fraction (× 10 ⁶)		Count		Average Diameter (µm)		Area Fraction (× 10 ⁶)		
	RD ND	TD ND	RD ND	TD ND	RD ND	TD ND	RD ND	TD ND	RD ND	TD ND	RD ND	TD ND	RD ND	TD ND	RD ND	TD ND	RD ND	TD ND	
Al Si	0	1	0	3.9	0	0.5	0	0	0	0	0	0	0	1	0	2.5	0	0.1	0
Alumina	10	4	4.8	1.8	0.9	0.4	10	0	7.3	0	1.5	0	8	1	2.1	2.9	0.6	0.2	
CaO-Al ₂ O ₃	100	61	7.4	5.6	23.9	12.6	130	62	6.5	7.4	12.7	18.3	123	82	8.4	5.2	20.7	21.3	
Ca-Si-Al	3	2	2.3	3.6	0.4	0.9	0	1	0	8.4	0	2.2	3	2	2.4	3.7	0.4	0.9	
CaS Type I	177	136	2.3	3.2	30.8	53.8	251	185	2.5	2.8	43.7	45.9	243	195	2.6	2.8	46.1	57.1	
CaS-MnS	2	3	2.9	2.6	0.4	0.7	2	5	3.2	2.7	0.5	1.0	4	1	3.0	2.7	1.0	0.2	
CaS Type II	69	56	2.7	3.2	15.3	20.4	81	61	2.7	2.7	16.3	14.9	81	61	2.9	2.8	15.4	14.8	
CaSi	1	1	2.5	2.2	0.1	0.1	1	0	2.4	0	0.1	0	0	1	0	5.9	0	1.0	
Mg	2	1	3.0	2.1	0.5	0.1	3	1	2.7	1.8	0.6	0.1	1	2	1.9	2.4	0.1	0.3	
MgO	44	21	2.2	2.8	8.0	6.9	57	21	2.0	2.6	4.7	5.0	47	31	2.8	2.7	13.3	8.2	
Ti	123	50	1.7	1.9	7.3	5.7	93	67	1.7	1.8	5.8	6.1	120	81	1.8	1.8	7.6	8.2	
TiAl	2	0	1.7	0	0.2	0	1	0	3.4	0	0.2	0	0	0	0	0	0	0	
TiAlCa	37	13	1.8	2.3	3.0	2.1	44	20	1.8	1.8	3.1	2.1	51	28	2.1	2.1	5.2	3.9	
TiCa	92	72	2.0	2.3	9.6	13.3	123	81	2.0	2.3	10.5	13.4	120	87	1.9	2.2	9.8	12.6	
TiS	180	104	1.9	2.1	14.1	15.6	185	102	2.1	2.0	15.1	12.4	210	128	2.0	2.0	15.6	14.3	
TiS-MnS	0	4	0	2.5	0	0.8	8	7	2.3	2.2	1.1	0.9	7	3	2.0	2.3	0.6	0.5	

Table 4.2: Count, average diameter and area fraction of inclusions as determined through ASPEX[®] analysis for the RD-ND plane and TD-ND planes of the X70 steel.

Inclusion Type	¼ Depth						½ Depth						¾ Depth					
	Count		Average Diameter (µm)		Area Fraction (× 10 ⁶)		Count		Average Diameter (µm)		Area Fraction (× 10 ⁶)		Count		Average Diameter (µm)		Area Fraction (× 10 ⁶)	
	RD ND	TD ND	RD ND	TD ND	RD ND	TD ND	RD ND	TD ND	RD ND	TD ND	RD ND	TD ND	RD ND	TD ND	RD ND	TD ND	RD ND	TD ND
AlMnS	0	1	0	1.7	0	0.04	1	1	2.4	1.8	0.1	0.04	1	1	3.8	1.8	0.2	0.1
Alumina	3	2	4.2	3.6	0.8	0.4	5	8	5.5	4.3	2.2	2.4	6	1	2.3	2.3	0.4	0.1
CaO-Al ₂ O ₃	172	164	5.8	7.7	91.8	128.1	180	181	5.1	9.3	106.4	129.1	199	154	7.2	6.7	153.3	116.5
Ca-Si-Al	4	14	3.0	3.8	0.5	3.1	3	6	4.0	3.7	0.8	1.2	7	5	3.5	2.7	1.3	0.5
CaS Type I	11	11	3.1	3.5	2.1	2.3	10	7	3.2	2.4	2.0	0.7	15	4	3.7	2.2	4.1	0.3
CaS-MnS	26	31	2.5	2.5	2.5	3.8	30	24	2.7	2.1	3.5	1.7	36	22	3.0	2.6	5.2	2.5
CaS Type II	124	135	4.5	4.2	43.8	46.5	139	129	4.4	4.5	44.9	50.5	164	123	4.5	4.3	55.9	4.1
CaSi	10	12	6.3	3.8	19.9	2.6	7	15	3.4	3.9	1.2	3.3	24	13	3.5	3.6	4.2	2.6
MgO	1	2	3.2	4.2	0.1	0.5	1	0	2.5	0	0.1	0	0	2	0	2.9	0	0.3
MnSi	1	2	3.2	3.2	0.1	0.3	0	0	0	0	0	0	2	2	3.8	3.0	0.4	0.2
MnS	278	237	3.0	2.8	40.1	33.7	241	251	3.0	2.5	34.8	29.1	289	236	3.2	2.4	44.2	26.1
Spinel	40	40	3.7	2.4	14.2	8.2	53	51	3.6	2.6	11.8	8.7	39	31	4.8	3.0	8.9	5.4
TiAl	11	8	2.4	2.6	1.0	1.0	9	9	2.5	1.6	0.86	0.4	7	9	2.5	1.8	0.7	0.5
TiAlCa	11	6	3.4	2.0	2.2	0.4	5	1	2.5	1.3	0.5	0.03	11	4	3.0	3.4	1.7	0.7
TiAlMg	2	1	2.6	1.9	0.2	0.05	2	1	3.4	1.8	0.3	0.04	0	1	0	2.0	0	0.05
TiCa	2	2	4.0	3.1	0.4	0.3	4	1	2.9	1.3	0.6	0.02	3	0	1.9	0	0.2	0
TiS-MnS	0	1	0	2.9	0	0.1	0	0	0	0	0	0	1	0	1.8	0	0.04	0

The area fraction data (which is a function of both the count and the average diameter) of the major inclusions types is plotted as bar charts in Figure 4.7 and Figure 4.8 for the X60 and X70 steel respectively. For the X60 steel, large amounts of Ca-containing inclusions were detected; such as CaS, CaSi, CaSiAl compounds, CaS MnS compounds, and CaO-Al₂O₃. Furthermore, many Ti-containing inclusions were detected, such as Ti, TiAlCa compounds, TiCa, TiS, TiS MnS compounds, and TiAl. Similarly for the X70 steel, large amounts of Ca-containing inclusions were detected; including CaS, CaSi, CaSiAl compounds, CaS MnS compounds, and CaO-Al₂O₃. However, while Ti-containing inclusions were detected in the X70 steel; including TiAl, TiAlCa, TiAlMg, TiCa, TiS, and TiS MnS compounds, there were significantly fewer of these inclusions than those detected in the X60 steel. Spinel inclusions were detected in the X70 steel but not detected in the X60 steel. Area fractions of Ca-containing inclusions in X70 steel were 3x higher than those detected in the X60 steel. Area fractions of MnS inclusions in the X70 steel were similar with the area fractions of Ca-containing inclusions detected in the X60 steel. MnS inclusions are detected in the X70 steel skelp due to low Ca content and high S content in X70 chemical composition.

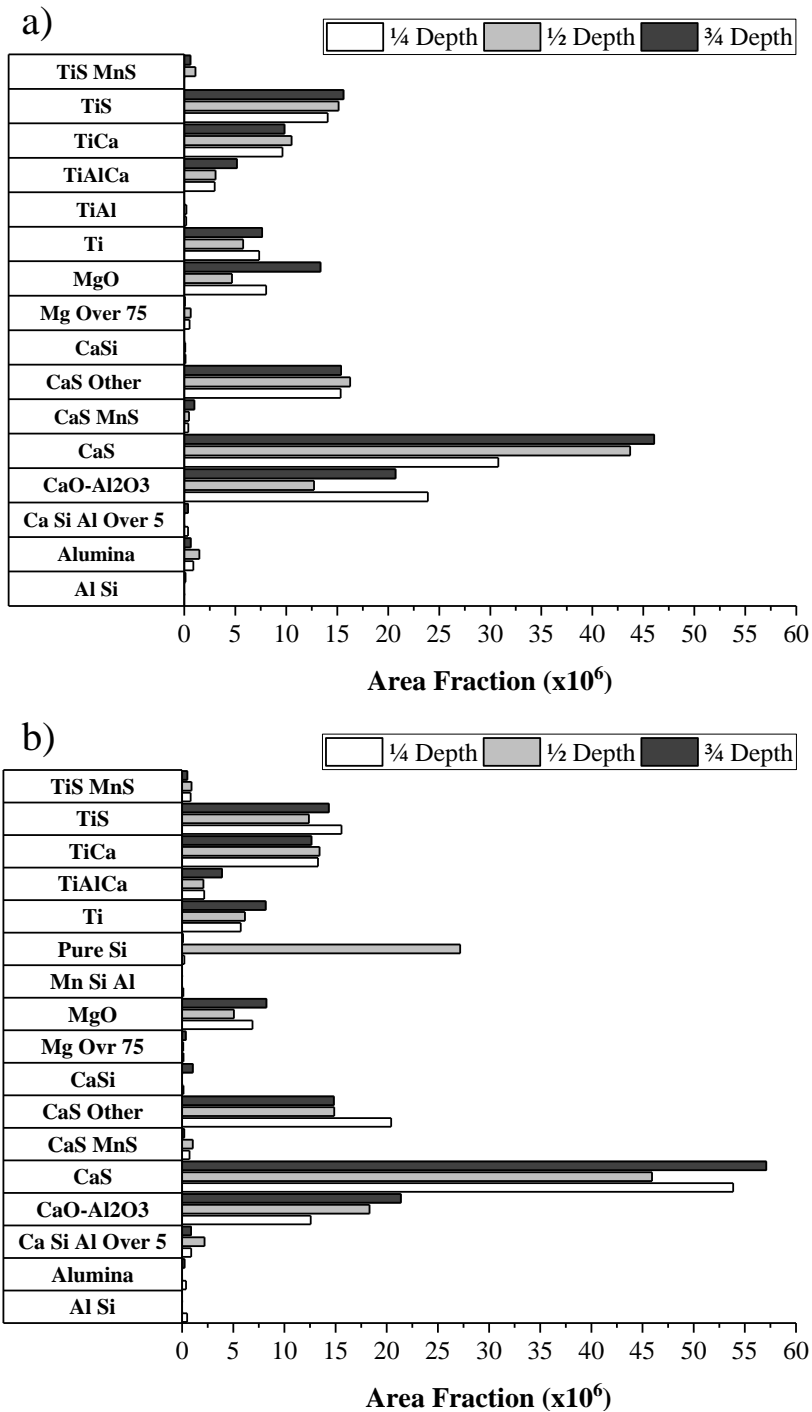


Figure 4.7: Area fraction plots of inclusions as determined through ASPEX[®] analysis for the X60 steel: (a) RD-ND plane and (b) TD-ND plane.

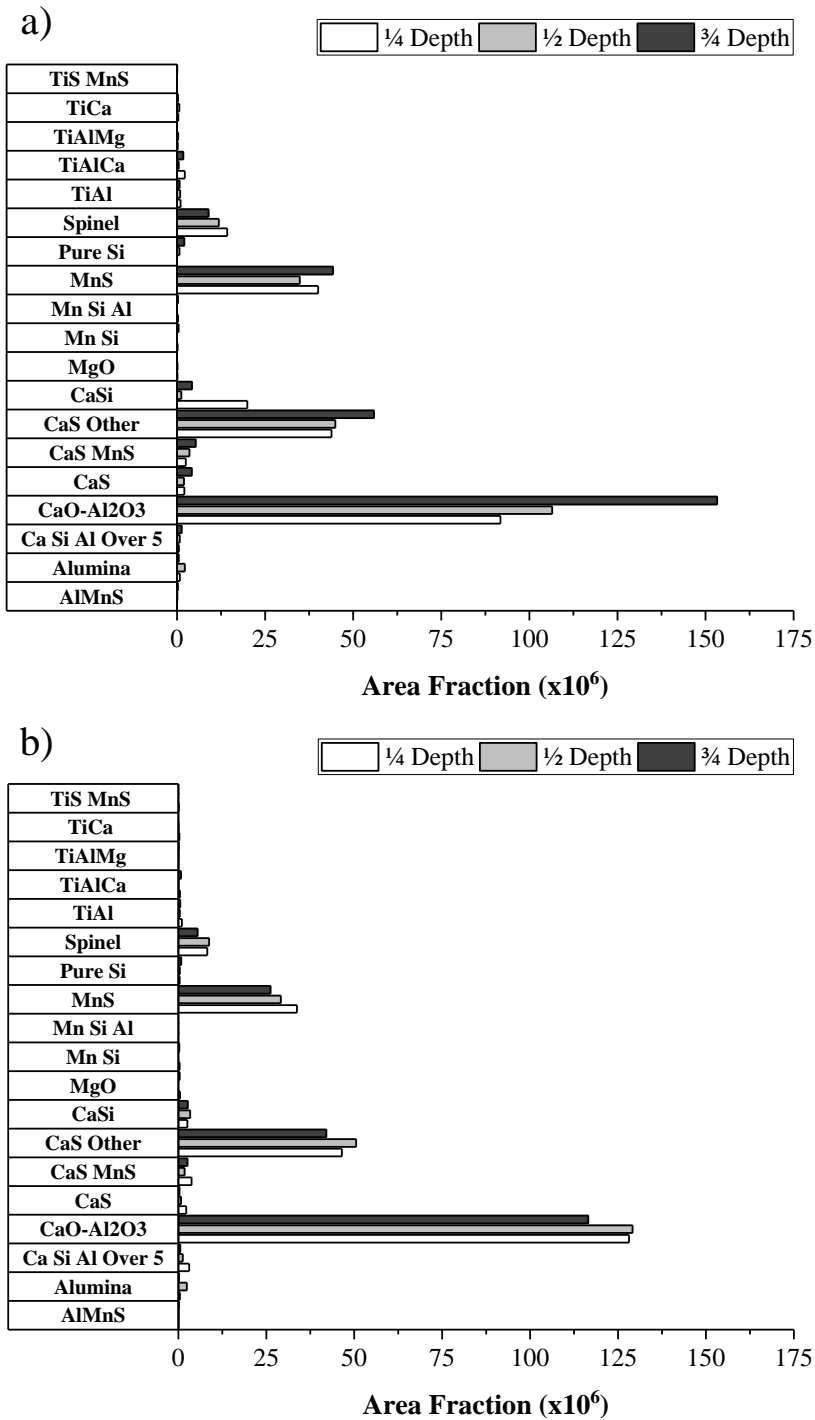


Figure 4.8: Area fraction plots of inclusions as determined through ASPEX[®] analysis for the X70 steel: (a) RD-ND plane and (b) TD-ND plane.

Individual inclusions were imaged in the X60 and X70 steel using SEM-EDS techniques and are shown in Figure 4.9 through Figure 4.13. Figure 4.9 shows a spherical inclusion imaged from the centreline of the X60 steel skelp. EDS mapping of this inclusion (Figure 4.9(b)) reveals the inclusion to be enriched in Mg oxides, CaS, CaO, but to not contain any elemental Mn or Al. The EDS map for Al is not shown as there was no detection of elemental Al in the inclusion nor the matrix. It is also interesting to note a prismatic Ti-nitride skin completely surrounding the inclusion. Figure 4.10 shows another inclusion type imaged from the centreline of the X60 steel skelp, but this inclusion is elongated rather than spherical in shape. In this inclusion, EDS mapping (Figure 4.10(b)) reveals the inclusion to comprise of CaS, Ca-Al-oxide, Mg oxide, and negligible amounts of Mn which is likely to be traces detected from the surrounding steel matrix. Ti-nitrides are still present along the edges of this inclusion, albeit in a non-prismatic shape and not encompassing the inclusion entirely. An inclusion imaged from the $\frac{1}{4}$ depth of the X70 steel skelp is shown in Figure 4.11. This inclusion is observed to be spherical in shape, and EDS mapping (Figure 4.11 (b)) reveals this inclusion to contain Al oxide, MnS, CaS, and a thin Ti-nitride skin partially surrounding the edge of the inclusion. EDS analysis did not detect Mg within this inclusion. Figure 4.12 is an image of a slightly irregular spherically shaped inclusion detected from the centreline of the X70 steel skelp. Figure 4.12(b) shows the EDS elemental maps indicating that this inclusion is enriched in Al oxide, Mg oxide, CaS, MnS, and small amounts of Ti partially surrounding the edge of the inclusion. The EDS map for N is not shown because no elemental N was detected through EDS in the inclusion nor surrounding matrix. Another inclusion detected from the centreline of the X70 steel skelp is imaged in

Figure 4.13. This inclusion is spherical in shape and EDS elemental mapping reveals that this inclusion contains Mg oxide, Al oxide, CaS, small traces of MnS was detected, as well as CaO. Very little Ti was detected at the inclusion edge, where it is seen to be along only a portion of the inclusion edge. An obvious difference detected through SEM-EDS spot check mapping between the X60 and X70 inclusions is the presence of Mn, which was detected in the inclusions found within the X70 steel, but not detected in those within the X60 steel. Otherwise, CaS, various oxides, and Ti-containing compounds were detected in inclusions contained in both steels. A main observation made is that Ti-N-compound in inclusions detected in the X60 steel are seen to form on the perimeter of Ca-Mg-O-S inclusions and sometimes the perimeter formation completely encompasses the core, forming a skin around the inclusion. While Ti-N-compounds were observed to be forming at the perimeter of inclusions detected in the X70 steel, it was not as developed as those observed on the X60 steel inclusions.

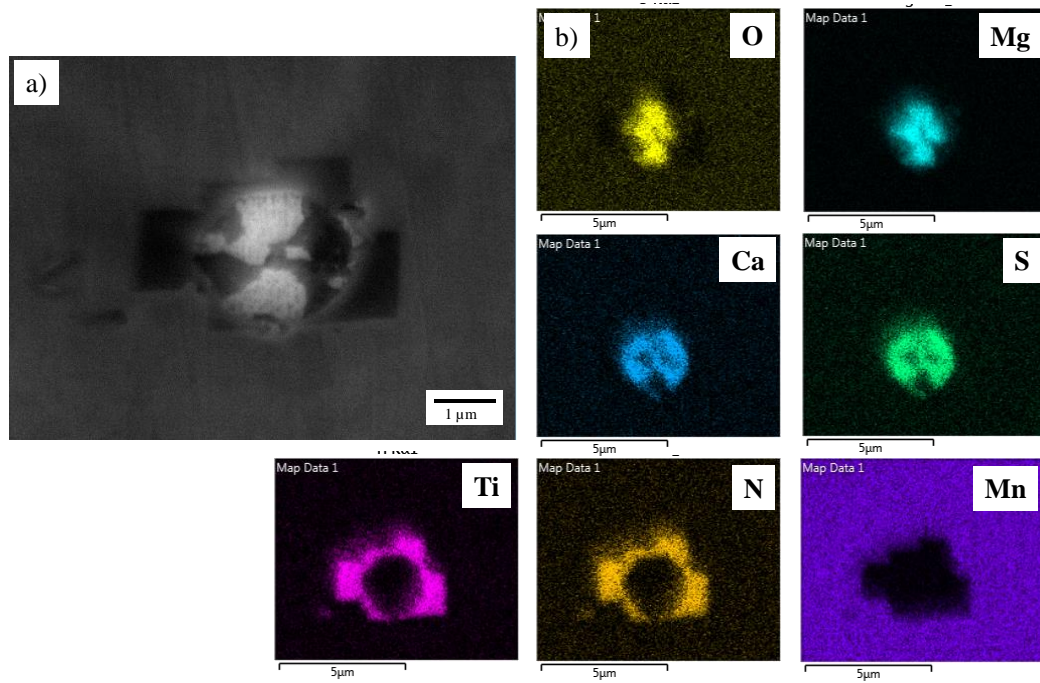


Figure 4.9: SEM image (a) and associated EDS maps (b) of a randomly selected inclusion in the $\frac{1}{2}$ depth of the X60 steel.

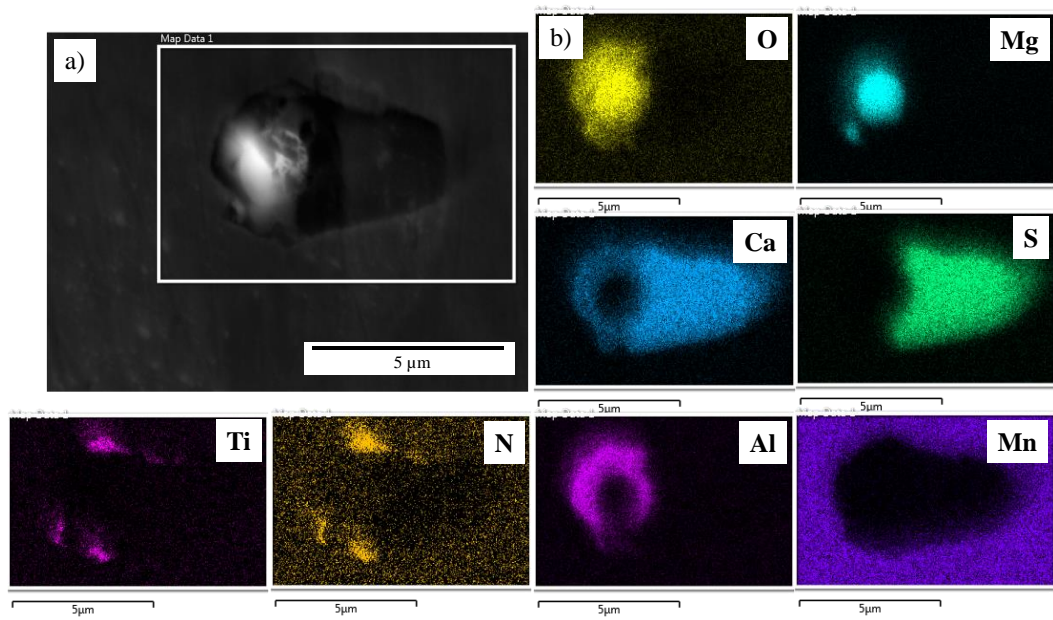


Figure 4.10: SEM image (a) and associated EDS maps (b) of a second randomly selected inclusion in the $\frac{1}{2}$ depth of the X60 steel.

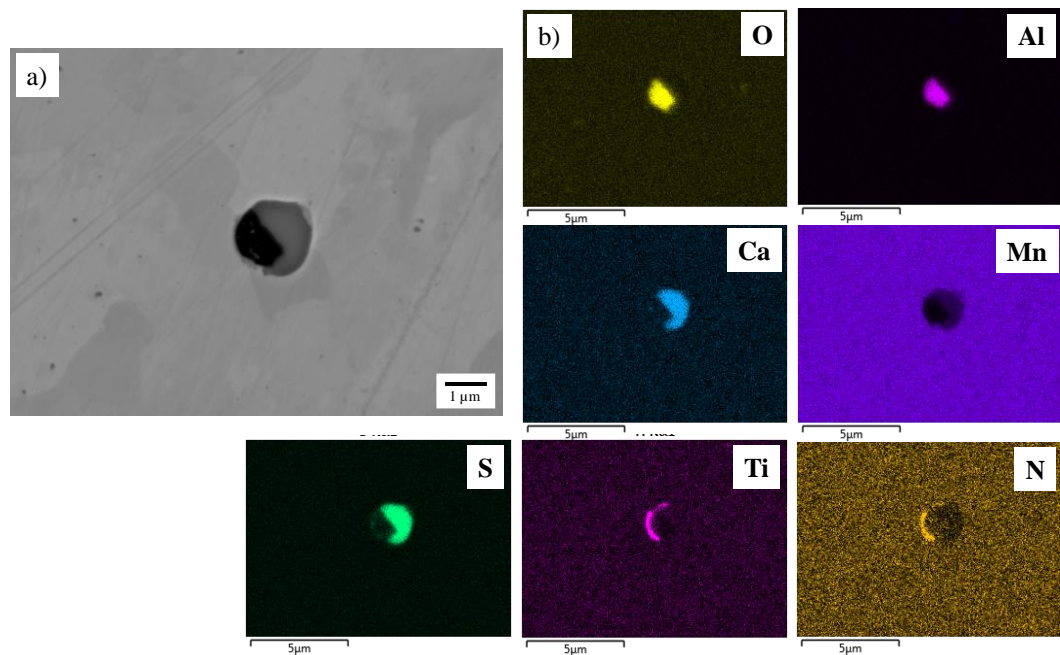


Figure 4.11: SEM image (a) and associated EDS maps (b) of a randomly selected inclusion in the $\frac{1}{4}$ depth of the X70 steel.

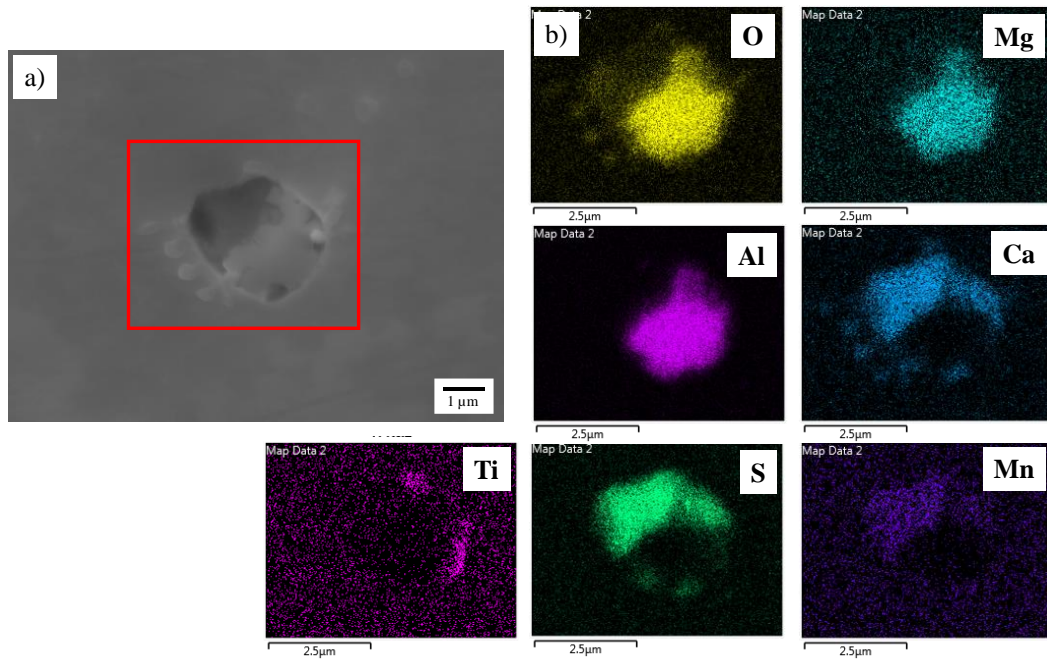


Figure 4.12: SEM image (a) and associated EDS (b) maps of a second randomly selected inclusion in the $\frac{1}{2}$ depth of the X70 steel.

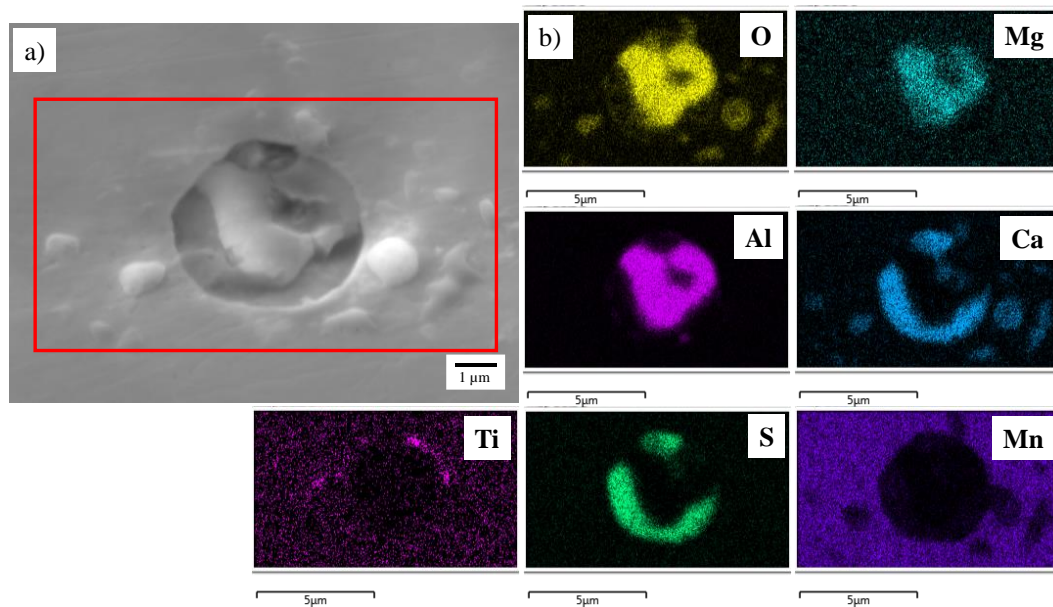


Figure 4.13: SEM image (a) and associated EDS maps (b) of a third randomly selected inclusion in the $\frac{1}{2}$ depth of the X70 steel.

Figure 4.14, Figure 4.15 and Figure 4.16 show a summary of the ASPEX[®] results from Figure 4.7 and Figure 4.8, binning together the area fraction, count and average diameter, respectively, of the inclusions containing specific elements; Ca, Mg, Al, Mn, Ti. From these results, it is clear that the X60 contains fewer Mn-containing inclusions than the X70, which is likely due to its higher Ca/S ratio. Overall, the area fraction of inclusions detected in the X70 steel was larger than that detected in X60 with the exception of Ti-containing inclusions, which had a larger area fraction within the X60 steel. Differences in both the area fraction and perimeter coverage of Ti-containing inclusions in the two steels is an intriguing finding. Dong et al. have concluded that Ti-containing inclusions in X60 steel do not have a significantly effect on HIC susceptibility [30]. The presence of Ti-containing inclusions was consistent in the $\frac{1}{4}$, $\frac{1}{2}$ and $\frac{3}{4}$ depths of both cross-sectional planes analyzed in both steels. A comparison of the inclusion count shows that there were overall fewer Ca-containing inclusions detected in the X70 steel with the exception of the $\frac{1}{4}$ depth analyzed in the TD-ND plane. There was not a significant difference in the Mg-containing inclusions between the two steels, but there were generally more Mg-containing inclusions within the X70 steel. It should be noted, however, that these Mg-containing inclusions also accounted for the spinel inclusion types detected in the X70 steel, while no spinel was detected in the X60. There were more Al-containing and Mn-containing inclusions, and significantly fewer Ti-containing inclusions detected in the X70 steel. The average diameter of inclusion types detected in X70 steel were larger than those detected in the X60 steel, with the exception of Al-containing and Ti-containing inclusions being smaller in the $\frac{1}{2}$ depth analyzed in the TD-ND plane, and Mn-containing inclusions being

smaller in the RD-ND plane and TD-ND plane of the $\frac{1}{2}$ depth only. It is important to consider the amount, size and area fractions of inclusions in the steel as an increase in these quantities make the steel more susceptible to HIC [12]. Huang et al. worked with high strength linepipe steel, namely X100 and X120, and emphasized that irreversible hydrogen trapping efficiency in steel increases with the amount and area of inclusions [25]. The types of inclusions detected in Huang et al.'s work primarily included Al_2O_3 and MnS , with small amounts of Fe-Mn-S complex inclusions and spinel-type double oxide $\text{FeO Al}_2\text{O}_3$ detected [25]. The X60 steel overall has a fewer number and smaller area fractions of inclusions and is deemed less susceptible to HIC from this perspective, whereas the X70 steel overall has a greater number and larger area fractions of inclusions and is deemed more susceptible to HIC from this perspective.

Chapter 4: Results and Discussion

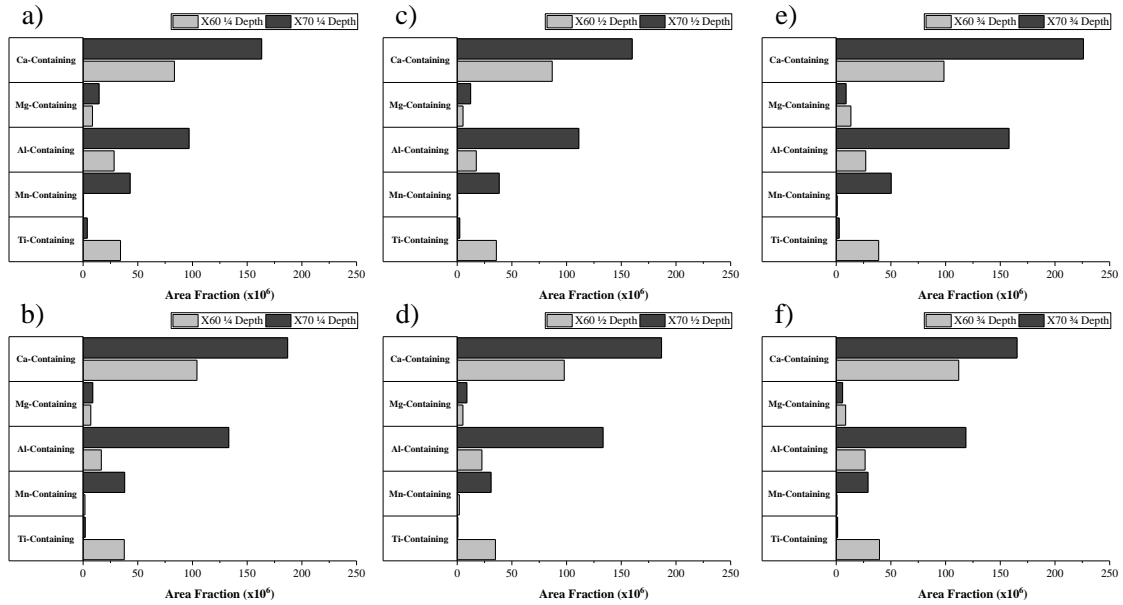


Figure 4.14: Comparison of inclusion group area fraction in the X60 and X70 steel for the (a) RD-ND plane and (b) TD-ND plane at the $\frac{1}{4}$ depth, (c) the RD-ND plane and (d) TD-ND plane for the $\frac{1}{2}$ depth, and (e) the RD-ND plane and (f) TD-ND plane for the $\frac{3}{4}$ depth.

Chapter 4: Results and Discussion

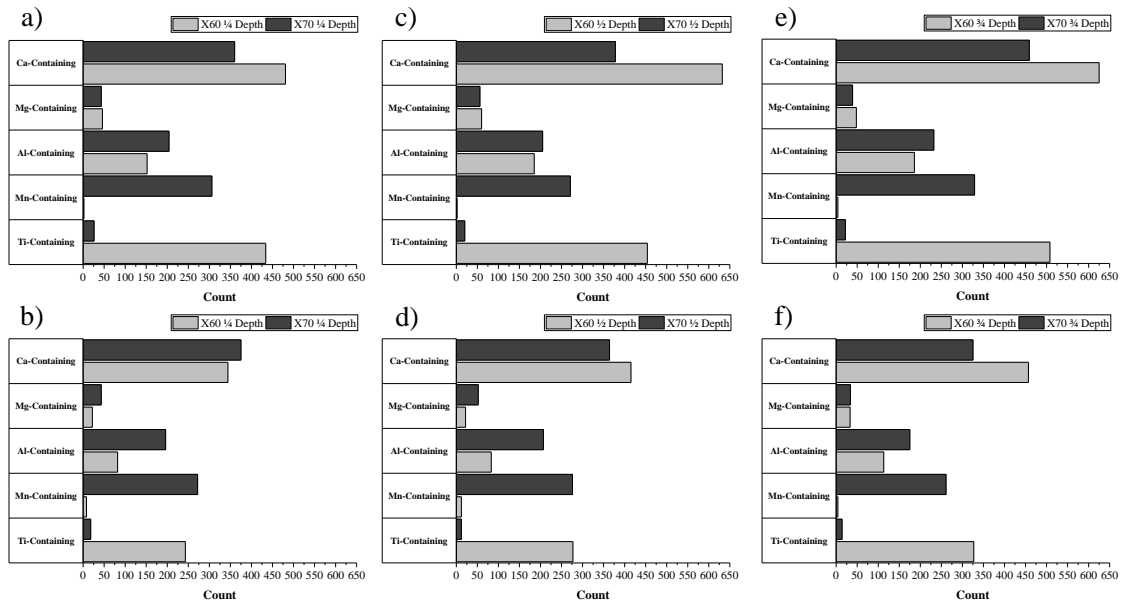


Figure 4.15: Comparison of inclusion group total count in the X60 and X70 steel for the (a) RD-ND plane and (b) TD-ND plane at the $\frac{1}{4}$ depth, (c) the RD-ND plane and (d) TD-ND plane for the $\frac{1}{2}$ depth, and (e) the RD-ND plane and (f) TD-ND plane for the $\frac{3}{4}$ depth.

Chapter 4: Results and Discussion

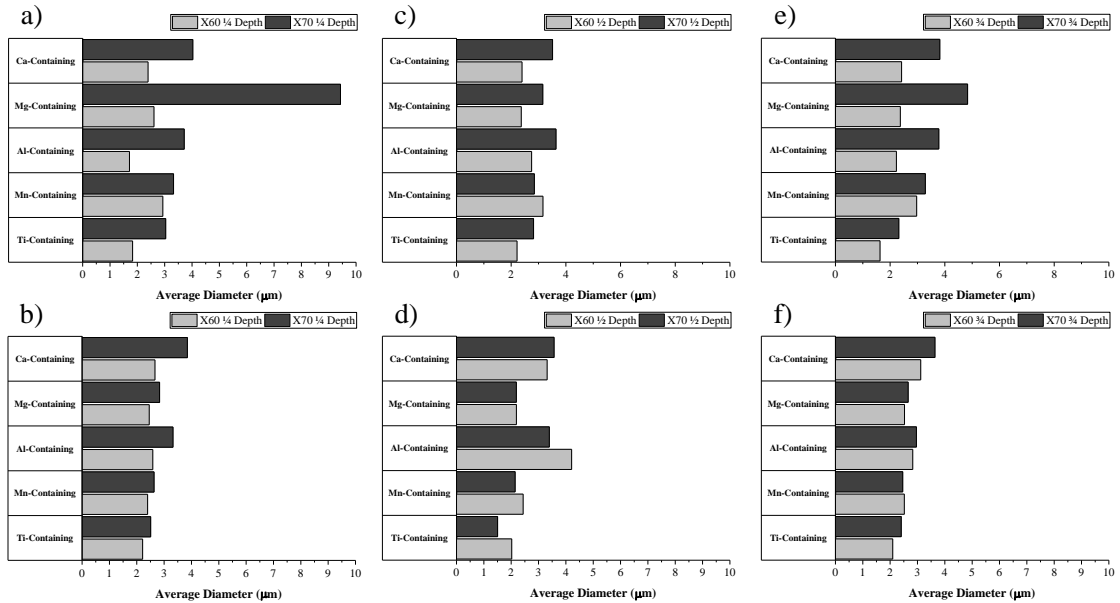


Figure 4.16: Comparison of inclusion group average diameter in the X60 and X70 steel for the (a) RD-ND plane and (b) TD-ND plane at the $\frac{1}{4}$ depth, (c) the RD-ND plane and (d) TD-ND plane for the $\frac{1}{2}$ depth, and (e) the RD-ND plane and (f) TD-ND plane for the $\frac{3}{4}$ depth.

4.2. Characterization of Diffusible Hydrogen

TDS analysis is indicative of the type of reversible and irreversible traps present in the steel skelp. Features within the microstructure that can act as reversible or irreversible traps include grain boundaries, phase boundaries, microvoids, dislocations, non-metallic inclusions, and precipitate particles [10]. The binding energy is indicative of whether a trap is considered to be reversible or irreversible; low binding energies correspond to reversible traps (grain boundaries, phase boundaries and dislocations) and high binding energies correspond to irreversible traps (non-metallic inclusions and precipitate particles) [10]. In

TDS, peaks detected at low temperatures correspond to weakly trapped hydrogen, otherwise known as reversible traps, and peaks detected at high temperatures correspond to traps deemed irreversible at ambient temperature, but reversible at high temperatures [9]. Non-metallic inclusions acting as irreversible hydrogen traps in linepipe steel are reported to include MnS, Al₂O₃-rich calcium aluminates, complex Al-Ca-Si oxides, oxides and oxysulfides of Ca and Al, Mg oxides, Mn oxides, Ti oxides, and nitrides and carbonitrides of Ti [10], [15]. Beidokhti et al. have reported that having a fine dispersion of Ti-base inclusions can act as a beneficial hydrogen trap inhibiting cracking in hydrogen sulfide environments [11]. Dong et al. reports that nitrides of Ti-base inclusions are typically very small (< 1 μm), while other inclusions and oxides tend to be larger and therefore attract more hydrogen causing the occurrence of cracking [30]. Beidokhti et al. comments that a fine dispersion of Ti-based inclusions are beneficial traps in the steel matrix due to its ability to provide dispersion strengthening and behave as innocuous permanent hydrogen traps, which provides numerous sites for the redistribution of hydrogen as well as decreases the cracking occurrence in the steel [11].

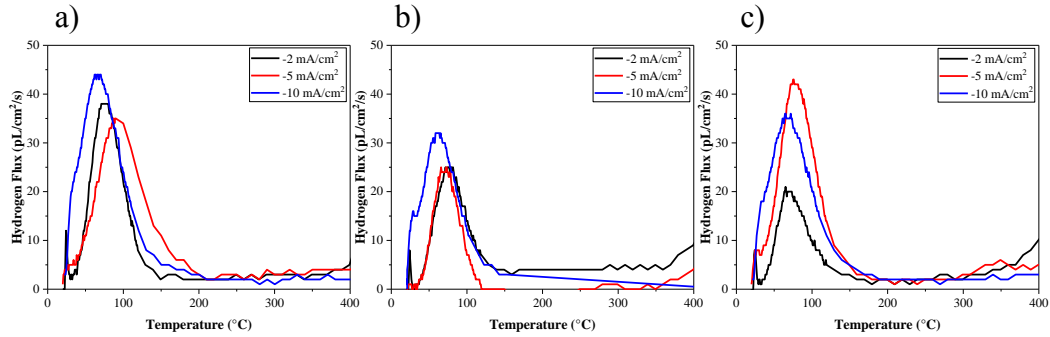


Figure 4.17: TDS data for (a) $\frac{1}{4}$ depth, (b) $\frac{1}{2}$ depth, and (c) $\frac{3}{4}$ depth of the X60 steel sample after prior galvanostatic cathodic charging.

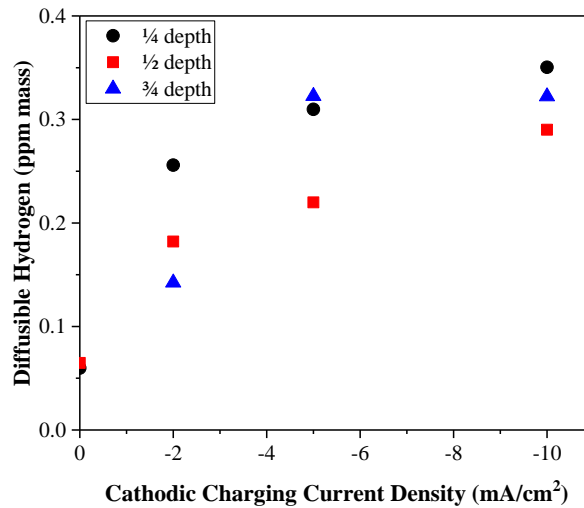


Figure 4.18: Plot of total diffusible hydrogen versus cathodic charging current density to determine hydrogen saturation.

Figure 4.17 shows the TDS data (between ambient temperature and 400°C) acquired for each of the $\frac{1}{4}$ depth, $\frac{1}{2}$ depth, and $\frac{3}{4}$ depth X60 steel samples after prior galvanostatic cathodic charging at current densities of -2 mA/cm^2 , -5 mA/cm^2 , and -10 mA/cm^2 for 2 h. Each test was duplicated, and a representative curve for each testing condition is used to display results. All curves show similar features consisting of a large maximum in the

hydrogen gas flux between ambient temperature and about 125°C, followed by a plateau region of low hydrogen flux, if any at all. There was no consistent trend in the peak hydrogen gas flux or the peak temperature as a function of current density applied during the galvanostatic cathodic polarization pre-treatment step. There was however an effect of the through-thickness depth on peak hydrogen gas flux with the ½ depth sample exhibiting the lowest peak flux after pre-charging at the two higher cathodic current densities (-5 mA/cm^2 and -10 mA/cm^2). This finding implies that the centreline (½ depth) sample has a higher capacity to trap hydrogen than either the quarterline (¼ and ¾) samples by whatever trap(s) is/are responsible for the maximum peak observed. Using the Ideal Gas Law (Equations 3.1 to 3.4), it was possible to calculate the total diffusible hydrogen for each current density and hence determine the parameters in which hydrogen saturation of the steel occurs. The result of this is shown in Figure 4.18 for each of the three through-thickness depths studied. All three curves are consistent with a parabolic-type dependence, with the diffusible hydrogen increasing with a decreasing rate as there is an increase in current density. The curves suggest that hydrogen saturation of the X60 steel is being approached at applied current densities greater than -10 mA/cm^2 for the 2 h charging period considered. This means that charging the sample using an applied current density of at least -10 mA/cm^2 for the 2 h charging period should result in sufficient hydrogen to be trapped thereby allowing easier detection for various hydrogen trapping sites through TDS analysis. This initial set of testing provided a level of confidence that an applied current density of -10 mA/cm^2 for the 2 h is sufficient to be used as a comparative basis for the two steels.

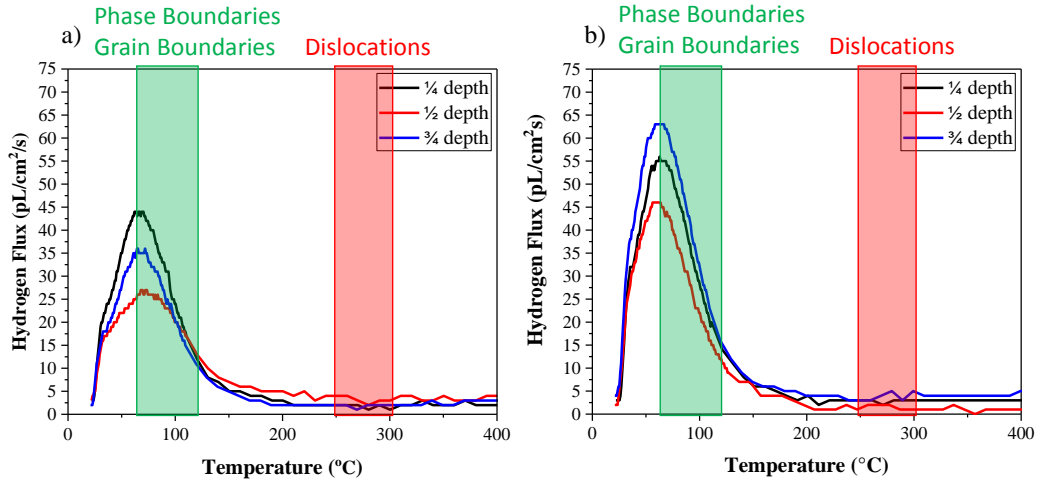


Figure 4.19: Low temperature TDS data for (a) X60 steel samples and (b) X70 steel samples after prior galvanostatic cathodic charging.

The low temperature TDS data acquired for the ¼ depth, ½ depth and ¾ depth X60 and X70 steel samples after prior galvanostatic cathodic charging at a current density of -10 mA/cm^2 for 2 h is shown in Figure 4.19. The peak temperature for ¼ depth, ½ depth, and ¾ depth X60 steel samples is approximately 63°C , 68°C , and 65°C respectively, whereas it is approximately 62°C , 66°C , and 63°C for the ¼ depth, ½ depth, and ¾ depth X70 steel samples respectively. These peak temperature values are indicative of the type of trap present in the steel matrix since the peak temperature is related to the activation energies of traps. Typically, activation energies of hydrogen traps can be calculated from the TDS peak temperatures associated with hydrogen trapping peaks when using different heating rates. A more detailed description of this method is described and executed by Escobar et al. [22]. Due to time constraints and limited availability of TDS apparatus, it was not possible to conduct the number of experiments required to calculate activation

energies corresponding to the specific hydrogen traps observed. Hydrogen flux values corresponding to the peak temperatures in the X60 and X70 low temperature TDS is shown in Table 4.3 Based on the peak hydrogen flux values, the X70 steel has a higher capacity to trap hydrogen in these low temperature traps than the X60, regardless of the through-thickness depth.

Table 4.3: Hydrogen flux values from low temperature TDS analysis as determined by peak temperature values for the detected hydrogen trapping peak.

X60 Steel			X70 Steel		
Hydrogen Flux (pL/cm ² /s)			Hydrogen Flux (pL/cm ² /s)		
1/4 Depth	1/2 Depth	3/4 Depth	1/4 Depth	1/2 Depth	3/4 Depth
44	27	36	56	46	63

Superimposed onto the plots shown in Figure 4.19 are the temperature ranges corresponding with hydrogen trapping types for low temperature peaks detected in the steel through TDS [9], [18]–[20]. It is evident from TDS results of the X60 and X70 steel skelps that hydrogen peaks in the range of 60°C to 70°C correspond to reversible grain boundary and phase boundary trapping types. In the X60 and X70 steel TDS curves, the decrease in the hydrogen flux value of the peak corresponding to grain boundary trapping types demonstrates that less hydrogen was released from the 1/2 depth sample. This may be due to the coarser grains (decreased grain boundary area) that exist within the centreline. A similar finding (decreased hydrogen flux associated with a coarser grain size) occurs when comparing the hydrogen flux measured from the X60 steel relative to the X70 steel, where

a lower hydrogen flux was detected at the low temperature peak corresponding with grain boundaries in the coarser-grained X60 steel.

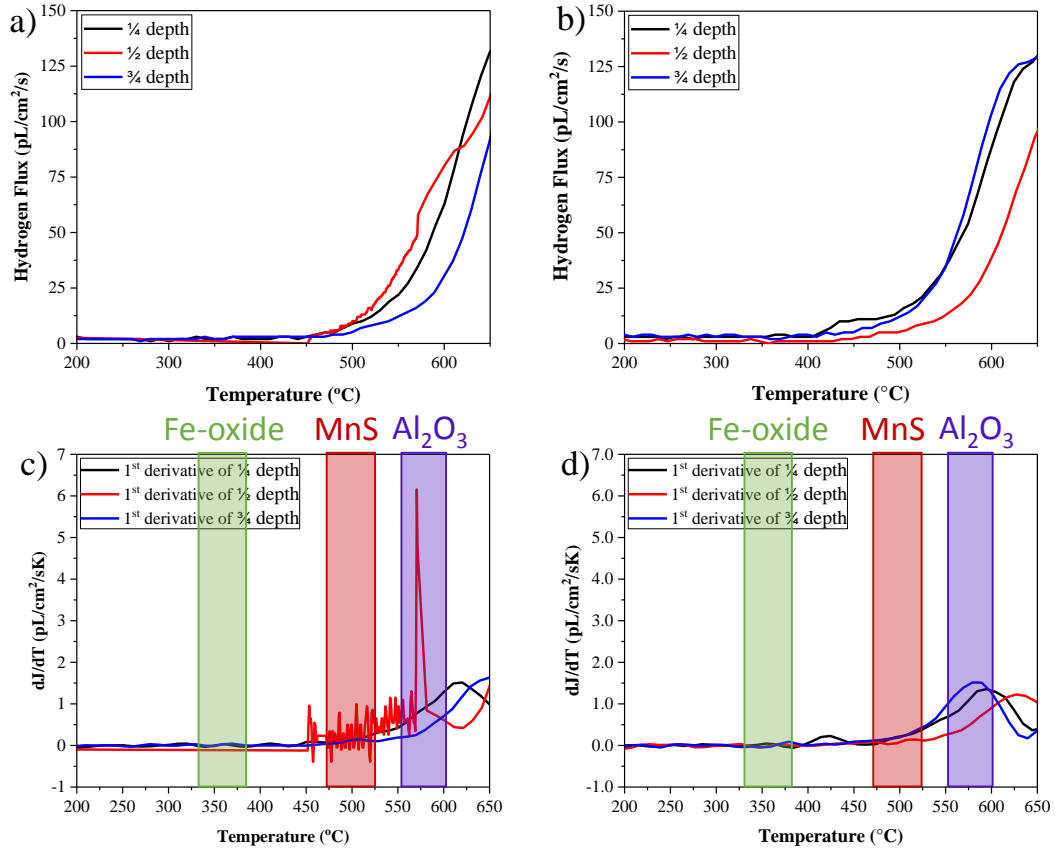


Figure 4.20: High temperature TDS data for (a) X60 steel samples and (b) X70 steel samples after galvanostatic cathodic charging, and 1st derivative plots for (c) X60 steel samples and (d) X70 steel samples.

The high temperature TDS data acquired for the 1/4 depth, 1/2 depth and 3/4 depth of the X60 and X70 steel samples after prior galvanostatic cathodic charging at a current density of -10 mA/cm^2 for 2 h is shown in Figure 4.20. First derivative plots of the TDS

data over the range from 200°C to 650°C (Figure 4.20 (c,d)) were calculated and plotted to help resolve small temperature peaks that exists in the high temperature data. From these first derivative plots, it was determined that multiple hydrogen peaks were detected and that peak temperatures for ¼ depth, ½ depth, and ¾ depth X60 steel samples were within the range of 450°C and 580°C, and that peak temperatures for ¼ depth, ½ depth, and ¾ depth X70 steel samples were within the range of 375°C and 650°C.

Superimposed onto the derivative plots in Figure 4.20(c,d) are the temperature ranges corresponding with hydrogen traps for high temperature peaks detected in steel through TDS [9], [18]–[20]. From this comparison, it is seen that hydrogen peaks detected in the X60 and X70 steel skelps may correspond to MnS inclusion and/or Al₂O₃ inclusion trap sites. Temperature ranges for hydrogen peaks associated with TiC inclusions were reported in literature to be above 700°C, which is higher than temperatures achieved during TDS experiments [9], [18]–[20].

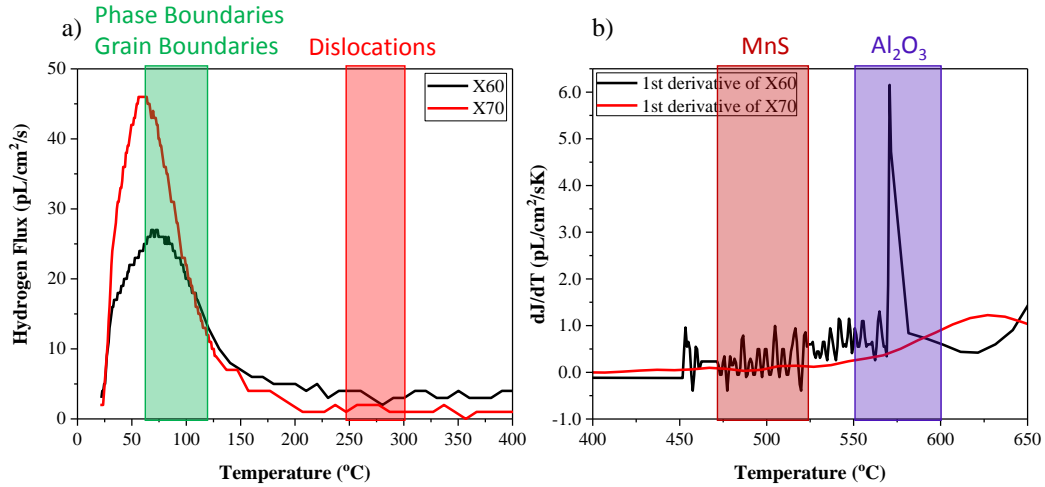


Figure 4.21: TDS data for the X60 steel and X70 steel samples from the $\frac{1}{2}$ depth for (a) low temperature analysis and (b) derivative plot of high temperature analysis after galvanostatic cathodic charging.

Figure 4.21(a) shows the TDS data acquired for the centreline ($\frac{1}{2}$ depth) X60 and X70 steel samples at low temperatures after galvanostatic cathodic charging at a current density of -10 mA/cm^2 . First derivative plots of the TDS data over the range from 400°C to 650°C (Figure 4.21(b)) were calculated to help resolve small temperature peaks that exist in the high temperature data. Figure 4.21 indicates hydrogen peaks at lower and higher temperatures, which are indicative of potential traps present in the steel matrix. An inflection point is observed at approximately 620°C for the $\frac{1}{2}$ depth X60 steel sample when prior charged at -10 mA/cm^2 for 2 h and at approximately 670°C for the $\frac{1}{2}$ depth X70 steel sample when prior charged at -10 mA/cm^2 for 2 h.

Superimposed onto the plots shown in Figure 4.21 are the temperature ranges corresponding with hydrogen trapping types for low and high temperature peaks detected in steel through TDS [9], [18]–[20]. From the comparison, the hydrogen peaks in the

temperature ranges of 450°C to 600°C detected in X60 and X70 steel skelps may corresponds to an Fe-oxide inclusion, MnS inclusion, and/or Al₂O₃ inclusion trap site. A strong inflection in the TDS data is observed at ~550°C and ~600°C for X60 and X70 steel respectively, which mostly corresponds to irreversible Al₂O₃ inclusion traps. Literature has emphasized the presence of Al₂O₃-rich Ca-aluminates in linepipe steel, especially that which has been Ca treated [12], [15], [44]. Both the ASPEX[®] analyses and SEM-EDS spot checks show that Ca-aluminate inclusion types are certainly present in both steels, whereas MnS were only detected in the X70 steel. No Fe-oxide inclusions were detected in either steel.

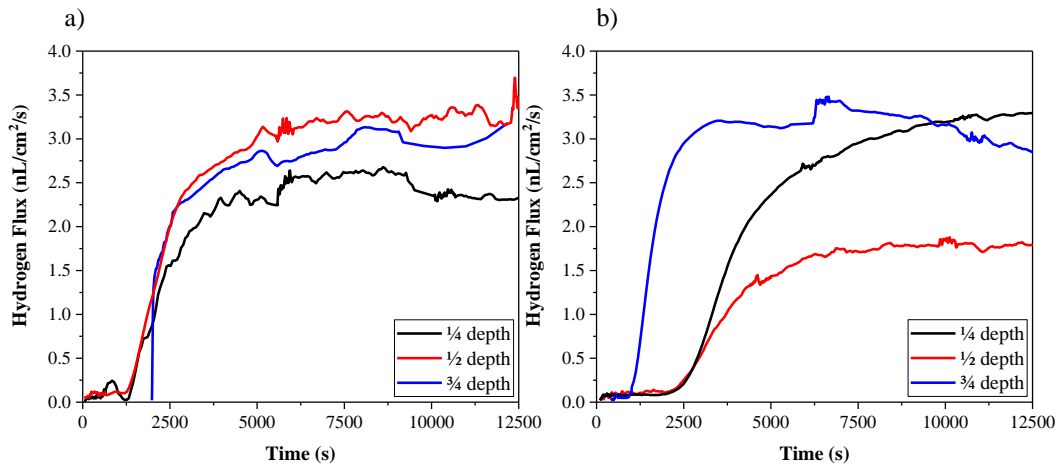


Figure 4.22: Hydrogen permeation data acquired for the (a) X60 steel samples and (b) X70 steel samples after prior galvanostatic cathodic charging.

The results of the hydrogen permeation tests conducted using X60 and X70 steel samples are shown in Figure 4.22. The curves show that there is an incubation time before any hydrogen gas flux is detected, presumably due to the time taken for hydrogen to diffuse

through the thickness of the steel sample. Once detected, the hydrogen gas flux increases rapidly before establishing a plateau, giving a relative indication on how much hydrogen is steadily diffusing through the X60 steel and X70 steel matrix comparatively through the through-thicknesses of the steel as well as comparing between the two grades of steel under investigation. As these hydrogen permeation measurements were done at room temperature, they were not performed at high enough temperatures to release hydrogen within trapping sites of high binding energies. The hydrogen release measured through these means is likely due to the grain boundaries allowing hydrogen flow through the steel matrix at room temperature. While there is a difference in the hydrogen detected among the $\frac{1}{4}$ depth, $\frac{1}{2}$ depth and $\frac{3}{4}$ depth X60 steel samples, this difference is very minor: approximately 2.3 nL/cm²/s, 3.3 nL/cm²/s, and 2.9 nL/cm²/s respectively. This can be caused by conjunction points and nodes present in the matrix acting as reversible traps, where the temperature was not quite high enough to elicit hydrogen release, or it can be caused by the presence of irreversible traps present in the steel matrix. In contrast, the hydrogen detected between the $\frac{1}{4}$ depth, $\frac{1}{2}$ depth, and $\frac{3}{4}$ depth X70 steel samples is significantly different: 3.3 nL/cm²/s, 1.8 nL/cm²/s, and 3.0 nL/cm²/s respectively. The hydrogen detected from the centreline ($\frac{1}{2}$ depth) sample is significantly less than that recorded for the quarterline ($\frac{1}{4}$ depth and $\frac{3}{4}$ depth) X70 steel samples. This can be caused by conjunction points and nodes present in the matrix acting as reversible traps, where the temperature was not quite high enough to elicit hydrogen release, or it can be caused by the presence of irreversible traps in the steel matrix. Based on the findings from TDS and hydrogen permeation, focus for HIC initiation was placed on the centrelines of the X60 and

X70 steel skelps due to the expected increased susceptibility to HE. This is due to the obvious observed differences in the hydrogen trapping capacity between the centreline and quarterline observed in the X60 and X70 steel using both TDS and hydrogen permeation analysis.

4.3. Hydrogen Embrittlement Susceptibility

It is acknowledged in literature that higher strength steels are more susceptible to HE due to an increase in the loss in ductility upon hydrogen charging, the number of potential cracking sites increasing, as well as an increased level of stress acting at these crack sites [22], [34]. Engineering stress-strain plots for the X60 and X70 steel centreline ($\frac{1}{2}$ depth) samples are shown in Figure 4.23. For metals experiencing yield point elongation, there is an upper yield point in which plastic deformation initiates and then decreases in stress to the lower yield point, where the YS is taken as the average stress with the lower yield point [52]. The yield stress (YS) and ultimate tensile stress (UTS) are approximately 423 MPa and 511 MPa respectively for the non-charged (as-received) X60 steel measured at the centreline, and 562 MPa and 643 MPa respectively for the non-charged (as-received) X70 steel measured at the centreline. After applying an elastic stress (85% of $YS_{0.2\%}$) and galvanostatic cathodic charging for 24 h in the hydrogen recombination poisoning solution, the YS of both steel centreline ($\frac{1}{2}$ depth) samples increase: 520 MPa and 543 MPa for the duplicate charged X60 steel samples, and 645 MPa, 610 MPa, and 570 MPa for triplicate

charged X70 steel samples. Prior charging to the samples also removed the YS elongation that was exhibited by both the uncharged X60 and X70 samples. Furthermore, the fracture strain of the charged samples was reduced relative to the uncharged samples, indicating a loss in ductility. The set of stress-strain curves of the charged X70 steel centreline samples, Figure 4.23(d), are quite different from one another. The testing parameters presumably remained the same for each test as there was no evidence to the contrary. The Test 1 response exhibited significant loss in ductility (embrittlement) relative to the Test 2 and Test 3 response. This could be indicative of a particularly detrimental centreline microstructural feature acting as a hydrogen trap and causing brittle fracture initiation to occur in this case.

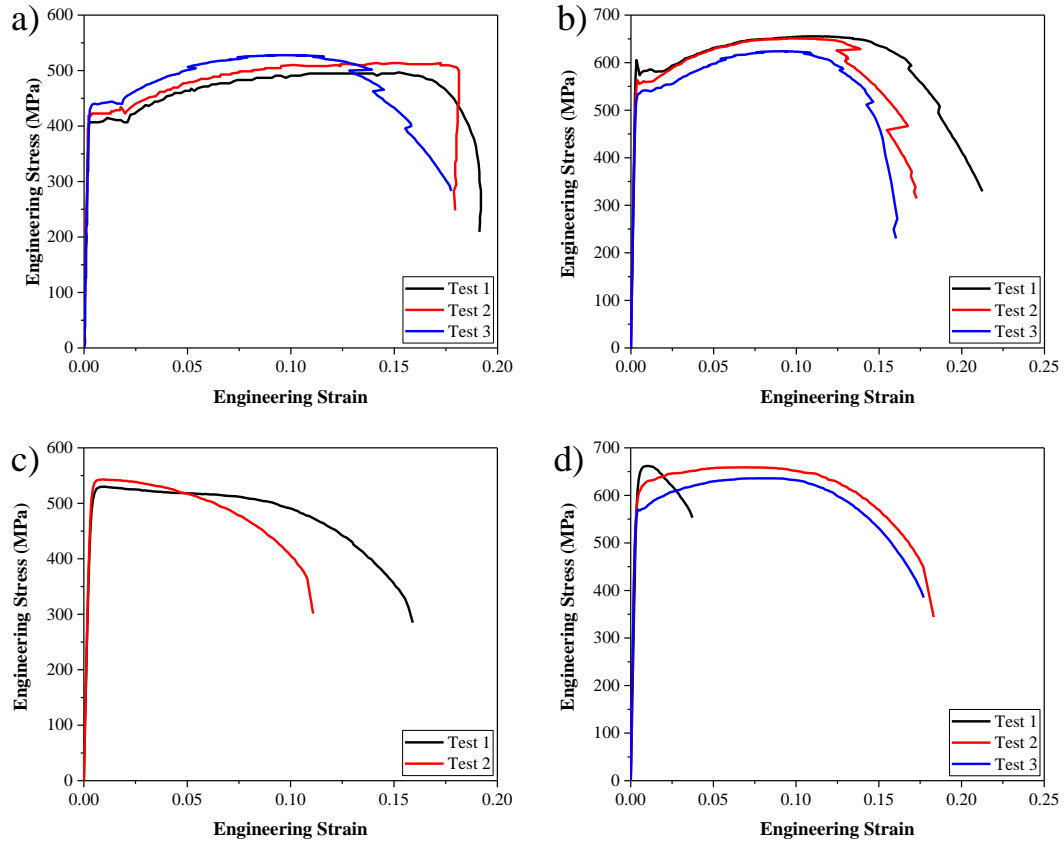


Figure 4.23: Engineering stress-strain plots of repeated sets for (a) X60 uncharged, (b) X70 uncharged, (c) X60 after charge, and (d) X70 after charge.

Table 4.4 summarizes the mechanical properties of the uncharged and charged tensile samples prepared from the two steels. Two embrittlement ratios, ER_1 and ER_2 , were calculated by comparing the failure at true strain (ϵ_f) and the percentage of reduction in area, respectively, between the uncharged and charged tensile samples. Lower values in each case correspond to higher HE susceptibility.

$$ER_1 = \frac{\epsilon_{f_c}}{\epsilon_{f_u}} \quad 4.1$$

$$ER_2 = \frac{\%RA_c}{\%RA_u} \quad 4.2$$

As expected, cathodically charging the tensile samples in a hydrogen poison-containing solution resulted in an overall loss of ductility (embrittlement) as well as an increase in the YS of the material as a result of the hydrogen entering the steel matrix and causing embrittlement. The duplicate set of charged X60 samples exhibited a consistent, yet mild embrittlement as determined using these metrics. The Test 1 charged X70 sample exhibited significant embrittlement relative to the Test 2 and Test 3 charged X70 samples, which together exhibited a consistent embrittlement. As a set, it is clear that charged X70 centreline samples were embrittled to a greater extent relative to the charged X60 centreline samples.

Table 4.4: Summary of mechanical properties for uncharged and charged tensile samples.

		YS (MPa)	UTS (MPa)	ϵ_f	%RA	ER ₁	ER ₂
X60 Uncharged	Test 1	405	495	0.175	80	-	-
	Test 2	423	511	0.164	77	-	-
	Test 3	442	528	0.164	76	-	-
	Average	423.3	511.3	0.168	78	-	-
X60 Charged	Test 1	535	549	0.147	74	0.87	0.95
	Test 2	548	550	0.105	71	0.62	0.91
X70 Uncharged	Test 1	585	654	0.196	82	-	-
	Test 2	560	651	0.162	76	-	-
	Test 3	541	624	0.155	72	-	-
	Average	562.3	643	0.171	77	-	-
X70 Charged	Test 1	650	669	0.037	28	0.22	0.37
	Test 2	623	717	0.163	68	0.95	0.89
	Test 3	575	695	0.168	65	0.98	0.85

Chapter 4: Results and Discussion

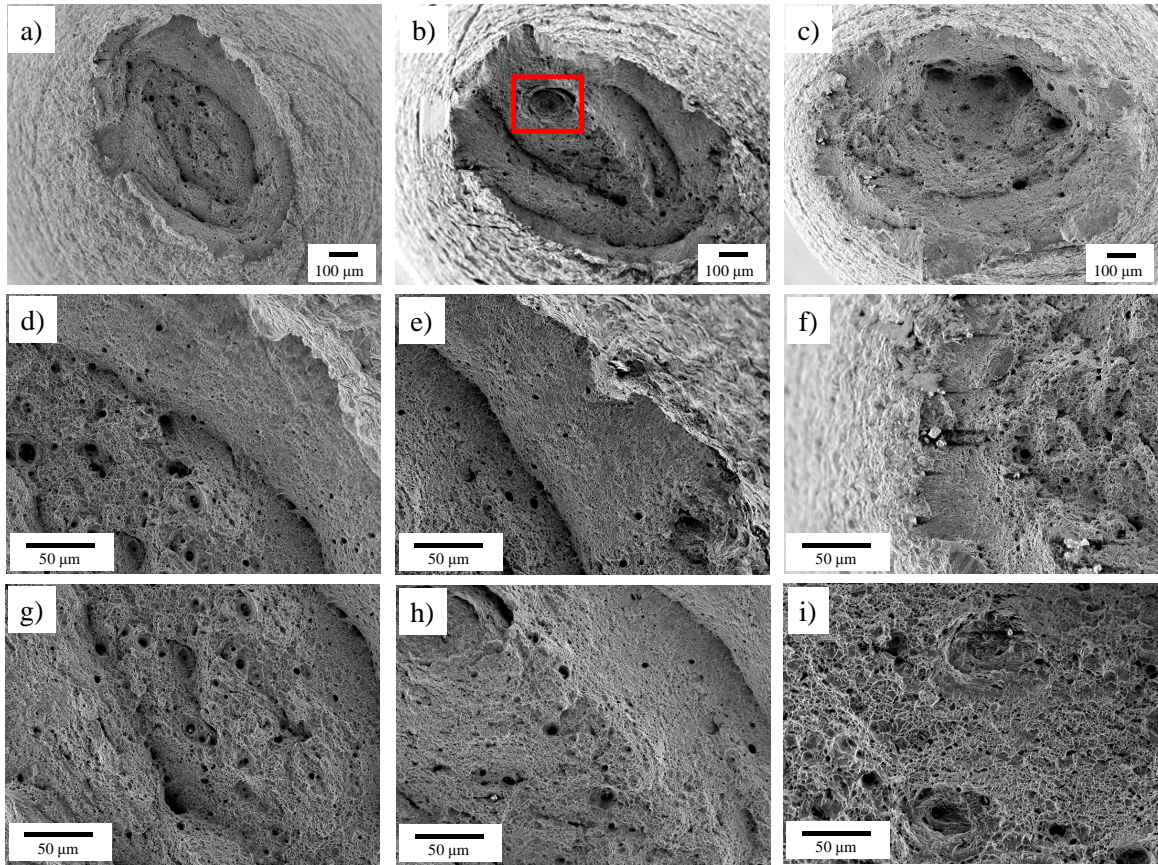


Figure 4.24: Low magnification SEM images of $\frac{1}{2}$ depth X60 steel sample fracture surfaces: (a) non-charged (starting) sample, (b) Test 1 charged sample, and (c) Test 2 charged sample. Higher magnification SEM images of outer region of (d) non-charged (starting) sample, (e) Test 1 charged sample, and (f) Test 2 charged sample and of inner region of (g) non-charged (starting) sample, (h) Test 1 charged sample, and (i) Test 2 charged sample.

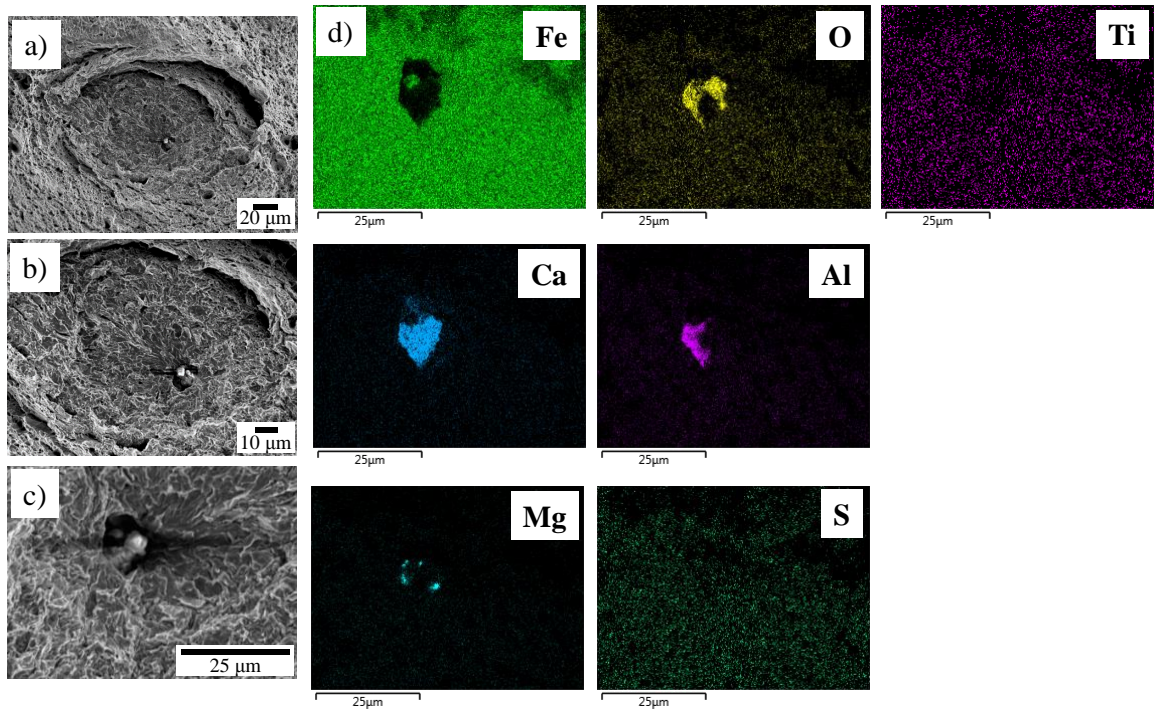


Figure 4.25: SEM images (a-c) of fish-eye feature found on the $\frac{1}{2}$ depth X60 Test 1 steel sample fracture surface at various magnifications. (d) EDS analysis of inclusion found within fish-eye feature shown in (c).

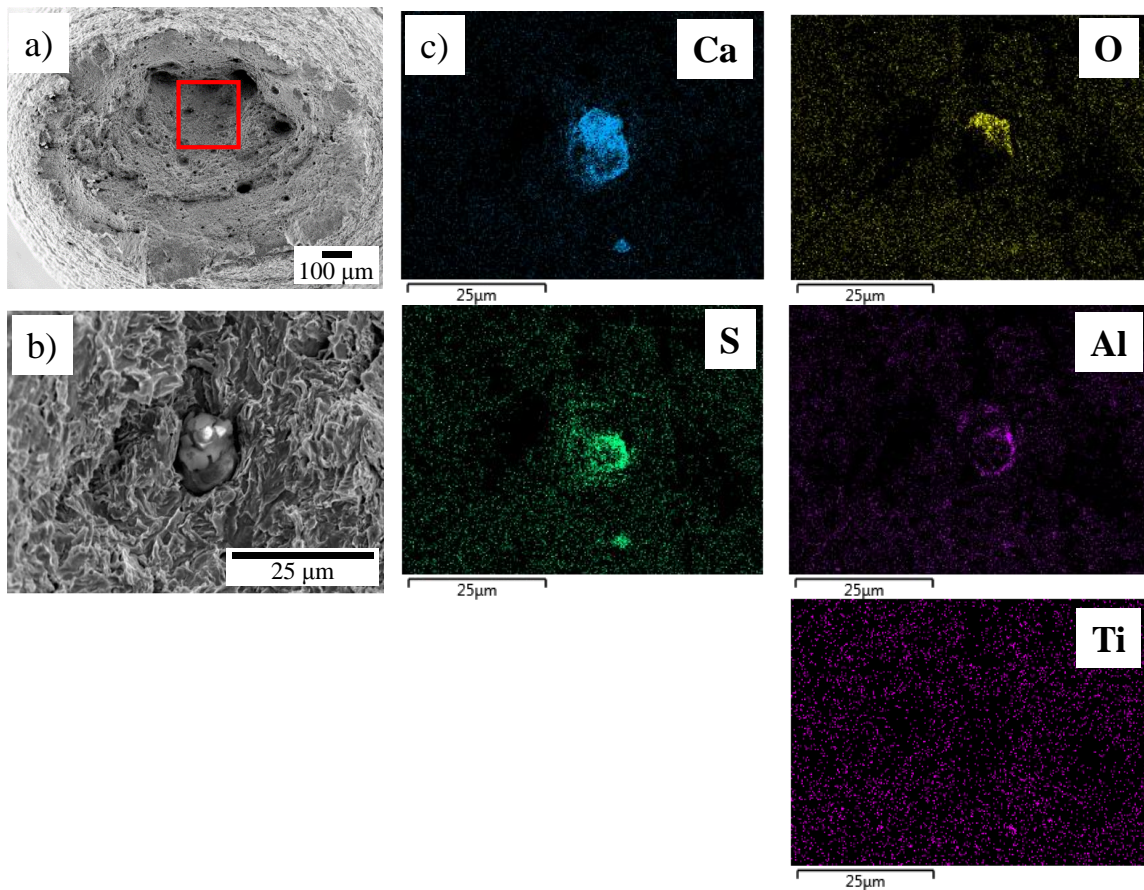


Figure 4.26: SEM images (a-b) of inclusion of interest found on the $\frac{1}{2}$ depth X60 Test 2 steel sample fracture surface at various magnifications. (c) EDS analysis of inclusion shown in (b).

Figure 4.24 shows a set of SEM images of the fracture surfaces the X60 steel centreline samples. The fracture surface of the uncharged sample consists of an outer region that exhibits shear lips and is consistent with ductile fracture mode and an inner region that exhibits dimpling which is also consistent with a ductile overload fracture mode [28], [41]–[43]. Charging the samples did not significantly change the appearance of the fracture surface relative to the uncharged sample. This observation is consistent with the relative low embrittlement ratio determined for both charged Test 1 and Test 2 samples. A ‘fisheye’

type feature, consistent with HIC cracking, was observed on the fracture surface of the charged Test 1 sample near the brittle/ductile fracture interface region, as shown in Figure 4.25 [53], [54]. An inclusion was found within the central region of fisheye feature. Clearly a significant void had formed around the inclusion, presumably from the delamination with the matrix. An EDS (area map) analysis of this inclusion, Figure 4.25(d), indicates that the inclusion is enriched in Ca, Al, Mg and O relative to the matrix. It is noted that EDS did not detect S enrichment in this inclusion, indicating that the inclusion contained within this fisheye fracture consists of oxides, which has been declared in the literature to be detrimental towards HIC susceptibility in steel [15]. A similar inspection of the charged Test 2 sample fracture surface revealed an inclusion located near the fracture interface between the shear lip and dimpled fracture region, as shown in Figure 4.26. An EDS (area map) analysis of this inclusion found on the fracture surface of the X60 Test 2 sample, Figure 4.26(c), indicated that it is enriched in Ca-Al-O and S relative to the matrix.

Chapter 4: Results and Discussion

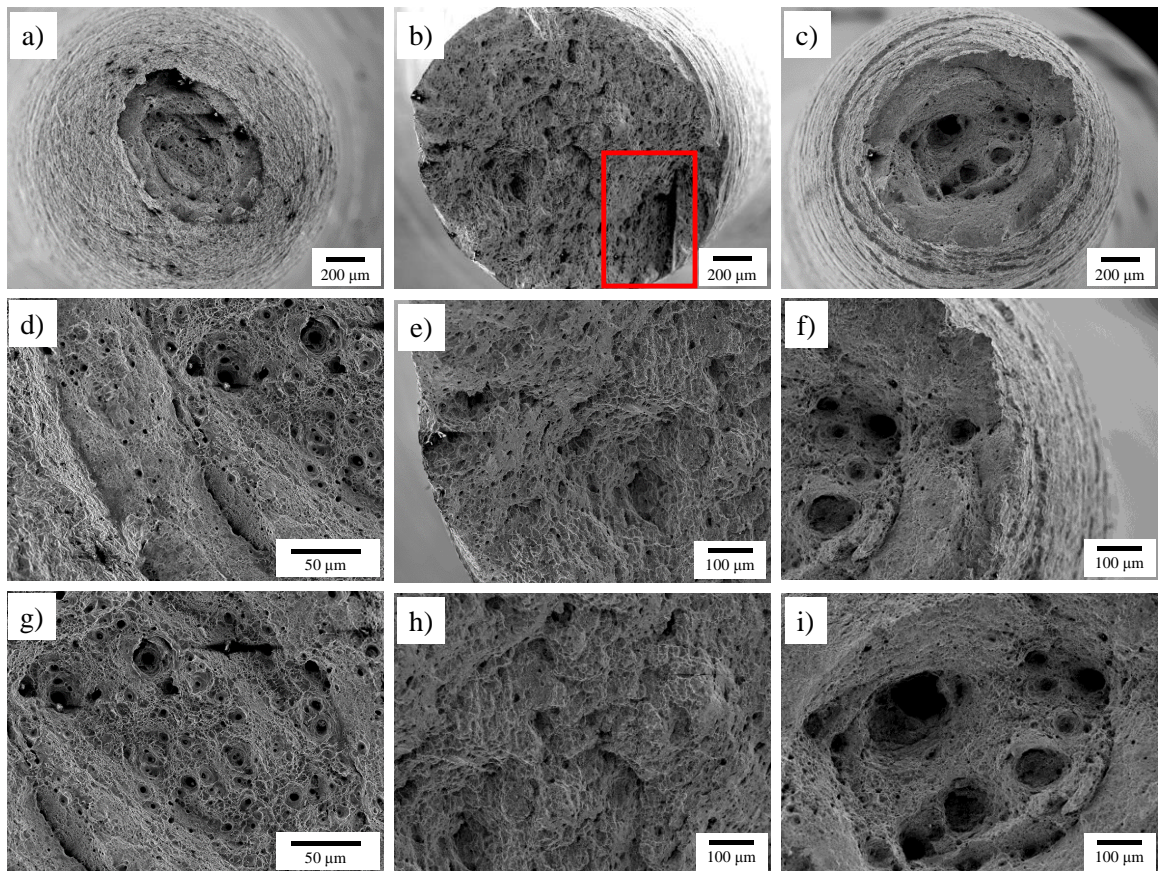


Figure 4.27: Low magnification SEM images of $\frac{1}{2}$ depth X70 steel sample fracture surfaces: (a) non-charged (starting) sample, (b) Test 1 charged sample, and (c) Test 2 charged sample. Higher magnification SEM images of outer region of (d) non-charged (starting) sample, (e) Test 1 charged sample, and (f) Test 2 charged sample and of inner region of (g) non-charged (starting) sample, (h) Test 1 charged sample, and (i) Test 2 charged sample.

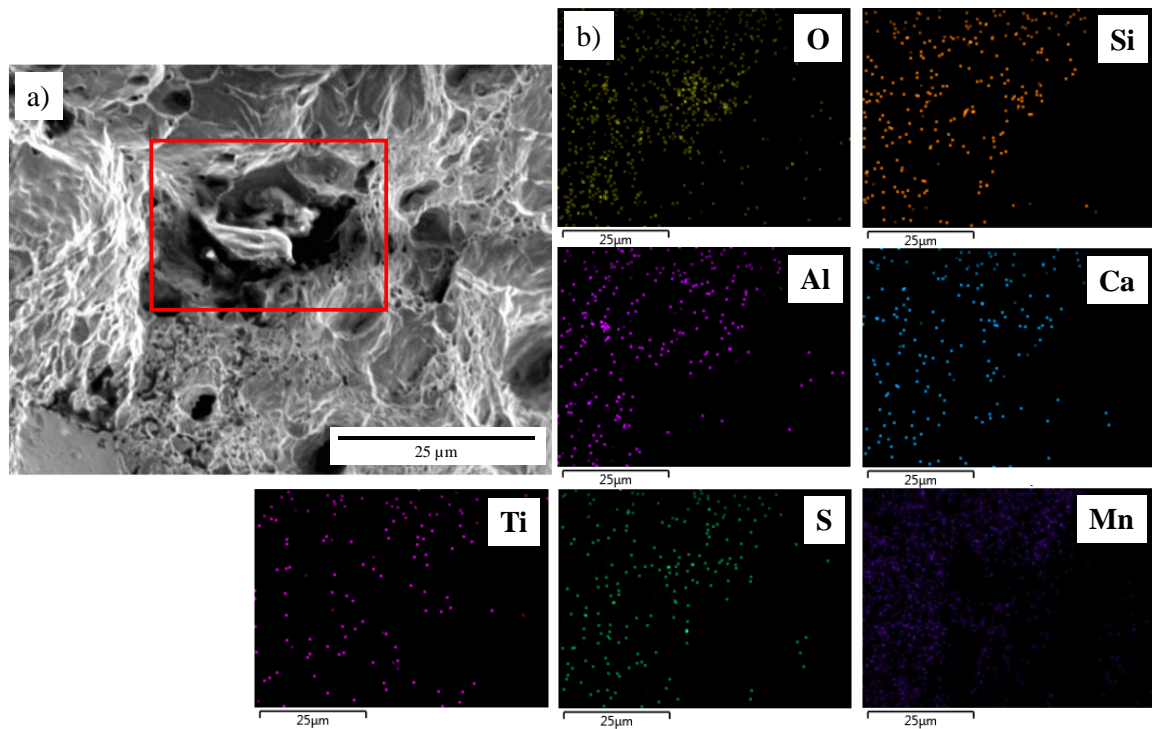


Figure 4.28: SEM images (a) of inclusion of interest found on the $\frac{1}{2}$ depth X70 Test 1 steel sample fracture surface and (b) EDS analysis of inclusion.

SEM images of the fracture surfaces of the X70 steel centreline samples are shown in Figure 4.27. The fracture surface of the uncharged sample and the fracture surface of the charged Test 2 sample consists of an outer region that exhibits shear lips and is consistent with a ductile fracture mode and an inner region that exhibits dimpling which is consistent with a ductile overload fracture mode. The entire fracture surface of the charged Test 1 sample does not contain the shear lip feature and is consistent with a brittle fracture mode, which is consistent with the relative high embrittlement ratio [28], [41]–[43]. So-called ‘ratchet marks’ are visible on the Test 1 fracture surface as well, which occur when multiple cracks initiating from different sites join together [55]. Figure 4.28 shows an SEM image of an inclusion found along the brittle fracture surface of the charged Test 1 sample. An

associated EDS (area map) analysis of the inclusion was attempted, and is shown in Figure 4.28(b). Unfortunately, due to the configuration of the sample, the X-ray signals were unable to reach the EDS detector, and therefore elemental analysis could not be completed on the inclusions imaged along the tensile fracture surface. In order to obtain the elemental presence within the inclusion, it is necessary to use focused ion beam (FIB) methods to isolate the inclusion allowing for further analysis to characterize the inclusion. Assuming that the microstructure was indeed susceptible to hydrogen embrittlement as the stress-strain curve suggests, then one possible cause is the presence of a higher volume fraction of the bainite phase, which is a harder phase relative to ferrite and is known to have a higher capacity to trap hydrogen [10], [12]. However, if true, then the other two charged samples should have exhibited a similar hydrogen embrittlement susceptibility as they were all appeared from the centreline region of the X70 steel skelp. As previously mentioned, a more detailed EBSD phase characterization is required to confirm if harder phases have indeed preferentially formed at the centreline. Another possible cause is the presence of particularly problematic inclusions.

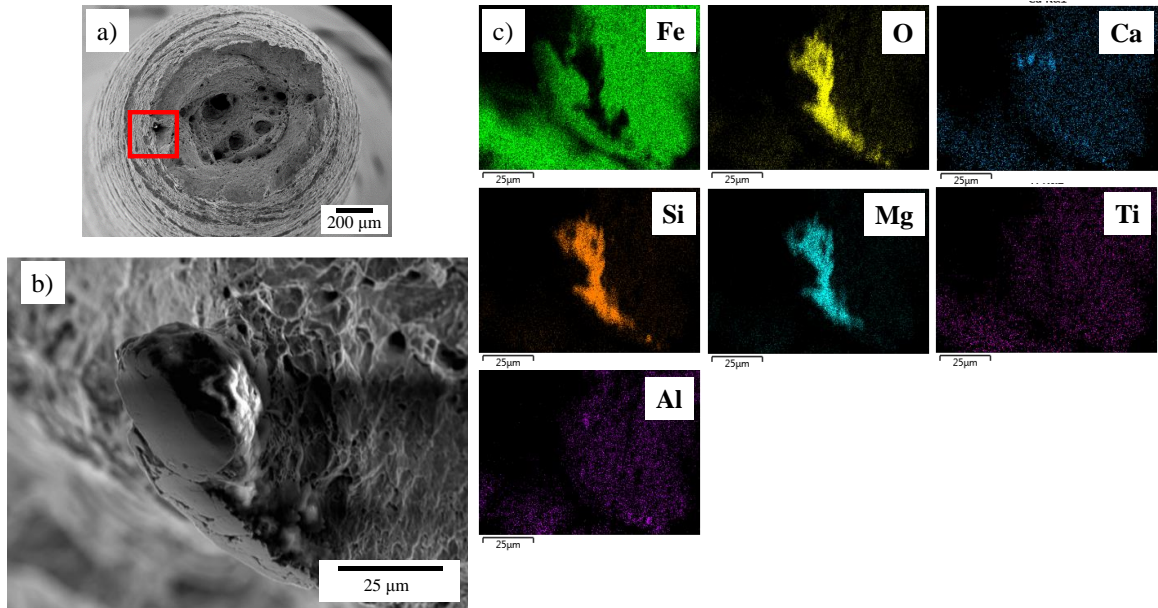


Figure 4.29: SEM images (a-b) of inclusion of interest found on the $\frac{1}{2}$ depth X70 Test 2 steel sample fracture surface at various magnifications. (c) EDS analysis of inclusion shown in (b).

The fracture surface of the other two charged samples (Test 2 and Test 3 samples) exhibited features similar to the uncharged sample: an outer region that is consistent with a brittle fracture mode and an inner region that is consistent with a ductile overload fracture mode. This observation is consistent with the relative low embrittlement ratio determined for both charged Test 2 and Test 3 samples. Figure 4.29 shows an SEM image of an inclusion found embedded in the outer brittle fracture region of the charged Test 2 sample. An associated EDS (area map) analysis of the inclusion is also observed. The EDS area maps indicates that this inclusion is enriched in Mg, Si and O relative to the matrix. Overall, this inclusion does not appear to be problematic as no decohesion is observed between the inclusion and steel matrix.

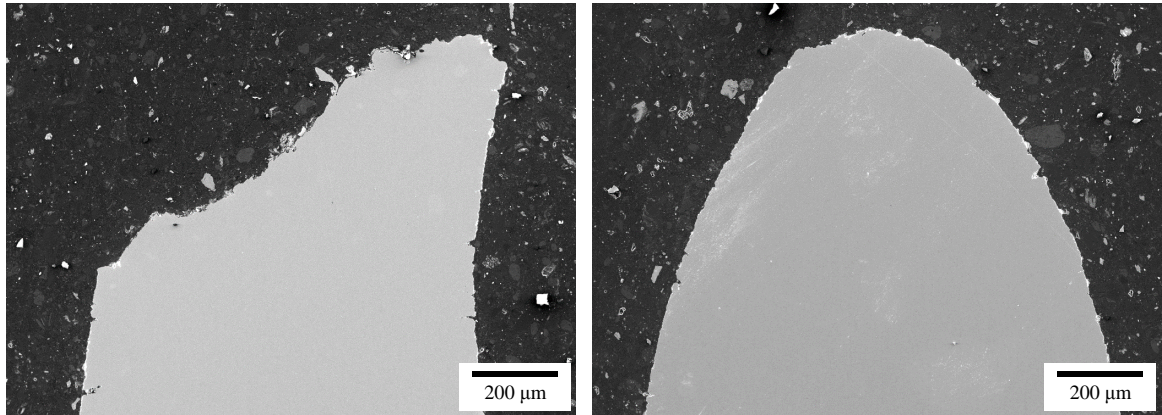


Figure 4.30: SEM image of 1/2 depth X70 steel sample fracture surface in cross-section: a) Test 1, and b) Test 2.

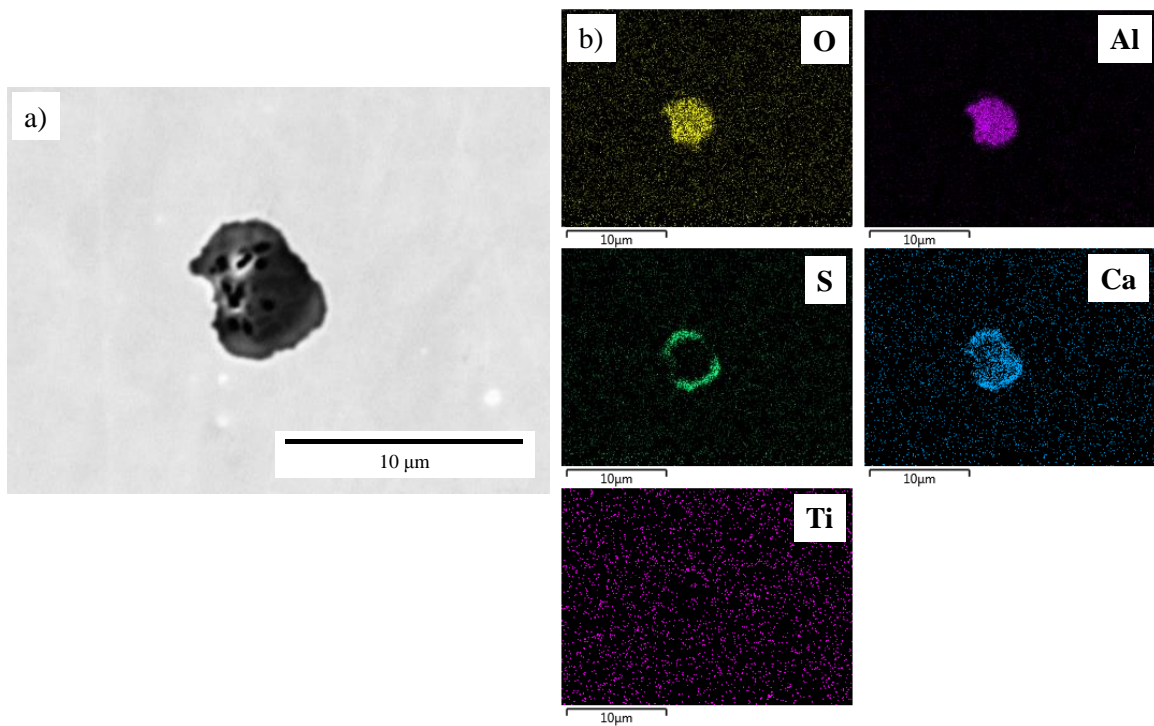


Figure 4.31: (a) SEM image and (b) associated EDS maps of inclusion found on 1/2 depth X70 Test 1 steel sample cross-section close to fracture surface.

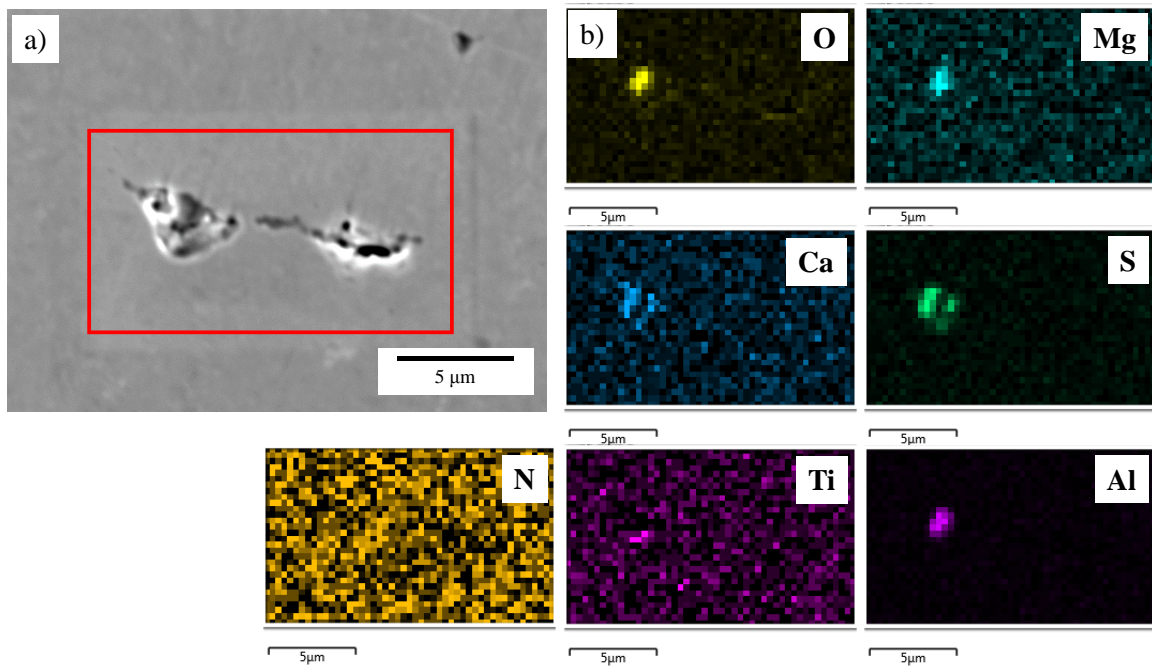


Figure 4.32: (a) SEM image (b) and associated EDS maps of inclusion found on $\frac{1}{2}$ depth X70 Test 2 steel sample cross-section close to fracture surface.

Figure 4.30 shows the SEM images of the charged Test 1 and Test 2 X70 sample fracture surfaces in cross-section. A clear difference exists between the two samples. The Test 1 sample shows very little necking and the full fracture is at a 45° angle to the tensile axis, which is indicative of brittle fracture, whereas the Test 2 sample shows necking in a manner typical for semi-ductile materials [42], [43]. No evidence of well-developed secondary cracking was observed on either sample. Figure 4.31 and Figure 4.32 show the SEM images and associated EDS (area map) analyses of inclusions found near the fracture surface of both charged samples. The inclusion imaged in the Test 1 sample is enriched in Ca, Al, O and S relative to the matrix, whereas the inclusion imaged in the Test 2 sample is enriched in Ca, Al, Mg, O and S relative to the matrix.

Figure 4.33 summarizes the area fraction and count of specific element containing inclusions for the centreline depths of the X60 and X70 steel. From the ASPEX[®] results, it is obvious that the X70 steel contains MnS inclusions where the X60 steel does not. Furthermore, the X70 steel contained a higher area fraction of irreversible inclusion types, including Al₂O₃-rich calcium aluminates, than the X60 steel, which could contribute to the difference of detectable hydrogen between the ½ depths of the X60 and X70 steel skelps, Figure 4.34. In addition, based on findings by Moon et al. and Park et al. it is known that phases of higher hardness, such as bainite, segregate at the centreline of steel slabs and act as reversible hydrogen traps [12], [27]. Therefore, the presence of bainite in the X70 steel could be a cause of the behavioural difference observed between the ½ depth to the ¼ and ¾ depths of the X70 steel skelp, and the difference between the ½ depths of the X60 and X70 steel skelps, Figure 4.34.

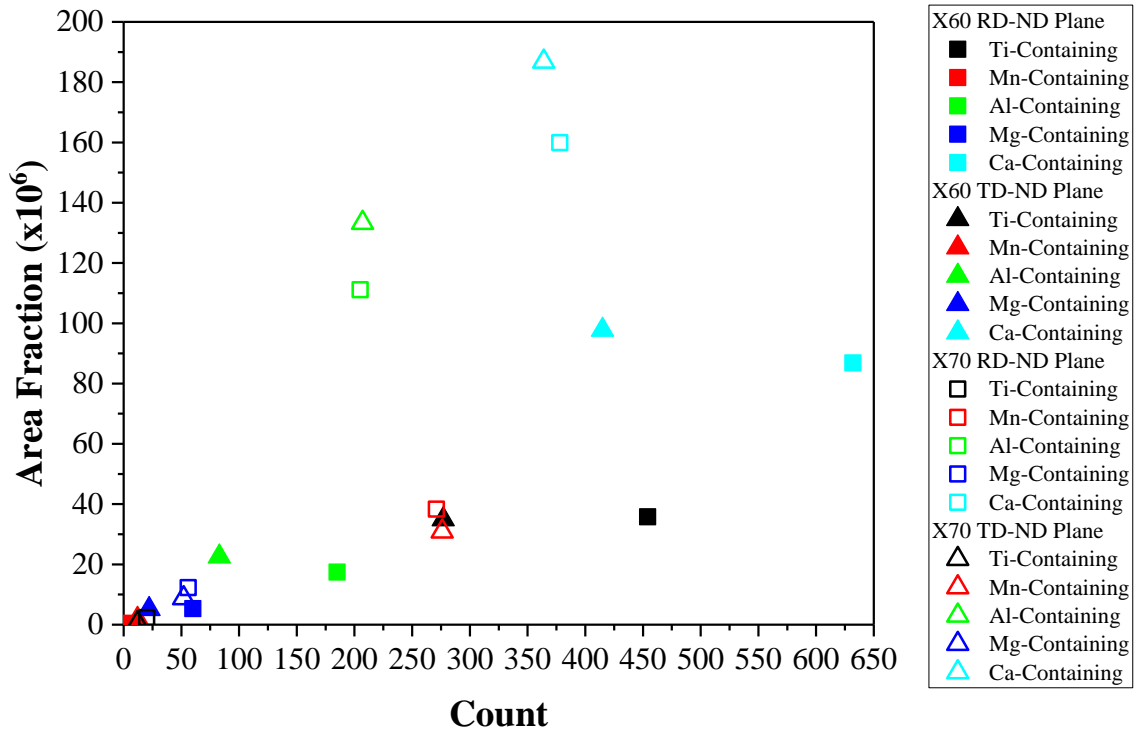


Figure 4.33: Area fraction versus count for each inclusion type detected through ASPEX[®] at the $\frac{1}{2}$ depth for X60 and X70 steel skelps.

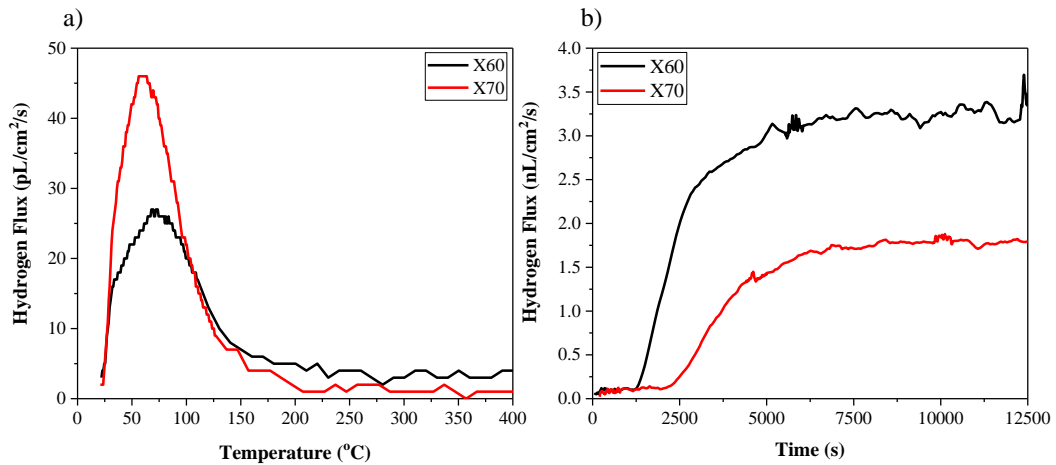


Figure 4.34: Comparison of the centreline behaviour between X60 and X70 steel skelps during (a) TDS, and (b) hydrogen permeation.

Dong et al. have reported that cracking as a result of hydrogen typically initiates from Ca-Al oxide inclusions rather than Ti carbonitrides [30]. This remains consistent with the results from SEM-EDS of inclusions detected along the fracture surfaces of the X60 and X70 charged specimens, where no Ti-containing inclusions were observed. Types of inclusions that were observed along the fracture surfaces include oxides and oxysulfides of Ca and Al, oxides of Mg, and Al-Ca-Si oxides. Literature findings along with the reported TDS analyses demonstrate that Al_2O_3 inclusion types are acting as irreversible traps in the steel matrix, and that Mg oxides, Ca oxysulfides, and MnS can hinder the performance of linepipe steel [10], [12], [15].

Mohtadi-Bonab et al. did a comparative study on X60 and X70 linepipe steel, where it was observed through spot analysis that the X60 steel lacked MnS inclusions whereas the X70 steel contained MnS inclusions [33]. This corresponds well to what was observed in this study through ASPEX[®] analysis: the X70 steel was observed to be populated with more Mn-containing inclusions than the X60 steel. It was observed in the study conducted by Mohtadi-Bonab et al. that cracks initiated from the MnS inclusions in the X70 steel and it was reported to be one of the main factors contributing to HIC susceptibility in linepipe steel [33]. ASPEX[®] analysis done in this current study also revealed an increase in the number of Al-containing inclusions and a decrease in the number of Ti-containing inclusions. Thus based on this, a conclusion has not yet been reached on what exactly is the problematic inclusion leading to crack initiation.

4.4. Outlook

There was limited success in unraveling the evidence of specific microstructural features acting as detrimental hydrogen trapping sites which lead to HIC and HE susceptibility in linepipe steel. Results obtained in this study are consistent with results provided by Mohtadi-Bonab et al. which indicates that both types of traps (reversible and irreversible) may play contributing roles to the overall HIC mechanism [33]. A more creative approach is necessary to look at isolating the various traps and interrogating them on a trapping capacity basis. Given the advances in micromechanical testing, using site specific samples prepared by focused-ion beam (FIB), this is certainly possible and a worthwhile pathway that needs to be explored [56]–[60].

The other interesting result from this study is the observation of a Ti-skin forming around the inclusions imaged through SEM-EDS techniques. In literature, it has been stated that Ti inclusions are beneficial from a HIC perspective due to uniform distribution of a small size particle [30]. Observations from this study lead to the proposal that it may be another mechanism, one that involves a Ti-skin rendering an otherwise potent trap ineffective. In future research, it would be interesting to look at a model steel containing a Ti-carbonitride interface to further investigate its hydrogen trapping capacity.

Chapter 5: Conclusions

The aim of this research was to identify problematic microstructural features as hydrogen traps in linepipe steel that serve to increase the hydrogen embrittlement susceptibility. A comparison was made between the hydrogen trapping capacity and associated hydrogen embrittlement susceptibility of Ca treated X60 grade steel skelp and X70 grade steel skelp: the latter typically being more susceptible to hydrogen-induced cracking in sour environments. Major conclusions extracted from this study can be summarized as follows:

1. ASPEX[®] analysis reveals that quarterline depths are homogeneous relative to the centreline depths in both materials in terms of type, count, and area fraction of inclusions. X70 contains a higher number of inclusions, and larger area fractions, depicting that it is not as clean of a steel as the X60. In terms of major inclusion types, major differences include higher quantities and area fractions of Mn- and Al-containing inclusions, but fewer quantities and area fractions of Ti-containing inclusions were detected in the X70 steel skelp compared to the X60 steel skelp. Inclusion differences were only observed when comparing the two steel grades with one-another, but not within the steel grade through-thicknesses.
2. Hydrogen permeation analysis in the X60 steel skelp shows little variance between the quarterline and centreline, consistent with ASPEX[®] inclusion analysis. Hydrogen permeation analysis in the X70 steel skelp shows difference between centreline and quarterline, with the centreline showing a higher capacity to trap.

Observations made through ASPEX[®] analysis indicated that this difference in the hydrogen trapping between the centreline and quarterline of the X70 steel is not inclusion related. This suggests that centreline segregation of hard phase is likely responsible for this.

3. Significant differences in the reversible hydrogen trapping capacity between the X60 and X70 steel grades were observed. X70 has the higher reversible trapping capacity as shown by the TDS results. This is consistent with the proposed centreline segregation previously explained. Both X60 and X70 steel grades show irreversible traps are contributing factors to HE, but given the differences in the major inclusion types present, it is expected that these irreversible traps also play a role in the HE susceptibility differences between the two grades in question.
4. The X70 has larger amounts of Al inclusions and MnS inclusions, both of which are well known to cause HIC. However, the X70 contains fewer Ti-containing inclusions than the X60 steel skelp. This is intriguing because from literature it is known that Ti needs to be well dispersed fine particles, but it has been observed through SEM-EDS ‘spot check’ inclusion analysis that the Ti is forming a skin around inclusions. It is possible this Ti-skin renders the inclusion as being an effective trap for HIC initiation.
5. A decision has not yet been reached on which heterogeneities are problematic to X70 in the centreline. It has been mentioned that hard phases tend to segregate towards the centreline of steel skelp, but the occurrence of this was not confirmed through this study. Conventional approaches, as used here, may not be the way to

go as there are too many variables. Rather, techniques such as the micro-mechanistic techniques explained in Section 4.4. should be further explored due to the capability to isolate and then further analyse features of interest.

Appendix I: Calibration of CorTest[®] Proof Ring

Calibration of the CorTest[®] proof ring was conducted using a 10 kN tensile test frame, where a uniaxial compressive force was applied to the proof ring. The ring deflection (mm), d , was measured with the corresponding applied axial load. Deflection values were recorded for when the compressive axial load was being applied, and while it was being released, Table I.1 and Table I.2 respectively. The resulting calibration curve is shown in Figure 3.10.

Table I.1: Deflection values corresponding to applied compressive axial load.

Axial Load (N)	Deflection (mm)
0	0
7.2	0.07
330	0.13
956	0.22
1551	0.30
2378	0.40
3038	0.47
3952	0.57
4903	0.67

Table I.2: Deflection values corresponding to released compressive axial load.

Axial Load (N)	Deflection (mm)
0	0
496	0.14
1114	0.22
1633	0.29
2076	0.37
2861	0.43
3511	0.50
4182	0.58
4870	0.66
5720	0.75

Appendix II: Inclusions Detected in X60 and X70 Steel

SEM-EDS techniques described in Section 3.2. were used to image inclusions detected in the X60 grade steel skelp and X70 grade steel skelp. Some of the inclusions imaged through this ‘spot check’ technique are shown in Table II.1 and Table II.2 for the X60 and X70 steel skelps respectively.

Table II.1: SEM-EDS images of inclusions detected in the X60 grade steel skelp.

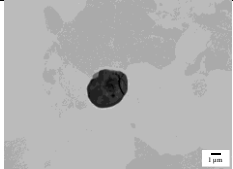
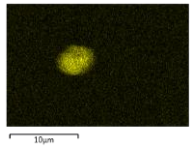
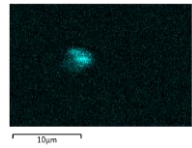
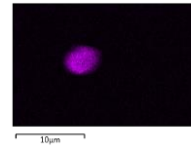
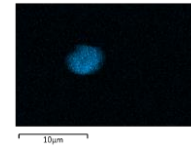

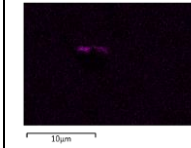
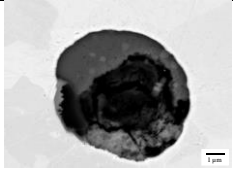
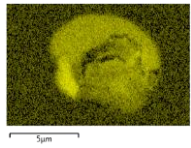
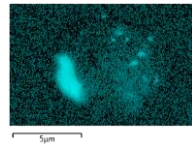
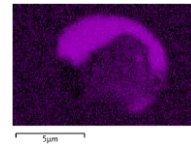
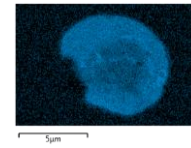
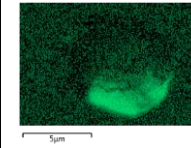
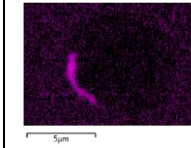
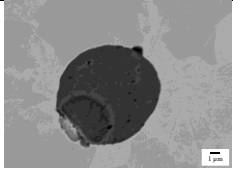
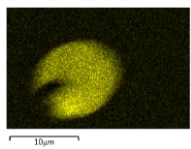
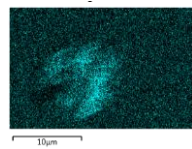
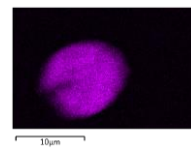
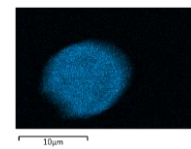


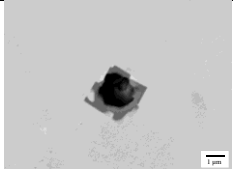
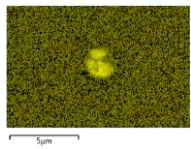
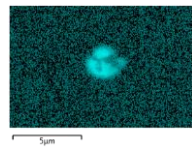

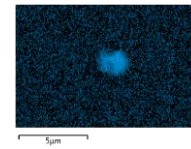
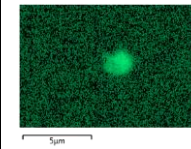
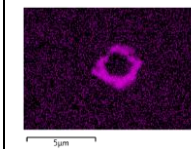
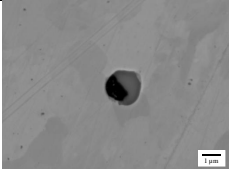
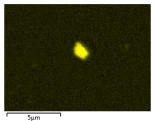

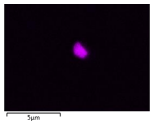
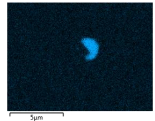
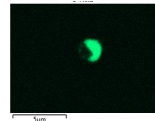
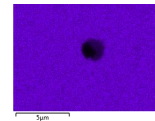
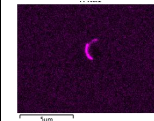
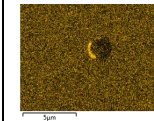
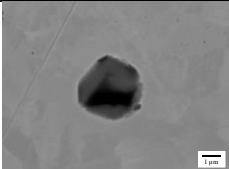
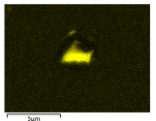
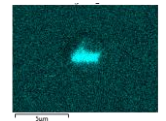
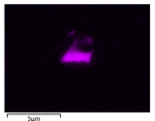
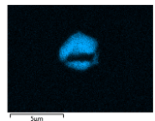
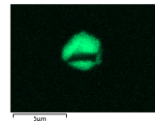
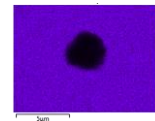
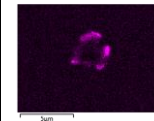
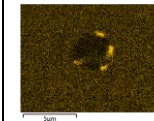
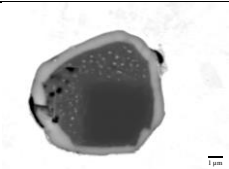
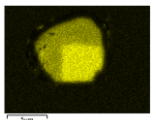
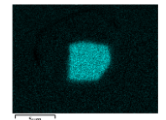
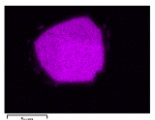
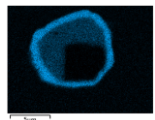
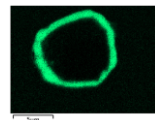
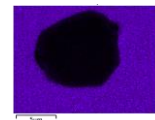
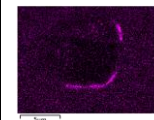
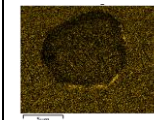
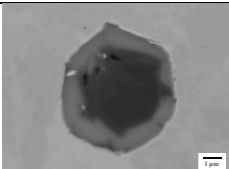
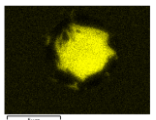
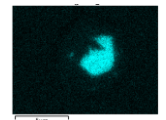
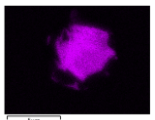
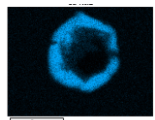
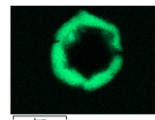
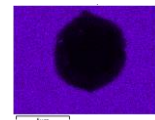
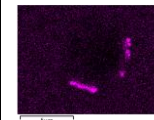
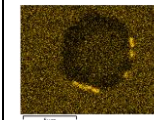
SEM Image of Inclusion	O	Mg	Al	Ca	S	Ti
						
						
						
						

Table II.2: SEM-EDS images of inclusions detected in the X70 grade steel skelp.

SEM Image of Inclusion	O	Mg	Al	Ca	S	Mn	Ti	N
								
								
								
								

References

References

- [1] T. L. Guidotti, “Occupational exposure to hydrogen sulfide in the sour gas industry: some unresolved issues,” *Int. Arch. Occup. Environ. Health*, vol. 66, no. 3, pp. 153–160, 1994.
- [2] G. Domizzi, G. Anteri, and J. Ovejero-García, “Influence of sulphur content and inclusion distribution on the hydrogen induced blister cracking in pressure vessel and pipeline steels,” *Corros. Sci.*, vol. 43, pp. 325–339, 2001.
- [3] A. Kawashima, K. Hashimoto, and S. Shimodaira, “Hydrogen electrode reaction and hydrogen embrittlement of mild steel in hydrogen sulfide solutions,” *Corrosion*, vol. 32, no. 8, pp. 321–331, 1976.
- [4] R. W. Revie, V. S. Sastri, M. Elboudjaini, R. R. Ramsingh, and Y. Lafrenière, “Hydrogen-Induced Cracking of Line Pipe Steels Used in Sour Service,” *CORROSION*, vol. 49, no. 7, pp. 531–535, 1993.
- [5] “ANSI/NACE TM0177-2016 Testing of Metals for Resistance to Sulfide Stress Cracking and Stress Corrosion Cracking in H₂S Environments,” no. 21212. NACE International, Houston, TX, 2016.
- [6] “ANSI/NACE TM0284-2003 Standard Test Method Evaluation of Pipeline and Pressure Vessel Steels for Resistance to Hydrogen-Induced Cracking,” no. 21215. NACE International, Houston, TX, 2003.
- [7] A. J. Haq, K. Muzaka, D. P. Dunne, A. Calka, and E. V Pereloma, “Effect of microstructure and composition on hydrogen permeation in X70 pipeline steels,” *Int. J. Hydrogen Energy*, vol. 38, no. 5, pp. 2544–2556, 2013.
- [8] M. A. Mohtadi-Bonab, J. A. Szpunar, L. Collins, and R. Stankievech, “Evaluation of hydrogen induced cracking behavior of API X70 pipeline steel at different heat treatments,” *Int. J. Hydrogen Energy*, vol. 39, pp. 6076–6088, 2014.
- [9] H. K. D. H. Bhadeshia, “Prevention of Hydrogen Embrittlement in Steels,” *ISIJ Int.*, vol. 56, no. 1, pp. 24–36, 2016.
- [10] D. Hejazi, A. J. Haq, N. Yazdipour, D. P. Dunne, A. Calka, F. Barbaro, and E. V. Pereloma, “Effect of manganese content and microstructure on the susceptibility of X70 pipeline steel to hydrogen cracking,” *Mater. Sci. Eng. A*, vol. 551, pp. 40–49, 2012.
- [11] B. Beidokhti, A. Dolati, and A. H. Koukabi, “Effects of alloying elements and microstructure on the susceptibility of the welded HSLA steel to hydrogen-induced cracking and sulfide stress cracking,” *Mater. Sci. Eng. A*, vol. 507, pp. 167–173, 2009.

References

- [12] J. Moon, S.-J. Kim, and C. Lee, “Role of Ca Treatment in Hydrogen Induced Cracking of Hot Rolled API Pipeline Steel in Acid Sour Media,” *Met. Mater. Int.*, vol. 19, no. 1, pp. 45–48, 2013.
- [13] L. Shi, J. Chen, and D. O. Northwood, “Effect of Rare Earth and Calcium Treatments on the Mechanical, Physical, and Electrochemical Properties of a 16Mn Steel,” *J. Mater. Eng. Perform.*, vol. 1, no. 1, pp. 21–27, 1992.
- [14] D. A. Jones, *Principles and Prevention of Corrosion*, 2nd ed. Upper Saddle River, NJ: Prentice Hall, 1996.
- [15] X. Yin, Y. H. Sun, Y. D. Yang, X. X. Deng, and A. McLean, “Effects of non-metallic inclusions and their shape modification on the properties of pipeline steel,” *Iron Steel Technol. Conf. Proc.*, vol. 3, pp. 3388–3406, 2015.
- [16] X. B. Shi, W. Yan, W. Wang, L. Y. Zhao, Y. Y. Shan, and K. Yang, “HIC and SSC Behavior of High-Strength Pipeline Steels,” *Acta Metall. Sin. (English Lett.)*, vol. 28, no. 7, pp. 799–808, 2015.
- [17] C. A. Zapffe and C. E. Sims, “Hydrogen Embrittlement, Internal Stress and Defects in Steel,” *Am. Inst. Mining, Metall. Pet. Eng.*, vol. 145, pp. 225–271, 1941.
- [18] W. Y. Choo and J. Y. Lee, “Thermal Analysis of Trapped Hydrogen in Pure Iron,” *Metall. Trans. A*, vol. 13A, no. January, pp. 135–140, 1982.
- [19] J.-Y. Lee and S. M. Lee, “Hydrogen trapping phenomena in metals with b.c.c. and f.c.c. crystal structures by the desorption thermal analysis technique*,” *Surf. Coatings Technol.*, vol. 28, pp. 301–314, 1986.
- [20] J. L. Lee and J. Y. Lee, “Hydrogen trapping in AISI 4340 steel,” *Met. Sci.*, vol. 17, pp. 426–432, 1983.
- [21] E. Wallaert, T. Depover, M. Arafin, and K. Verbeken, “Thermal desorption spectroscopy evaluation of the hydrogen-trapping capacity of NbC and NbN precipitates,” *Metall. Mater. Trans. A Phys. Metall. Mater. Sci.*, vol. 45, no. 5, pp. 2412–2420, 2014.
- [22] D. P. Escobar, K. Verbeken, L. Duprez, and M. Verhaege, “Evaluation of hydrogen trapping in high strength steels by thermal desorption spectroscopy,” *Mater. Sci. Eng. A*, vol. 551, pp. 50–58, 2012.
- [23] S. Lee and J. Lee, “The Trapping and Transport Phenomena of Hydrogen in Nickel,” *Metall. Trans. A*, vol. 17A, pp. 181–187, 1986.
- [24] H. E. Kissinger, “Reaction Kinetics in Differential Thermal Analysis,” *Anal. Chem.*, vol. 29, no. 11, pp. 1702–1706, 1957.
- [25] F. Huang, J. Liu, Z. J. Deng, J. H. Cheng, Z. H. Lu, and X. G. Li, “Effect of microstructure and inclusions on hydrogen induced cracking susceptibility and

References

- hydrogen trapping efficiency of X120 pipeline steel,” *Mater. Sci. Eng. A*, vol. 527, pp. 6997–7001, 2010.
- [26] L. B. Godefroid, L. C. Cândido, R. V. B. Toffolo, and L. H. S. Barbosa, “Microstructure and Mechanical Properties of Two Api Steels for Iron Ore Pipelines,” *Mater. Res.*, vol. 17, pp. 114–120, 2014.
- [27] J. H. Park, M. Oh, and S. J. Kim, “Effect of bainite in microstructure on hydrogen diffusion and trapping behavior of ferritic steel used for sour service application,” *J. Mater. Res.*, vol. 32, no. 7, pp. 1295–1303, 2017.
- [28] G. F. Vander Voort, Ed., *ASM Handbook. Metallography and Microstructures*, Vol. 9. Materials Park, OH, 2004.
- [29] J. Moon, C. Park, and S.-J. Kim, “Influence of Ti Addition on the Hydrogen Induced Cracking of API 5L X70 Hot-Rolled Pipeline Steel in Acid Sour Media,” *Met. Mater. Int.*, vol. 18, no. 4, pp. 613–617, 2012.
- [30] C. F. Dong, X. G. Li, Z. Y. Liu, and Y. R. Zhang, “Hydrogen-induced cracking and healing behaviour of X70 steel,” vol. 484, pp. 966–972, 2009.
- [31] X. Shi, W. Yan, W. Wang, L. Zhao, Y. Shan, and K. Yang, “Effect of Microstructure on Hydrogen Induced Cracking Behavior of a High Deformability Pipeline Steel,” *J. Iron Steel Res. Int.*, vol. 22, no. 10, pp. 937–942, 2015.
- [32] T. Kyada, J. R. Shant, R. K. Goyal, and T. S. Kathayat, “Understanding the Delamination and Its Effect on Charpy Impact Energy in Thick Wall Linepipe Steel,” *J. Mater. Metall. Eng.*, vol. 4, no. 1, pp. 31–39, 2014.
- [33] M. A. Mohtadi-Bonab, J. A. Szpunar, and S. S. Razavi-Tousi, “A comparative study of hydrogen induced cracking behavior in API 5L X60 and X70 pipeline steels,” *Eng. Fail. Anal.*, vol. 33, pp. 163–175, 2013.
- [34] C. F. Dong, Z. Y. Liu, X. G. Li, and Y. F. Cheng, “Effects of hydrogen-charging on the susceptibility of X100 pipeline steel to hydrogen-induced cracking,” *Int. J. Hydrogen Energy*, vol. 34, no. 24, pp. 9879–9884, 2009.
- [35] H. B. Xue and Y. F. Cheng, “Characterization of inclusions of X80 pipeline steel and its correlation with hydrogen-induced cracking,” *Corros. Sci.*, vol. 53, no. 4, pp. 1201–1208, 2011.
- [36] “API 5L: Specification for Line Pipe.” API Publishing Services, Washington, DC., p. 36, 2004.
- [37] *ASM Handbook. Properties and Selection: Irons Steels and High Performance Alloys*, Vol. 1. Materials Park, OH: ASM International, 2004.
- [38] H.-G. Hillenbrand, M. Gräf, and C. Kalwa, “Development and production of high strength pipeline steels,” *Niobium Sci. Technol. Conf. Proc.*, 2001.

References

- [39] J. Liu, H. Wu, Y.-P. Bao, and M. Wang, “Inclusion variations and calcium treatment optimization in pipeline steel production,” *Int. J. Miner. Metall. Mater.*, vol. 18, no. 5, pp. 527–534, 2011.
- [40] S. Nafisi, J. Jordan, C. D. Souza, L. Collins, and T. J. Drake, “A Study of Ca-Modification Process in Al-Killed Steels,” *AISTech - Iron Steel Technol. Conf. Proc.*, 2012.
- [41] David Broek, *Elementary Engineering Fracture Mechanics*. Hingham, MA: Martinus Nijhoff Publishers, 1982.
- [42] M. F. Ashby and D. R. H. Jones, *Engineering Materials I: An Introduction to their Properties and Applications*, 2nd ed. Jordan Hill, Oxford, UK: Butterworth-Heinemann, 1996.
- [43] J. R. Davis, Ed., *Tensile Testing*, Second Edi. Materials Park, OH: ASM International, 2004.
- [44] R. E. Ashburn, K. D. Hickey, A. L. Blyth, J. A. McConnell, L. B. Miller, C. P. Brown, C. A. Trobaugh, and K. J. McGhee, “A Publication of the Association for Iron & Steel Technology,” *Iron Steel Technol.*, vol. 11, no. 7, pp. 132–153, 2014.
- [45] “ASTM E112-13 Standard Test Methods for Determining Average Grain Size.” ASTM International, West Conshohocken, PA, 2013.
- [46] X. Pang, F. Fazeli, M. Attard, and C. Shi, “Assessment of Hydrogen Uptake and Permeation in AHSSs,” *Mater. Sci. Forum*, vol. 783–786, pp. 950–955, 2014.
- [47] F. W. H. Dean, “Hydrosteel Applications Instrument Manual V1.12.” Ion Science Ltd, Fowlmere, Cambs, pp. 1–64, 2009.
- [48] F. W. H. Dean, T. M. Smeeton, and D. J. Fray, “Hydrogen permeation through mild steel in temperature range 20 – 500°C measured by hydrogen collection method,” *Mater. Sci. Technol.*, vol. 18, pp. 851–855, 2002.
- [49] H. M. Ha, J.-H. Ai, and J. R. Scully, “Effects of prior cold work on hydrogen trapping and diffusion in API X-70 line pipe steel during electrochemical charging,” *Corrosion*, vol. 70, no. 2, pp. 166–184, 2014.
- [50] “Operation Manual - Cortest Proof Ring and Optional Equipment.” CorTest Inc., Willoughby, OH.
- [51] F. Xiao, B. Liao, Y. Shan, G. Qiao, Y. Zhong, C. Zhang, and K. Yang, “Challenge of mechanical properties of an acicular ferrite pipeline steel,” *Mater. Sci. Eng.*, vol. 431, pp. 41–52, 2006.
- [52] M. A. Meyers and K. K. Chawla, *Mechanical Behavior of Materials*, 2nd ed. Cambridge, England: Cambridge University Press, 2009.
- [53] J. Ćwiek, “Prevention methods against hydrogen degradation of steel,” *J. Achiev.*

References

- Mater. Manuf. Eng.*, vol. 43, no. 1, pp. 214–221, 2010.
- [54] A. Borruto, T. M. R. Borruto, and A. Spada, “Hydrogen-steel interaction: hydrogen embrittlement in pipes for power former plant effluents,” *Int. J. Hydrogen Energy*, vol. 24, pp. 651–659, 1999.
- [55] N. W. Sachs, “Understanding the surface features of fatigue fractures: How they describe the failure cause and the failure history,” *J. Fail. Anal. Prev.*, vol. 5, no. 2, pp. 11–15, 2005.
- [56] K. Fujii and K. Fukuya, “Development of Micro Tensile Testing Method in an FIB System for Evaluating Grain Boundary Strength,” *Mater. Trans.*, vol. 52, no. 1, pp. 20–24, 2011.
- [57] H. Dugdale, D. E. J. Armstrong, E. Tarleton, S. G. Roberts, and S. Lozano-Perez, “How oxidized grain boundaries fail,” *Acta Mater.*, vol. 61, no. 13, pp. 4707–4713, 2013.
- [58] J. Dohr, D. E. J. Armstrong, E. Tarleton, T. Couvant, and S. Lozano-Perez, “The influence of surface oxides on the mechanical response of oxidized grain boundaries,” *Thin Solid Films*, vol. 632, pp. 17–22, 2017.
- [59] D. E. J. Armstrong, A. J. Wilkinson, and S. G. Roberts, “Micro-mechanical measurements of fracture toughness of bismuth embrittled copper grain boundaries,” *Philos. Mag. Lett.*, vol. 91, no. 6, pp. 394–400, 2011.
- [60] R. Ding, J. Gong, A. J. Wilkinson, and I. P. Jones, “Transmission electron microscopy of deformed Ti-6Al-4V micro-cantilevers,” *Philos. Mag.*, vol. 92, no. 25–27, pp. 3290–3314, 2012.